VOLCANIC FACIES AND GEOCHEMICAL ANALYSIS OF THE TRIASSIC MAMMOTH ROCK BRECCIA AS A TEST OF EARLY-ARC PALEOGEOGRAPHY AND SUBDUCTION INCEPTION, EASTERN SIERRA NEVADA, CALIFORNIA

By Samantha K. Berglin

A Thesis

Submitted in Partial Fulfillment

of the Requirements for the Degree of

Master of Science

in Geology

Northern Arizona University

December 2021

Approved:

Nancy R. Riggs, Ph.D., Chair

Andrew P. Barth, Ph.D.

Michael H. Ort, Ph.D.

ABSTRACT

VOLCANIC FACIES AND GEOCHEMICAL ANALYSIS OF THE TRIASSIC MAMMOTH ROCK BRECCIA AS A TEST OF EARLY-ARC PALEOGEOGRAPHY AND SUBDUCTION INCEPTION, EASTERN SIERRA NEVADA, CALIFORNIA

SAMANTHA K. BERGLIN

The breccia of Mammoth Rock crops out in the Mount Morrison pendant in the eastern Sierra Nevada. The Triassic volcaniclastic facies of Mammoth Rock are a product of early arc magmatism that initiated after convergence began along a pre-existing transform fault. Early-arc paleogeography and subduction initiation that built the Sierra Nevada arc are poorly understood, despite decades of study. Early-arc paleogeography and induced subduction inception are recorded in the arc by tectonics including uplift, thrust faulting, and early-arc magmatism. The deposition, composition, magmatic source, and timing of magmatism for the breccia of Mammoth Rock provide an understanding of the arc paleogeography.

The breccia facies dominantly contain angular to subrounded clasts with variable amounts of cuspate, jigsaw-fit, and fluidal clast shapes and flow-banded clast textures dispersed throughout. Interbedded sandstone facies are composed of alternating fine- to coarse-grained sandstone with bedding characteristics including planar laminated, lenticular, low-angle tabular cross-bedded, and massive. The volcaniclastic and siliciclastic facies of Mammoth Rock suggest deposition in a shallow-marine environment likely between shoreface and a shallow-continental shelf. Collapse of solidified lava flows resulting in submarine mass wasting is suggested by the clasts in the polymictic and monomictic facies. Whole-rock geochemical analysis of clasts in the

breccia of Mammoth Rock reveals a trachyandesitic composition. Whole-rock geochemical analyses also show a high K_2O and Al_2O_3 weight %, low Mg#, LILE and LREE enrichment, and HREE depletion that suggest dominantly an upper crustal magma source that fractionated from a primitive melt to an evolved andesitic melt and reveal geochemical signatures consistent with a thick continental crust. The breccia and sandstone zircon trace element geochemistry reveal medium to high U/Yb concentrations that aligns with whole-rock geochemical data, supporting the inference of a thick continental crust. Geochronologic analysis of zircon confine the timing of magmatism for the breccia of Mammoth Rock to ca. 225 - 216 Ma. Maximum depositional ages from detrital zircon in the sandstone facies suggest deposition as a result of mass wasting of breccia of Mammoth Rock occurred between ca. 222 Ma and 216 Ma.

© Samantha Berglin, 2021

ACKNOWLEDGEMENTS

Thank you to my family, friends and colleagues for their continued support throughout the last two years during this research project. I am so thankful for my husband who went on this big adventure with me to Arizona to further my education and for his love and encouragement during this chapter of my life. I am forever grateful for my mom's encouragement. I would not be where I am today without all the late-night phone calls and video calls with her. She truly helped me navigate life's rough patches and setbacks during this project, which allowed me to remain focused and driven to finish my research. I would like to thank my parents and my in-laws for all the ways they supported me during my Masters. I would like to thank my field assistant, Sonya Bogle, who trekked across rough terrain with me to conduct field mapping and collect samples for this project. Lastly, I am very thankful for my advisor, Nancy Riggs, for giving me this opportunity to further my education and knowledge in the field of geology. This research opportunity has allowed me to grow in many ways as a geologist including new lab skills and improvement of my scientific writing skills. It has built my self-confidence and allowed me to see my true potential.

TABLE OF CONTENTS

LIST OF TABLES…… viii

LIST OF FIGURES……... xi

1. INTRODUCTION……. 1

2. BACKGROUND…… 4

2.1 GEOLOGIC HISTORY OF THE SIERRA NEVADA MESOZOIC ARC……. 4

2.2 FORMATION OF EASTERN SIERRA NEVADA ROOF PENDANTS...…… 5

2.3 GEOLOGIC HISTORY OF MAMMOTH ROCK…….. 6

2.4 SUBAQUEOUS VOLCANISM…….. 6

2.5 SUBDUCTION INITIATION……. 7

3. METHODS…… 8

3.1 GEOLOGIC MAPPING…….. 8

3.2 PETROGRAPHY…… 8

3.3 GEOCHEMISTRY…….. 9

3.4 GEOCHRONOLOGY……. 10

4. FACIES DESCRIPTIONS…… 12

4.1 BRECCIA OF MAMMOTH ROCK…….. 12

4.2 SANDSTONE OF MAMMOTH ROCK…… 21

5. RESULTS……. 25

5.1 PETROGRAPHY……... 25

5.2 GEOCHEMISTRY……. 31

5.2.1 MAJOR ELEMENT GEOCHEMISTRY…… 31

5.2.2 TRACE ELEMENT GEOCHEMISTRY……. 37

5.2.3 ZIRCON GEOCHEMISTRY……... 46

5.3 GEOCHRONOLOGY……. 48

5.3.1 BRECCIA OF MAMMOTH ROCK…… 49

5.3.2 SANDSTONE OF MAMMOTH ROCK……. 50

6. DISCUSSION AND INTERPRETATIONS……. 52

6.1 FACIES INTERPRETATIONS……... 52

6.2 PETROGRAPHIC INTERPRETATIONS…….…….. 58

6.3 GEOCHEMISTRY INTERPRETATIONS…….. 59

6.4 GEOCHRONOLOGY INTERPRETATIONS…….. 67

6.5 EARLY ARC-PALEOGEOGRAPHY AND SUBDUCTION INCEPTION…… 69

6.6 MODERN ANALOGY FOR THE SIERRA NEVADA……... 71

7. CONCLUSIONS…….. 72

REFERENCES……. 75

APPENDIX A…….. 82

APPENDIX B…….…….. 84

APPENDIX C…….…….. 91

APPENDIX D…….... 103

LIST OF TABLES

Table 1: Whole-rock geochemical data for the 10 clasts of the breccia of Mammoth Rock with the sample name and associated IGSN number…….. 32

Table 2: Clast characteristics, eruption style, and emplacement mechanism for breccia facies of Mammoth Rock…….. 57

Table 3a: GPS locations of breccia clast samples and type of analyses conducted on the sample……. 82

Table 3b: GPS locations of breccia clast samples and type of analyses conducted on the sample……. 83

Table 4: Hand sample and thin sections descriptions of breccia samples…….. 84

Table 5a: Zircon trace element geochemical data for 48 zircon from the breccia of Mammoth Rock…… 91

Table 5b: Zircon trace element geochemical data for 48 zircon from the breccia of Mammoth Rock…… 92

Table 6a: Zircon trace element geochemical data for 266 detrital zircon from the sandstone of Mammoth Rock…….. 93

Table 6b: Zircon trace element geochemical data for 266 detrital zircon from the sandstone of Mammoth Rock…….. 94

Table 6c: Zircon trace element geochemical data for 266 detrital zircon from the sandstone of Mammoth Rock…….. 95

Table 6d: Zircon trace element geochemical data for 266 detrital zircon from the sandstone of Mammoth Rock…….. 96

Table 6e: Zircon trace element geochemical data for 266 detrital zircon from the sandstone of Mammoth Rock…….. 97

Table 6f: Zircon trace element geochemical data for 266 detrital zircon from the sandstone of Mammoth Rock…….. 98

Table 6g: Zircon trace element geochemical data for 266 detrital zircon from the sandstone of Mammoth Rock…….. 99

Table 6h: Zircon trace element geochemical data for 266 detrital zircon from the sandstone of Mammoth Rock…….. 100

Table 6i: Zircon trace element geochemical data for 266 detrital zircon from the sandstone of Mammoth Rock…….. 101

Table 6j: Zircon trace element geochemical data for 266 detrital zircon from the sandstone of Mammoth Rock…….. 102

Table 7a: U-Pb age data for 48 zircon grains from 5 clast samples of the breccia of Mammoth Rock (BMR)……... 103

Table 7b: U-Pb analytical data for 48 zircon grains from 5 clast samples of the breccia of Mammoth Rock (BMR)……. 104

Table 8a: U-Pb age data for detrital zircon grains from 2 bulk-rock samples of the sandstone of Mammoth Rock…….. 105

Table 8b: U-Pb age data for detrital zircon grains from 2 bulk-rock samples of the sandstone of Mammoth Rock…….. 106

Table 8c: U-Pb age data for detrital zircon grains from 2 bulk-rock samples of the sandstone of Mammoth Rock…….. 107

Table 8d: U-Pb age data for detrital zircon grains from 2 bulk-rock samples of the sandstone of Mammoth Rock…….. 108

Table 8e: U-Pb age data for detrital zircon grains from 2 bulk-rock samples of the sandstone of Mammoth Rock…….. 109

Table 8f: U-Pb age data for detrital zircon grains from 2 bulk-rock samples of the sandstone of Mammoth Rock…….. 110

Table 9a: U-Pb analytical data for detrital zircon grains from 2 bulk-rock samples of the sandstone of Mammoth Rock……. 111

Table 9b: U-Pb analytical data for detrital zircon grains from 2 bulk-rock samples of the sandstone of Mammoth Rock……. 112

Table 9c: U-Pb analytical data for detrital zircon grains from 2 bulk-rock samples of the sandstone of Mammoth Rock……. 113

Table 9d: U-Pb analytical data for detrital zircon grains from 2 bulk-rock samples of the sandstone of Mammoth Rock……. 114

Table 9e: U-Pb analytical data for detrital zircon grains from 2 bulk-rock samples of the sandstone of Mammoth Rock……. 115

Table 9f: U-Pb analytical data for detrital zircon grains from 2 bulk-rock samples of the sandstone of Mammoth Rock……. 116

LIST OF FIGURES

Figure 1: Map of the eastern Sierra Nevada modified from Field (2018) displaying major rock types and corresponding ages in the Ritter Range pendant (RRP), Saddlebag Lake pendant (SLP), and Mount Morrison pendant (MMP). Location of Mammoth Rock indicated by the yellow square on the map…… 3

Figure 2: Clast shapes of Mammoth Rock breccia include A) cuspate, B) jigsaw-fit, and C) fluidal. D) Flow-banded clast texture. Clast shapes and textures are shown by yellow arrows. Cuspate, fluidal and flow-banded clasts are observed in both the monomictic and polymictic breccia. Jigsaw-fit was only observed in the monomictic breccia. The white scale card is 15.3 cm long…….…….. 12

Figure 3: A) Monomictic facies with black volcanic clasts. B-C) Polymictic facies with black volcanic clasts with feldspar (BV), white-gray volcanic clasts with pyroxene (WV), white marble clasts (M), gray metasedimentary clasts (MS), and gray-purple devitrified volcanic clasts (GPDV). The white scale card is 15.3 cm long…….…….….. 14

Figure 4: Map of Mammoth Rock facies and contiguous geologic units. Facies 1-8 are labelled F1-F8. F1-F4 (shades of blue) are breccia units. F1 and F3 are the most common breccia facies. Jigsaw-fit clasts are shown on the map by a triangle. F5-F8 (brown) are S-SW dipping sandstone beds. Strike and dip of sandstone beds are displayed on the map. Geochronology sample locations indicated by orange circles for sandstone and green circles for breccia….……..…. 15

Figure 5: Clasts of the monomictic breccia facies 1. A-B) Angular to subrounded clasts with varying sizes of jigsaw-fit (JF) and cuspate (C) clasts. C) The largest clast (70 cm) found in facies 1 with an angular to subangular shape. White scale card is 15.3 cm long……..… 16

Figure 6: Clasts of the monomictic breccia facies 2. Clasts are highly fluidal. A) Fluidal clasts with a modal percentage of 10%. B) Fluidal clasts with a modal percentage of 5%. The white scale card is 15.3 cm long……..… 17

Figure 7: A-C) Clasts of the polymictic breccia facies 3. Polymictic breccia facies include black volcanic clasts with feldspar (BV), white-gray volcanic clasts with pyroxene (WV), white marble clasts (M), gray metasedimentary clasts (MS), and gray-purple devitrified volcanic clasts (GPDV). The white scale card is 15.3 cm long…… 19

Figure 8: A-B) Clasts of the sparsely polymictic breccia facies 4. The BV clast is the most dominant and there are ≤ 1% of each of the other clast types. Sparsely polymictic breccia facies may have any of the five clast types including black volcanic clasts with feldspar (BV), white-gray volcanic clasts with pyroxene (WV), white marble clasts (M), gray metasedimentary clasts (MS), and gray-purple devitrified volcanic clasts (GPDV). A) Sparsely polymictic breccia showing the dominant BV clast with ≤ 1% of M clasts. B) Sparsely polymictic breccia showing the dominant BV clast with ≤ 1% of the M, MS, and GPDV clasts. The white scale card is 15.3 cm long…….……. 20

Figure 9: A-C) Planar laminated sandstone facies of Mammoth Rock (facies 5). Planar laminated sandstone layers alternate in grain size and vary in thickness. The white scale card is 15.3 cm long…….. 22

Figure 10: Planar laminated sandstone with a breccia lens indicated by yellow arrow (facies 6). The white scale card is 15.3 cm long…….. 23

Figure 11: A-B) Low-angle tabular cross-bedded sandstone (facies 7). The white scale card is 15.3 cm long……. 24

Figure 12: Photomicrograph of sample 8230-1D from facies 3 at 2x magnification. A) Image in plane-polarized light showing minor epidote (ep) alteration of the groundmass and spotty alteration of plagioclase phenocrysts (Pl). B) Image in cross-polarized light shows plagioclase phenocrysts (Pl) with secondary muscovite (ms) crystal growth in a fine-grained groundmass with epidote alteration (ep) and secondary mineral growth of quartz (qtz)……. 27

Figure 13: Photomicrograph of sample 72720-2C from facies 3 at 4x magnification. A) Image in plane-polarized light differentiates the devitrified groundmass from minor sericite (ser) alteration of the groundmass and shows abundant sericite alteration within a plagioclase phenocryst (Pl). B) Image in cross-polarized light shows some small plagioclase phenocrysts (Pl) and a large plagioclase phenocryst with sericite (ser) alteration in a fine-grained groundmass with minor epidote (ep) alteration……... 28

Figure 14: Photomicrograph of sample 727920-4A from facies 3 at 2x magnification. A) Image in plane-polarized light shows major sericite (ser) alteration of the groundmass. B) Image in cross-polarized light shows abundant sericite (ser) alteration of the fine-grained groundmass with secondary muscovite (ms) crystal growth……..……. 29

Figure 15: Photomicrograph of sample 727920-5A from facies 3 at 2x magnification. A) Image in plane-polarized light shows abundant sericite (ser) and moderate epidote (ep) alteration of the groundmass with highly altered spotty plagioclase phenocrysts (Pl). B) Image in cross-polarized light shows plagioclase (Pl) phenocryst with abundant sericite (ser) and epidote (ep) alteration of the fine-grained groundmass with secondary muscovite (ms) crystal growth. Highly altered mineral (yellow arrow) is likely plagioclase……. 30

Figure 16. TAS diagram of clasts from the breccia of Mammoth Rock (BMR) for rock classification (modified from Le Bas et al., 1986). BMR clast compositions range from andesitic to dacitic…… 33

Figure 17. TAS diagram of the clasts from breccia of Mammoth Rock (BMR) and breccia of Frog Lakes (FLB) samples (modified from Le Bas et al., 1986). BMR clast compositions range from andesitic to dacitic. FLB compositions range from basaltic to andesitic. Bold dashed line denotes alkaline rocks (above line) and subalkine rocks (below line)…….. 34

Figure 18a: Harker variation diagrams of SiO_2 versus major element oxides for clasts from the breccia of Mammoth Rock…… 35

Figure 18b: Harker variation diagrams of SiO_2 versus major element oxides for clasts from the breccia of Mammoth Rock…… 36

Figure 19: Discrimination plot of SiO2 versus trace elements Nb/Y to determine composition and rock classification (modified from Winchester and Floyd, 1977)……..... 38

Figure 20: Discrimination plot of arc type for clasts from the breccia of Mammoth Rock (BMR) and breccia of Frog Lakes (FLB) (Pearce, 1983)……. 39

Figure 21: Discrimination plot of arc type and magmatic setting for clasts from the breccia of Mammoth Rock (BMR) and breccia of Frog Lakes (FLB) (Pearce, 1983)…….……. 40

Figure 22: Discrimination plot of the magmatic setting for clasts from the breccia of Mammoth Rock (BMR) and breccia of Frog Lakes (FLB) (Pearce et al., 1984)……... 41

Figure 23: Discrimination plot of the magmatic setting for clasts from the breccia of Mammoth Rock (BMR) and Frog Lakes breccia (FLB) (Pearce et al., 1984)……..…… 41

Figure 24: Trace element plot of Ba/La versus Ba for clasts from the breccia of Mammoth Rock (BMR) and breccia of Frog Lakes (FLB) (Hildreth and Moorbath, 1988)……...… 42

Figure 25: Spider diagram of mobile and immobile trace elements for clasts from the breccia of Mammoth Rock (BMR) normalized to chondrite (Sun and McDonough, 1995). Breccia compared to average upper and lower crustal values (Lee et al., 2007)……...… 43

Figure 26: Spider diagram of mobile and immobile trace elements for clasts from the breccia of Mammoth Rock (BMR) normalized to chondrite (Sun and McDonough, 1995). Breccia compared to average N-MORB, E-MORB and OIB (Sun and McDonough, 1989)……...…. 44

Figure 27: Spider diagram of mobile and immobile trace elements for clasts from the breccia of Mammoth Rock (BMR) and breccia of Frog Lakes (FLB) normalized to chondrite (Sun and McDonough, 1995). Breccia compared to average N-MORB, E-MORB and OIB (Sun and McDonough, 1989)……..…… 45

Figure 28: Spider diagram of mobile and immobile trace elements for clasts from the breccia of Mammoth Rock (BMR) and breccia of Frog Lakes (FLB) normalized to chondrite (Sun and McDonough, 1995). BMR and FLB compared to average upper and lower crustal values (Lee et al., 2007)……... 45

Figure 29: Trace element plot of U/Yb versus Hf from zircon trace-element geochemistry for the five samples that produced zircon from the breccia of Mammoth Rock (BMR). All of the zircon for BMR are classified as medium to high U/Yb…...…….. 47

Figure 30: Trace element plot of U/Yb versus Hf from detrital zircon trace-element geochemistry for two bulk-rock samples from the sandstone of Mammoth Rock. The zircon are dominantly classified as high U/Yb……. 48

Figure 31: A) Concordia diagram of zircon from breccia clast sample 72720-2E. B) Weighted mean plot of zircon from breccia clast sample 72720-2E. MSWD = mean square of weighted deviates. N = number of crystals analyzed…….…….. 49

Figure 32: A) Concordia diagram of zircon from breccia clast sample 73020-1A. B) Weighted mean plot of zircon from breccia clast sample 73020-1A. MSWD = mean square of weighted deviates. N = number of crystals analyzed…….…….. 50

Figure 33: A) Concordia diagram of detrital zircon from the lower sandstone sample 72820. B) Weighted mean plot of detrital zircon from sandstone sample 72820. MSWD = mean square of weighted deviates. N = number of crystals analyzed…… 51

Figure 34: A) Concordia diagram of detrital zircon from the upper sandstone sample 72920. B) Weighted mean plot of detrital zircon from sandstone sample 72920. MSWD = mean square of weighted deviates. N = number of crystals analyzed…… 51

Figure 35: Interpreted fractional crystallization trends based on regression analysis for the breccia of Mammoth Rock (BMR) on Harker variation diagrams. Major element oxides for the BMR display weak negative trends for oxides of high-charge cations including TiO_2 and Al_2O_3. No trends are observed for oxides of low-charge cations. Trend arrows are vectors showing amount of change caused by 10% fractionation of the stated minerals. Compositions of the minerals are from Escobar-Burciaga (2016)……. 63

1. INTRODUCTION

The early Mesozoic Cordilleran arc in eastern California formed on the southwestern Laurentian passive margin as a result of plate convergence, which caused induced-subduction inception and arc magmatism (Stern, 2004; Saleeby and Dunne, 2015). Despite decades of study of the Sierra Nevada (Rinehart and Ross, 1964; Schweickert and Cowan, 1975; Tobisch and Fiske, 1982; Stevens and Greene, 2000; Barth et al., 2011, Saleeby and Dunne, 2015; Levy et al., 2021), early-arc paleogeography and subduction initiation are poorly understood. Induced-subduction initiation that is proposed for the early Mesozoic Cordilleran arc resulted from plate convergence along a transform boundary and collapse of the transform boundary into a subduction zone (Stern, 2004). The Sierra Nevada arc initially formed on a convergent margin that underwent crustal thickening, uplift of buoyant crust, and thrust faulting (Saleeby and Dunne, 2015), which are characteristics of induced-subduction inception (Stern, 2004); therefore, the early arc should consist of intermediate volcanic rocks that reflect geochemical signatures related to the upper crust. The depositional environment of the eastern Sierra Nevada was likely a shallow-marine environment based on the subaqueous clast shapes of the breccia of Mammoth Rock. Previous studies also suggest the Sierra Nevada paleogeography consisted of a shallow- to marginal-marine environment that later transitioned into terrestrial environments in the southeastern region of the arc (Howell and Blakey, 2013; Riggs et al., 2020). Changes in the paleogeography began at ca. 235 Ma in the southeastern region of the arc and are recorded by progradation of conglomerates with an abundance of arc-derived volcanic rock in the Chinle Formation and backarc dynamic subsidence. The deposition of sedimentary formations, such as the Chinle Formation and Buckskin Formation, suggest a shallow- to marginal-marine setting for the Sierra Nevada arc prior to ca. 235 Ma transition.

The earliest inception of subduction for the arc is recorded at the southwestern margin of the North American Cordillera in the Mojave Desert by 295 Ma initiation of the Last Chance thrust system (Lodes et al., 2020), the oldest arc plutons (275 Ma) in the El Paso terrane (Saleeby and Dunne, 2015), and the 255 Ma Foothills metamorphic belt. The tectonics of the Last Chance thrust system and initiation of magmatism suggest subduction inception occurred between 295 - 285 Ma (Lodes et al., 2020). Subduction inception in the central Sierra Nevada is marked by the intrusion of metamorphic diapirs into the western Foothills ophiolitic mélange and metamorphic belt at 255 Ma (Saleeby and Dunne, 2015). In the eastern Sierra Nevada, the earliest magmatism is recorded by the 232 ± 1.4 Ma intrusion of the Spiller Canyon Pluton (Cao et al., 2015) and the 232 ± 2 Ma Black Mountain tuff (Barth et al., 2011).

Volcanic rocks in the Sierra Nevada preserved as roof pendants record the paleogeography of the volcanic arc (Schweickert and Cowan, 1975). The Mount Morrison pendant is one of these preserved roof pendants. Triassic volcaniclastic facies of Mammoth Rock make up the oldest volcanic unit within the Mount Morison pendant (Fig. 1; Rinehart and Ross, 1964). A preliminary study of the volcaniclastic rocks by Field (2018) indicated subaqueous deposition of a breccia with hyaloclastic clast shapes, but arc formation on a continental plate allows the possibility of a subaerial or subaqueous depositional environment. Further investigation of Mammoth Rock breccia was conducted to determine the depositional environment, composition, and the magma source.

This project provides a deeper understanding of the paleogeography and geochemistry of the early arc. Early-arc paleogeography is assessed through determining the depositional environment, composition, and magma source of the breccia of Mammoth Rock. The volcaniclastic facies and geochemistry of Mammoth Rock suggest deposition of andesitic breccia

in a shallow-marine environment, a magma source related dominantly to the upper crust with minor to moderate influence of subduction, and arc formation on a thick continental crust. The volcaniclastic facies and geochemical signatures of Mammoth Rock breccia contribute to the larger investigation of the early-arc paleogeography of the Sierra Nevada arc and the mode of subduction inception.

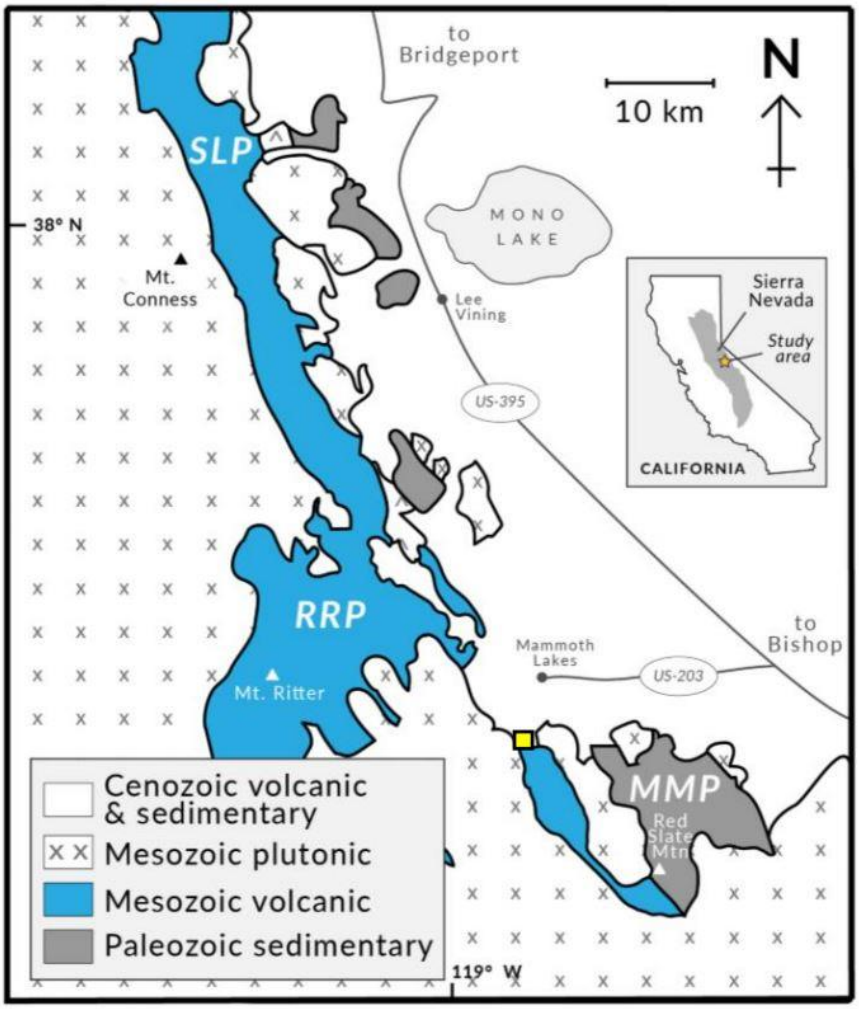

Figure 1. Map of the eastern Sierra Nevada modified from Field (2018) displaying major rock types and corresponding ages in the Ritter Range pendant (RRP), Saddlebag Lake pendant (SLP), and Mount Morrison pendant (MMP). Location of Mammoth Rock indicated by the yellow square on the map.

2. BACKGROUND

2.1 GEOLOGIC HISTORY OF THE SIERRA NEVADA MESOZOIC ARC

The Sierra Nevada arc is part of the Mesozoic Cordilleran margin of North America, known as Laurentia. The southwestern margin of Laurentia was bounded by a passive margin that formed during Precambrian rifting (Dickinson, 1977). The Laurentian passive margin was truncated by ca. 300 Ma (Walker, 1988) due to the initiation of the late Paleozoic California-Coahuila transform fault (Dickinson, 1977; Dickinson, 2004), which caused a shift to an oblique convergent boundary along the pre-existing fault and inception of induced subduction (Saleeby and Dunne, 2015). The boundary shift to a convergent margin was marked by early stages of arc plutonism and regional transpressive fold-and-thrust deformation, as well as uplift in the overriding upper plate due to crustal thickening and buoyancy (Saleeby and Dunne, 2015).

Saleeby and Dunne (2015) inferred that the magmatic arc formed in a submarine environment across transitional and oceanic terranes and grew dominantly through accretion of subduction complexes, arc collision, arc volcanism, and ophiolite genesis (Snow and Scherer, 2006). Structural and stratigraphic studies indicate a three-stage history of Mesozoic arc volcanism with two lulls (Tobisch and Fiske, 1982; Schweickert and Cowan, 1975; Sorenson et al., 1998). The first stage occurred during the early Triassic period with the production and deposition of early-arc volcaniclastic rocks in a marine setting. The second stage occurred during late Jurassic to early Cretaceous time and is marked by regional shortening and tilting. The third stage occurred during the Cretaceous Period with deposition of volcanic rocks in a subaerial setting. Barth et al. (2011) concluded that the plutonism and volcanism were coeval and cogenetic based on geochronology and zircon trace-element geochemistry, which provide insight

into magmatic processes and petrogenesis of the arc. Prior to arc magmatism, the eastern Sierra Nevada was composed of Paleozoic passive-margin sedimentary rocks, deep-sea sedimentary rocks, and mafic-submarine igneous rocks that are now dominantly exposed as allochthons (Speed, 1979; Stevens and Greene, 2000)

2.2 FORMATION OF EASTERN SIERRA NEVADA ROOF PENDANTS

The eastern Sierra Nevada contains multiple roof pendants including the Mount Morrison, Ritter Range, Saddlebag Lake, Bishop Creek, Pine Creek, Deadman Pass, Gull Lake, and the Log Cabin Mine pendants (Stevens and Greene, 1999). Eastern Sierra Nevada Mesozoic volcanic and clastic rocks unconformably overlie the Paleozoic rocks and granitic rocks intrude them, recording the growth of the Sierra Nevada batholith (Schweickert and Cowan, 1975). Major tectonic events are recorded in the eastern pendants by thrust faulting of the Golconda and Nevahbe faults and deformation caused by the Antler, Morrison, and Sonoma orogenies (Stevens and Greene, 2000). Eastern Sierra Nevada pendants have experienced multiple phases of Paleozoic to Late Cretaceous deformation resulting in steeply dipping bedding, foliation, subvertical lineation, and multiple shear zones and faults (Cao et al., 2015). Regional foliation in the eastern pendants was caused by multiple phases of subparallel deformation that resulted in overprinting of older Paleozoic and Mesozoic rocks (Tobisch and Fiske, 1982; Cao et al., 2015).

Roof pendants contain sedimentary deposits ranging from deep-water shales, limestone, and turbidites to shallow-water carbonates, sandstones, and siltstones that represent passive-margin rocks (Stevens and Greene, 2000). Roof pendants also contain preserved early Mesozoic volcanic deposits that record the initiation of arc magmatism (Barth et al., 2018). The most common deposits in the eastern pendants are Mesozoic silicic ignimbrites and pyroclastic rocks,

andesitic lavas, marine to non-marine volcanic sandstones and mudstones, and limestone (Schweickert and Cowan, 1975).

2.3 PREVIOUS STUDIES OF MAMMOTH ROCK

Mammoth Rock is located in the Mount Morrison pendant (Fig. 1) and is composed of Paleozoic Mount Baldwin limestone faulted against Mesozoic volcaniclastic rock (Rinehart and Ross, 1964; Field, 2018). Numerous thrust faults are observed in the Mount Morrison pendant including the Convict Creek fault, the Laurel Mountain fault, the Mount Morrison fault, McGee Creek fault, Esha Canyon fault, and the Nevahbe fault (Stevens and Greene, 2000). The Triassic volcaniclastic facies of Mammoth Rock make up the oldest volcanic unit within the Mount Morrison pendant (Rinehart and Ross, 1964). Rinehart and Ross (1964) classified the Mesozoic volcaniclastic rock as a rhyolitic metavolcanic breccia that contains fragments of angular volcanic rock and rounded to subrounded metasedimentary rock. Preliminary facies analysis of the volcaniclastic rocks by Field (2018) suggested subaqueous deposition of an andesitic, polymictic and monomictic breccia with two interbedded sedimentary beds with a succession thickness of ~320 meters. The volcanic facies are altered and recrystallized, which indicates metamorphism alteration occurred.

2.4 SUBAQUEOUS VOLCANISM

Batiza and White (2000) summarized processes common in subaqueous volcanism. Submarine lava flows, hyaloclastite, and hypabyssal intrusive complexes can be produced by subaqueous volcanism. Submarine lava flows occur in various forms including pillow lava flows, lobate lava flows, and multiple types of sheet lava flows. Hypabyssal intrusive complexes occur when the magma density is greater than the density of the sediment and causes shallow-level

intrusions into the unconsolidated sediment. Hydroclastic rocks, including hyaloclastite, are volcaniclastic rocks produced by the interaction of magma and water. Hyaloclastite is quenched-glass fragments that are rapidly cooled in subaqueous settings. Hyaloclastite may be produced in terrestrial subaqueous environments and commonly in marine settings such as deep-sea environments at emergent islands, island arcs, mid-ocean ridges, and seamounts. Ancient submarine volcanic successions now on land, like the breccia of Mammoth Rock, allow us to view a succession of events through time due to exposed volcanic stratigraphy and facies.

2.5 SUBDUCTION INITIATION

The two types of subduction initiation, spontaneous and induced, are speculated to have different characteristics in relation to volcanic successions and geochemical signatures (Leng et al., 2012). Induced-subduction initiation results from plate convergence along a transform boundary and causes a subduction zone to form at the transform boundary (Stern, 2004). Induced-subduction initiation is characterized by early stages of compression, uplift in the upper plate, and thrust faulting. Spontaneous-subduction initiation results from gravitational instability of weak oceanic lithosphere and lithospheric collapse at a passive margin or transform boundary. Spontaneous-subduction initiation is characterized by extension and rifting.

Induced- and spontaneous-subduction initiation can each be further distinguished by subclasses (Stern, 2004). Induced-subduction initiation can occur through transference or polarity reversal. Transference occurs when buoyant crust enters the subduction zone, which causes collision and failure of the subduction zone and results in the formation of a new subduction zone outboard of the collision zone. Polarity reversal also occurs when buoyant crust enters the subduction zone, but the new subduction zone forms in the overriding plate and the

subduction zone dip direction reverses. Spontaneous subduction initiation can occur through passive margin collapse or transform collapse. Passive margin collapse occurs from the collapse of weak lithosphere beneath a passive margin. Transform collapse occurs from the collapse of weak lithosphere along a transform fault.

3. METHODS

This study involves geologic field mapping, facies analysis, petrography, geochemistry, and geochronology. Field work was completed during the summer of 2020 and laboratory work was completed during fall 2020 and spring 2021. The objective is to determine and understand the depositional environment, composition, magma source, and timing of magmatism to provide a clearer context regarding the arc paleogeography and mode of subduction inception.

3.1 GEOLOGIC MAPPING

Field work consisted of geologic mapping at a scale of 1:5,000 and a detailed volcanic facies analysis of the breccia of Mammoth Rock along with a supplementary facies analysis of the sandstone interbeds of Mammoth Rock. Analysis of the sandstone facies was done by my field assistant, Sonya Bogle. The geologic mapping and analysis of the volcanic facies and sedimentary facies provide evidence of the depositional environment. GPS locations of samples and associated analyses are provided in Appendix A.

3.2 THIN SECTION PETROGRAPHY

Fifteen breccia samples were cut into billets and sent to Quality Thin Sections in Tucson, AZ, for preparation of petrographic thin sections. Thin sections provide further insight into the

composition and magmatic processes through the minerals present and textures that suggest magmatic reactions and crystallization sequence. Thin section photomicrographs were taken at the State University of New York College at Oneonta (SUNY Oneonta) with an Olympus BX51 microscope that contains an Infinity HD camera with eyepiece lenses 10x and objective lenses of 2x, 4x, and 10x. The microscope uses Infinity HD Capture image capture software and Illustrator for image processing software. Detailed thin sections descriptions with corresponding hand sample descriptions are provided in Appendix B.

3.3 GEOCHEMISTRY

Whole-rock major and trace element geochemical analysis was conducted on ten clasts to identify the source of magmatism and composition. Each sample was crushed with the jaw crusher at Northern Arizona University and >30 grams of the crushed clast was collected. XRF (x-ray fluorescence) analysis for major-element and Rb, Sr, and Zr was completed on fused glass disks at Michigan State University using a Bruker spectrometer. Further trace element analyses were completed on the same whole-rock glasses with the Micromass ICP-MS (inductively coupled plasma-mass spectrometer). The following major element oxides and trace elements were analyzed: SiO_2, TiO_2, AlO_2, Fe_2O_3, MnO, MgO, CaO, Na_2O, K_2O, Sc, V, Cr, Co, Ni, Rb, Sr, Y, Zr, Nb, Cs, Ba, La, Ce, Pr, Nd, Sm, Eu, Gd, Tb, Dy, Ho, Er, Tm, Yb, Lu, Hf, Ta, Pb, Th, and U (Table 1). Precision was monitored using JB-2 and BHVO-2 GSJ and USGS rock standards. Precision is better than 1% for most major element oxides and trace elements with concentrations > 100 ppm and for less abundant trace element concentrations precision is 2 - 5%.

3.4 ZIRCON GEOCHRONOLOGY AND TRACE ELEMENT GEOCHEMISTRY

Ten breccia clasts were processed to extract zircon. Two sandstone samples, one from a lower interbed and one from an upper interbed, were collected and processed by Sonya Bogle to extract detrital zircon. Breccia and sandstone samples were individually crushed with the jaw crusher and steel roller mill. The samples were then sieved to remove grains larger than 500 μm. The sieved grains were run through the Frantz magnetic separator at 0.3 A, 0.5 A, and 1.0 A to remove magnetic grains. Non-magnetic grains were then separated through dense-liquid mineral separation, which allowed zircon to sink in the liquid. Zircon crystals were hand-picked from the remaining grains. The process of rock crushing, mineral separation, and zircon extraction were conducted at Northern Arizona University.

U-Pb geochronology of the breccia was conducted to determine the crystallization age and constrain the period of magmatism recorded by the breccia of Mammoth Rock. U-Pb geochronology of the sandstone was conducted to determine the maximum depositional age of the sandstone interbeds of Mammoth Rock. Elemental concentrations and isotopic ratios of the zircon were analyzed at the University of California at Santa Barbara (UCSB) Laser Ablation Split Stream (LASS) facility. The facility is equipped with Photon Machines Analyte G2 193 nm excimer laser with a HeLex sample cell, a Nu Plasma HR MC-ICPMS (high resolution multi-collector inductively coupled plasma mass spectrometer), and a Nu AttoM single collector ICPMS. Analyses of the zircon were normalized against the 91500, N612, GJ1, and Plesovice zircon standards. Data were reduced using Iolite 2.5 software in Igor Pro 6.37. Error assessment is based on Kylander-Clark et al. (2013). Five out of ten clast samples produced no zircon. Data from the five clast samples with zircon were used for trace element geochemical interpretations. Of the five clast samples with zircon, only two samples provided a sufficient number of zircon

grains for age determination. Zircon trace element geochemical data for all five clast samples that contained zircon are provided in Appendix C. Data from 119 out of 266 detrital zircon from two sandstone samples with a MSWD < 1.0 were used for interpretations. Zircon trace element geochemical data for all detrital zircon grains from the two sandstone samples is provided in Appendix C. All U-Pb data from the five clast samples and two sandstone samples are provided in Appendix D.

4. FACIES DESCRIPTIONS

4.1 BRECCIA OF MAMMOTH ROCK

The breccia of Mammoth Rock is a matrix-supported breccia composed of 5-35% volcanic and metasedimentary clasts. Clasts have various shapes and compositions dispersed into monomictic and polymictic breccia units. Clast shapes vary throughout breccia facies from angular to subrounded, cuspate (Fig. 2A), jigsaw-fit (Fig. 2B), and fluidal (irregular) clasts (Fig. 2C). Flow-banded clast textures (Fig. 2D) are also dispersed throughout the facies.

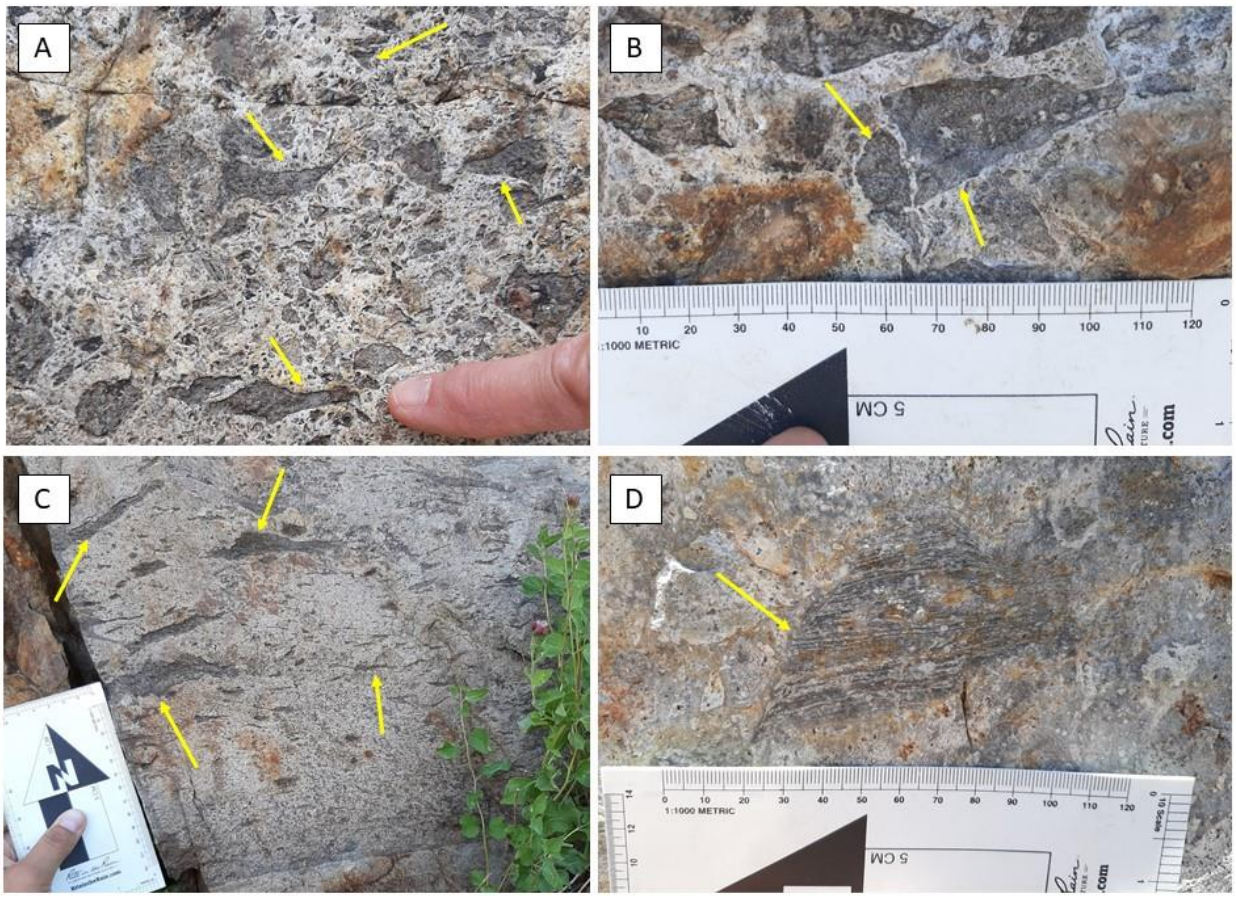

Figure 2. Clast shapes of Mammoth Rock breccia include **A)** cuspate, **B)** jigsaw-fit, and **C)** fluidal. **D)** Flow-banded clast texture. Clast shapes and textures are shown by yellow arrows. Cuspate, fluidal and flow-banded clasts are observed in both the monomictic and polymictic breccia. Jigsaw-fit was only observed in the monomictic breccia. The white scale card is 15.3 cm long.

The clasts in the monomictic breccia (Fig. 3A) are a black volcanic rock with white plagioclase phenocrysts. Clast shapes are dominantly angular to subangular, but vary from angular to subrounded, cuspate, jigsaw-fit, and fluidal throughout the facies. Flow-banded clast textures are dispersed throughout.

The polymictic breccia (Fig. 3B and 3C) contains two to five different types of clasts: 1) black volcanic clasts with plagioclase phenocrysts; 2) white to gray volcanic clasts with pyroxene phenocrysts; 3) white marble clasts; 4) gray metasedimentary clasts; and 5) gray-purple devitrified volcanic clasts with phenocrysts eroded out. Clast shapes are dominantly subangular to subrounded, but vary in some facies from angular to subrounded and cuspate. Flow-banded clast textures are dispersed throughout.

The breccia was divided into four facies (Fig. 4): 1) Facies 1: monomictic breccia with angular to subrounded, cuspate, and jigsaw-fit clast shapes; 2) Facies 2: monomictic breccia with subangular to subrounded and highly fluidal clast shapes; 3) Facies 3: polymictic breccia with angular to subrounded and cuspate clast shapes; and 4) Facies 4: sparsely polymictic breccia with subangular to subrounded and cuspate clast shapes. Facies 1 and 3 are the most common and widespread facies of the breccia of Mammoth Rock. Facies 2 and 4 are much less common and only found in a few locations.

Rinehart and Ross (1964) summarized field observations of the breccia of Mammoth Rock as a microgranular matrix of quartz, plagioclase, and potassium feldspar with angular volcanic clasts and subangular to subrounded metasedimentary clasts. The matrix also includes a small percentage of amphibole, muscovite, biotite, chlorite, clinozoisite, calcite, sphene, apatite, and pyrite with sporadic albite and potassium feldspar granoblasts.

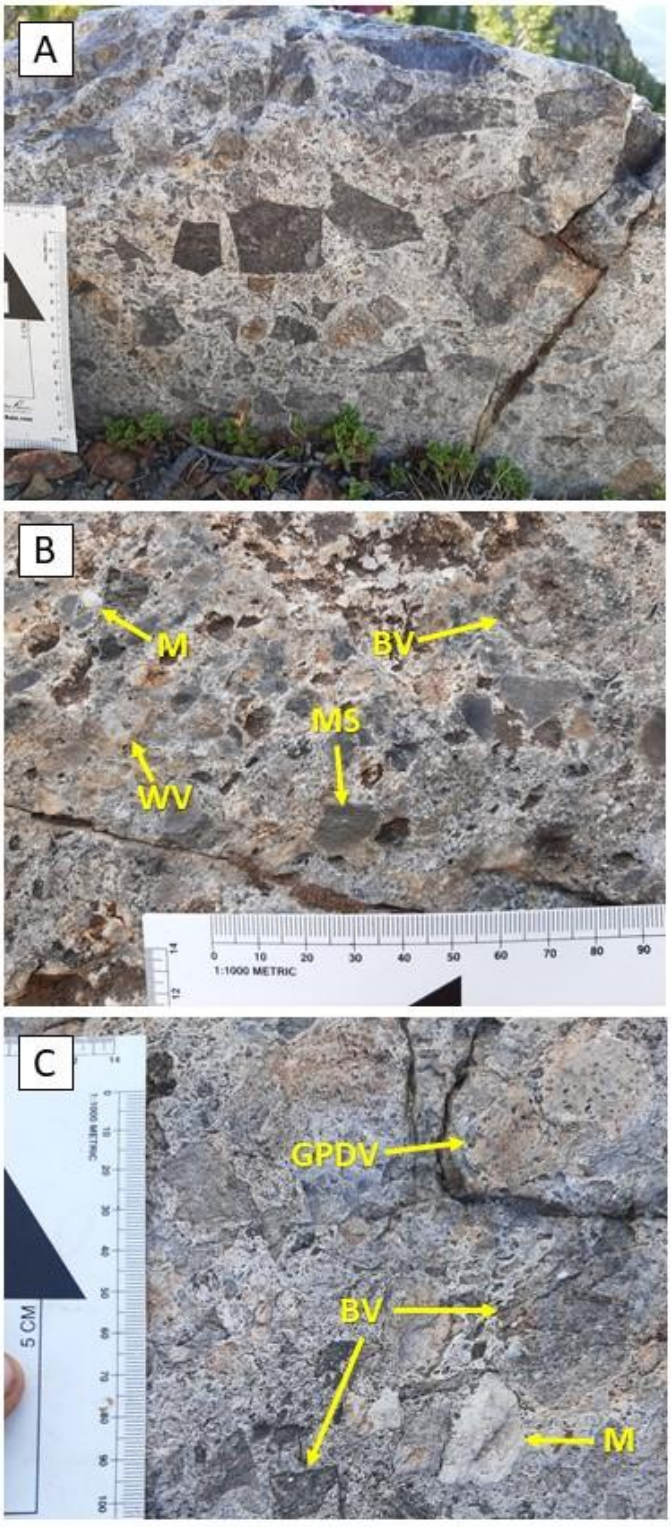

Figure 3. A) Monomictic facies 1 with black volcanic clasts. **B-C)** Polymictic facies with black volcanic clasts with feldspar (BV), white-gray volcanic clasts with pyroxene (WV), white marble clasts (M), gray metasedimentary clasts (MS), and gray-purple devitrified volcanic clasts (GPDV). The white scale card is 15.3 cm long

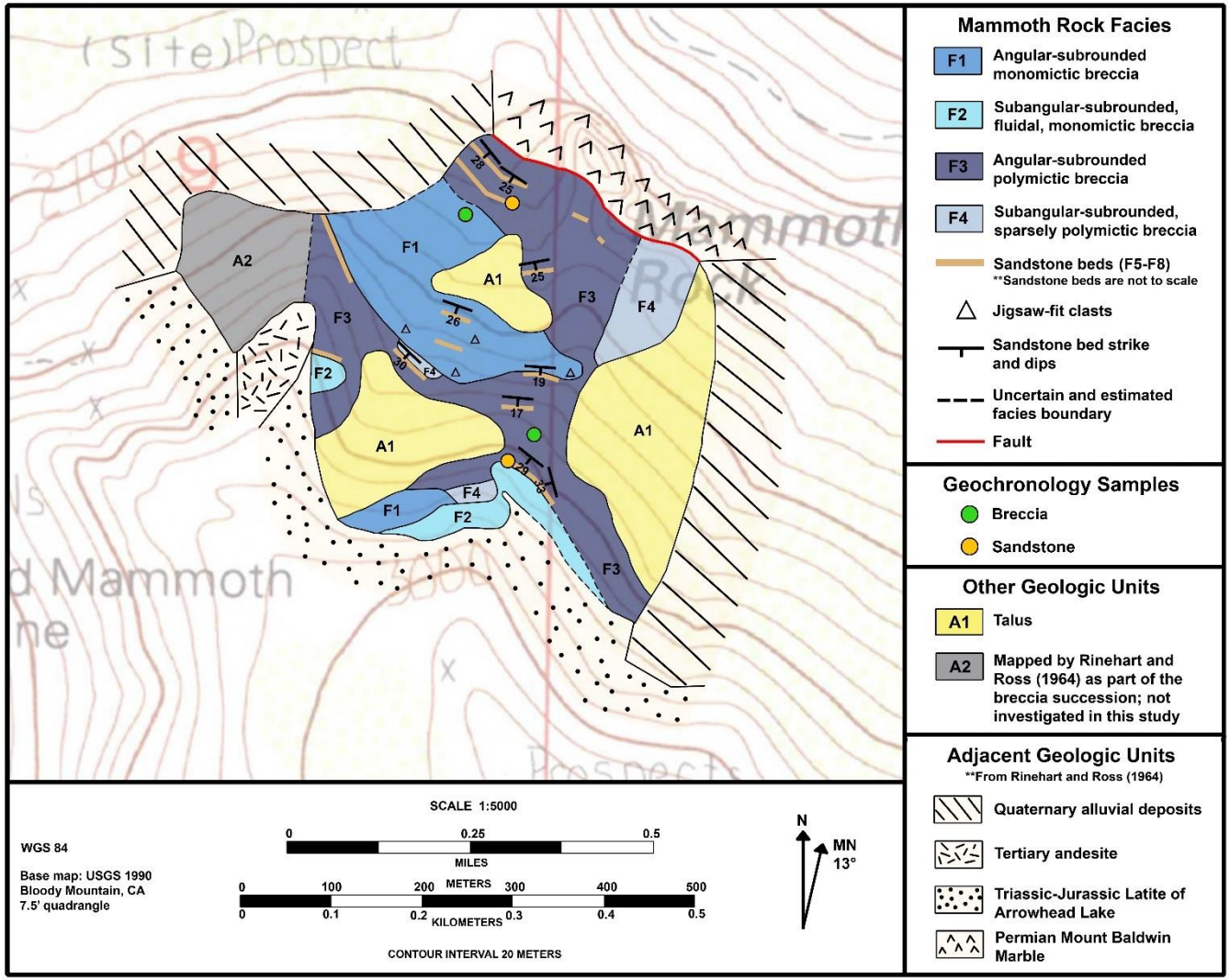

Figure 4. Map of Mammoth Rock facies and contiguous geologic units. Facies 1-8 are labelled F1-F8. F1-F4 (shades of blue) are breccia units. F1 and F3 are the most common breccia facies. Jigsaw-fit clasts are shown on the map by a triangle. F5-F8 (brown) are S-SW dipping sandstone beds. Strike and dip of sandstone beds are displayed on the map. Geochronology sample locations indicated by orange circles for sandstone and green circles for breccia.

Field descriptions of volcanic facies

Facies 1

Facies 1 is very common and is exposed mainly in northwest-central parts of the field area aside from two outliers that lie on the western and southern edges of the field area (Fig. 4). The breccia is monomictic and matrix supported in a fine-grained groundmass. The overall clast modal percentage is 10-30%, but the dominant modal percentage observed in this facies is 20-25% clasts. Clast are 1 mm - 18 cm in diameter, but some very large outliers are up to 70 cm in diameter (Fig. 5C) The breccia clast shapes are dominantly angular to subrounded with cuspate and jigsaw-fit clasts dispersed throughout the facies (Figs. 5A and 5B). Larger clasts are usually angular while the smaller clasts are more subangular to subrounded. Clasts also locally display flow banding. Some clasts display irregular, wavy edges. Clast composition is limited to the black volcanic clasts with 2-5% plagioclase feldspar phenocrysts that are ≤ 1 mm - 4 mm.

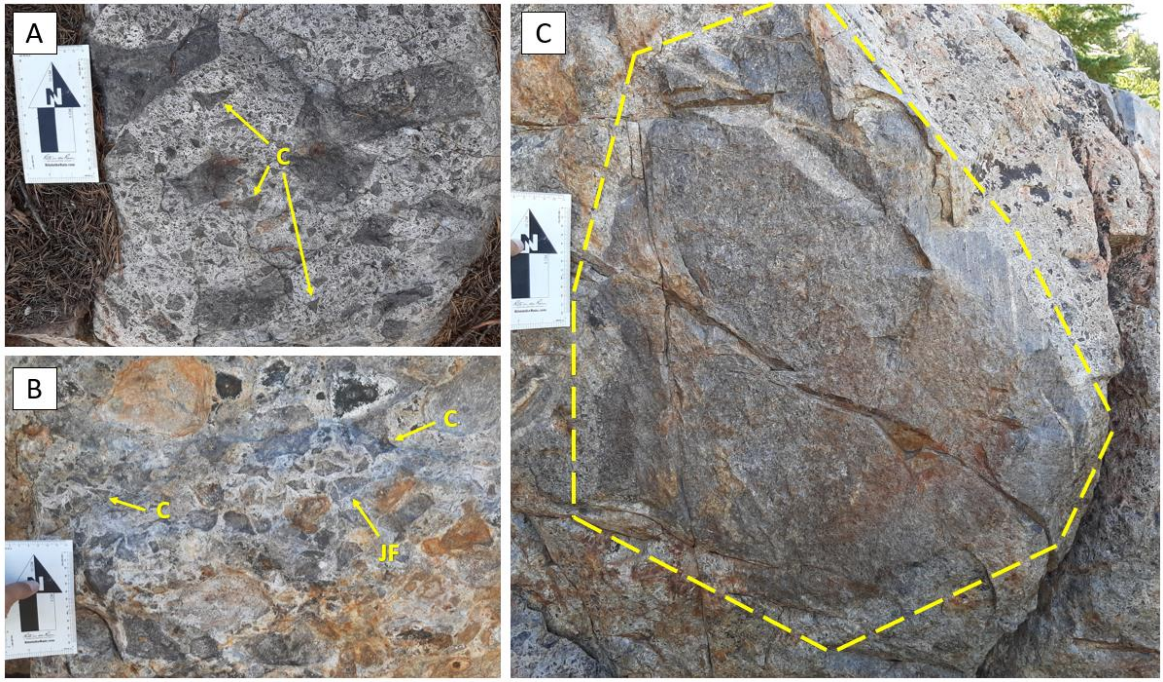

Figure 5. Clasts of the monomictic breccia facies 1. **A-B)** Angular to subrounded clasts with varying sizes of jigsaw-fit (JF) and cuspate (C) clasts. **C)** The largest clast (70 cm) found in facies 1 with an angular to subangular shape. White scale card is 15.3 cm long.

Facies 2

Facies 2 is rare and only exposed in two locations on the southern and western margins of the field area (Fig. 4). The breccia is monomictic and matrix supported in a fine-grained groundmass. Clast modal percentage ranges from 5 to 10% (Figs. 6A and 6B). The higher modal percentages for these highly fluidal facies were found at the boundary of other breccia facies. Clast sizes average 1 mm - 5 cm; however, a few larger outliers are up to 21 cm in diameter. The breccia clast shapes are dominantly fluidal with few subangular to subrounded and cuspate clast shapes (Figs. 6A and 6B). Exposures with larger clasts have a mix of very fluidal-cuspate and typically are along the contact with other facies. Clast composition is limited to the black volcanic clasts with 1-3% plagioclase feldspar phenocrysts that are ≤ 2 mm.

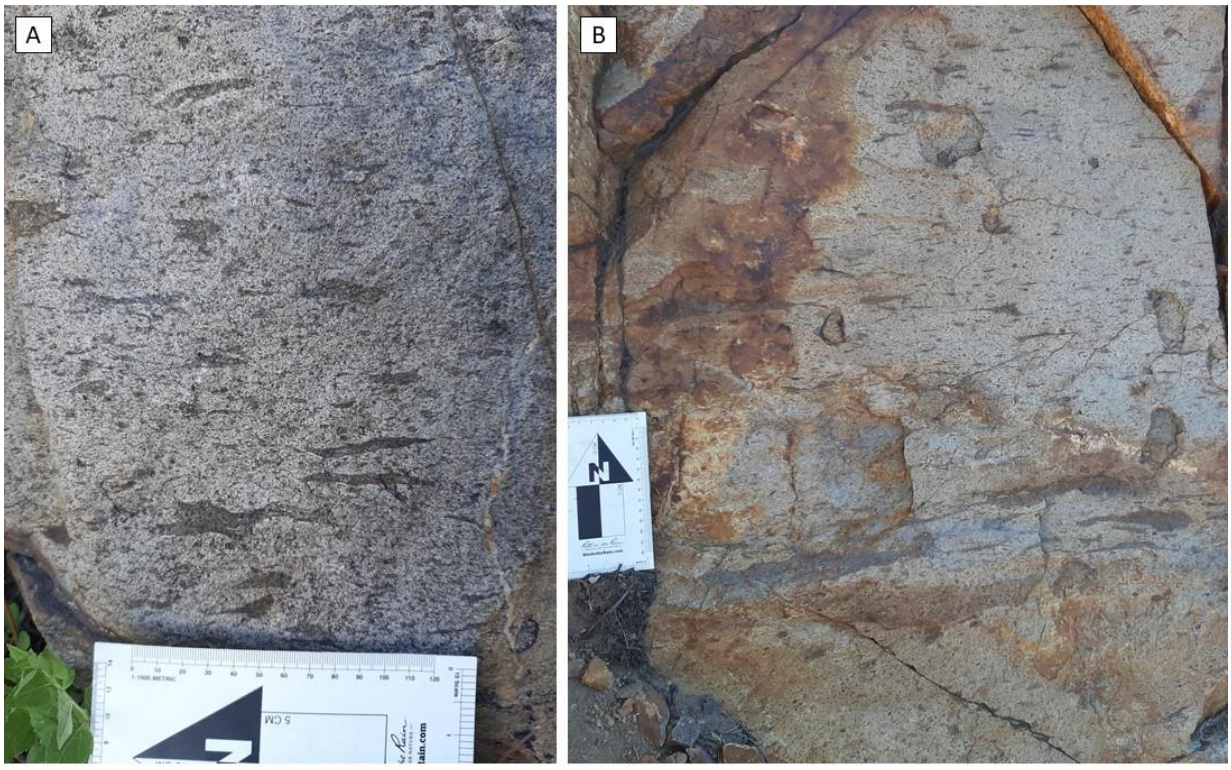

Figure 6. Clasts of the monomictic breccia facies 2. Clasts are highly fluidal. **A)** Fluidal clasts with a modal percentage of 10%. **B)** Fluidal clasts with a modal percentage of 5%. The white scale card is 15.3 cm long.

Facies 3

Facies 3 is the most dominant, widespread breccia facies found in most regions of the field area (Fig. 4). The breccia is polymictic and matrix supported in a fine-grained groundmass. Clast modal percentage is 15-35%. Clast sizes range from 1 mm to 40 cm, but average from 1 mm to 17 cm. The breccia clast shapes are dominantly angular to subrounded with cuspate clasts dispersed throughout the facies (Figs. 7A, 7B, and 7C). Flow-banded clast textures are also observed throughout the facies. Two to five clast compositions are observed (Figs. 7A, 7B, and 7C) depending on the location may include the 1) angular to subrounded black volcanic clasts ranging from 1 mm to 40 cm with 2-20% white feldspar phenocrysts that range from ≤ 1 mm to 6 mm; 2) subangular to subrounded white-gray volcanic clasts ranging from 2 mm to 10 cm with 1-5% black pyroxene phenocrysts ≤ 2 mm; 3) subangular to subrounded marble clasts ranging from 1 mm to 7 cm; 4) angular to subrounded metasedimentary clasts ranging from 1 cm to 4 cm and 5) subangular to subrounded gray-purple devitrified volcanic clasts ranging from 1 cm to 7 cm with phenocrysts eroded out. The facies displays some small (3 mm - 2 cm) pockets of hornblende crystals with white alteration rims in the south-central location of the field area. The facies also displays some minor epidote overprinting on the western edge of the field area. Both the hornblende pockets and epidote alteration are uncommon and only seen in specific locations.

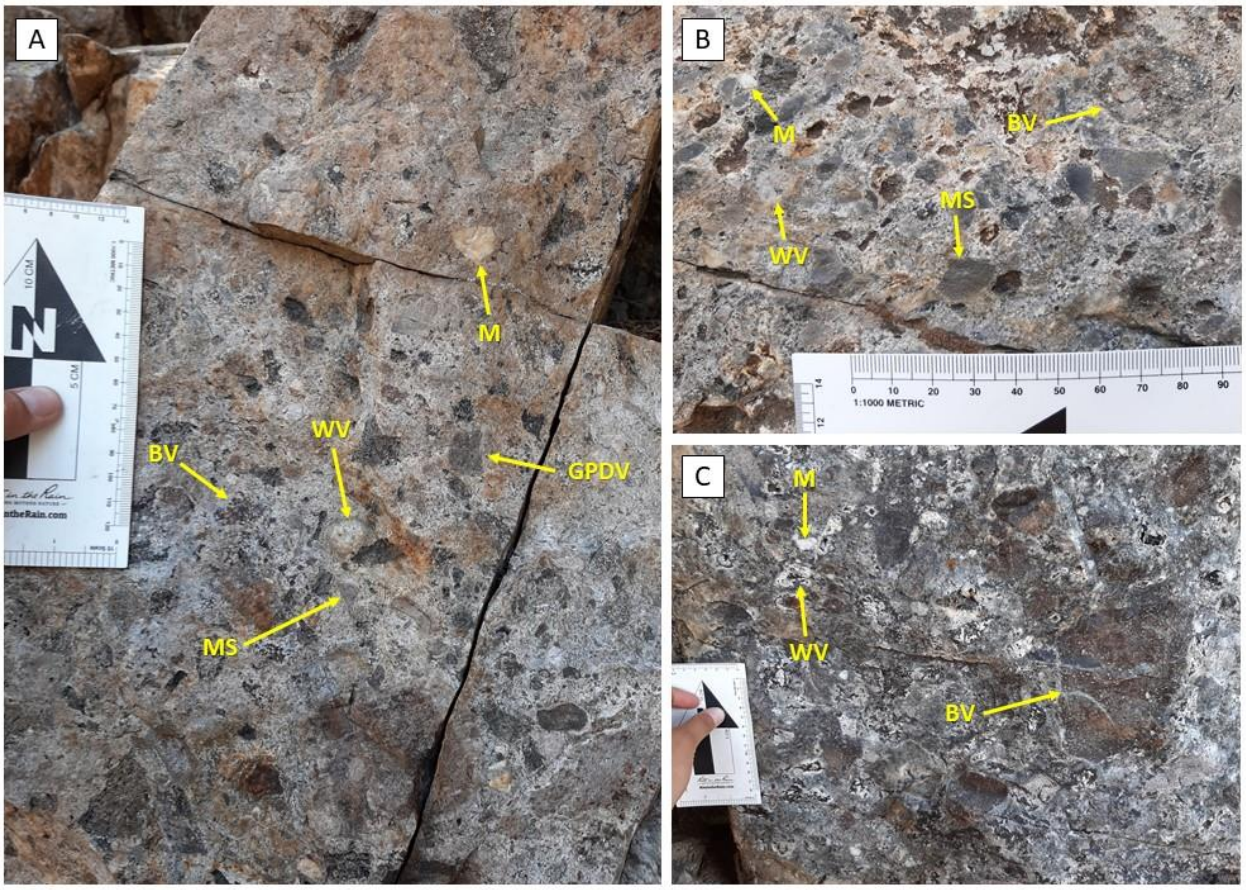

Figure 7. A-C) Clasts of the polymictic breccia facies 3. Polymictic breccia facies include black volcanic clasts with feldspar (BV), white-gray volcanic clasts with pyroxene (WV), white marble clasts (M), gray metasedimentary clasts (MS), and gray-purple devitrified volcanic clasts (GPDV). The white scale card is 15.3 cm long.

Facies 4

Facies 4 is uncommon and mostly exposed in the northeast corner with minor exposures in the central and southern regions of the field area (Fig. 4). The breccia is sparsely polymictic and matrix supported in a fine-grained groundmass. Clast modal percentage ranges from 10 to 20%. Clast sizes range from 1 mm to 12 cm and clast shapes are dominantly subangular to subrounded with cuspate clasts dispersed throughout the facies (Figs. 8A and 8B). Two to five clast types (Figs. 8A and 8B) include the 1) subangular to subrounded black volcanic clasts ranging from 1 mm to 12 cm with 2-10% white feldspar phenocrysts that range from ≤ 1 mm to

4 mm; 2) subangular to subrounded white-gray volcanic clasts that are ≤ 3 cm with 1-3% black pyroxene phenocrysts ≤ 2 mm; 3) subangular to subrounded marble clasts that are ≤ 3 cm; 4) subangular to subrounded metasedimentary clasts that are ≤ 2.5 cm and 5) subangular to subrounded gray-purple volcanic clasts that are ≤ 3 cm with phenocrysts eroded out. The dominant clast in this facies is the black volcanic clast (type 1). The facies has ≤ 1% of each of the remaining clast types. The sparsely polymictic facies 4 generally has smaller clasts than polymictic breccia facies 3 for all clast types.

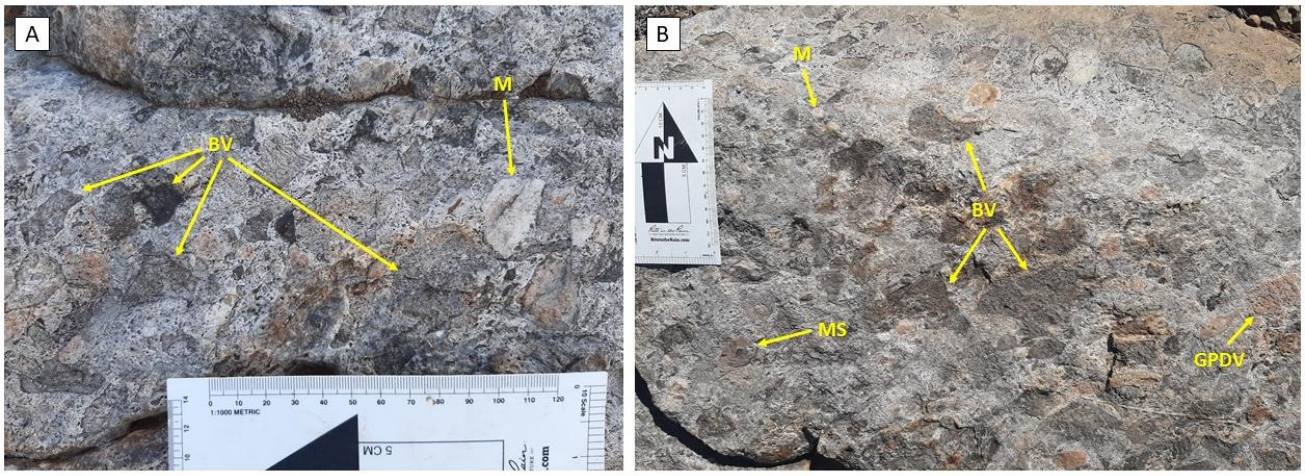

Figure 8. A-B) Clasts of the sparsely polymictic breccia facies 4. The BV clast is the most dominant and there are ≤ 1% of each of the other clast types. The sparsely polymictic breccia outcrops may have any of the five clast types including black volcanic clasts with feldspar (BV), white-gray volcanic clasts with pyroxene (WV), white marble clasts (M), gray metasedimentary clasts (MS), and gray-purple devitrified volcanic clasts (GPDV). **A)** Sparsely polymictic breccia showing the dominant BV clast with ≤ 1% of M clasts. **B)** Sparsely polymictic breccia showing the dominant BV clast with ≤ 1% of the M, MS, and GPDV clasts. The white scale card is 15.3 cm long.

4.2 SANDSTONE OF MAMMOTH ROCK

Sandstone beds are dispersed throughout the breccia facies (Fig. 4). Grain size varies throughout the sandstone beds from fine to coarse. Sandstone beds are crystalline due to low-grade metamorphism. Some beds have randomly dispersed breccia lenses or breccia clasts. Other beds have either no grading, poor grading of clasts and sand grains, or very rare low-angle tabular cross-bedding. Overall, the sandstone beds range in thickness from 14 cm to 2.5 m, but the average thickness ranges from 14 cm to 30 cm. The beds strike NE-SW to E-W and dip S-SW with dip angles ranging from 17 to 33 degrees.

The four facies of sandstone beds are: 1) Facies 5: planar-laminated sandstone; 2) Facies 6: planar-laminated sandstone with breccia lenses; 3) Facies 7: cross-bedded sandstone; and 4) Facies 8: massive sandstone with breccia clasts. Sandstone facies 6-8 are much less common than facies 5 and only found in a few locations.

Field descriptions of sandstone facies

Facies 5: Planar-laminated sandstone beds are the most common sedimentary facies (Figs. 9A, 9B, and 9C). Bed thickness ranges from 14 cm to 1 m. Laminations vary in thickness from 1 mm to 3 cm. Beds consist of alternating fine- to medium-grained or alternating medium to coarse-grained layers.

Figure 9. A-C) Planar laminated sandstone facies of Mammoth Rock (facies 5). Planar laminated sandstone layers alternate in grain size and vary in thickness. The white scale card is 15.3 cm long.

Facies 6: The planar-laminated sandstone with breccia lenses (Fig. 10) is rare and only found in one location. The thickness of this sandstone facies ranges from 14 cm to 50 cm. Laminations vary in thickness from 2 mm to 2 cm. The sandstone beds consist of alternating fine- to medium-grained or medium- to coarse-grained layers. Subangular to subrounded clasts are found dispersed throughout the facies and are poorly sorted. Clasts in the basal layers of facies 6 are 2 mm - 1 cm and clasts in the upper layers are 1 cm - 3 cm. The breccia lenses range from 10 cm to 22 cm in length. Breccia clasts within the lenses include the white-gray volcanic, marble, and gray-purple devitrified volcanic clasts.

Figure 10. Planar laminated sandstone with a breccia lens indicated by yellow arrow (facies 6). The white scale card is 15.3 cm long.

Facies 7: The cross-bedded sandstone (Figs. 11A and 11B) is only exposed in two locations. Bed thickness ranges from 60 cm to 1.5 m. The facies have low-angle tabular cross-bedding and range from very fine to coarse grained. The sandstone beds are not graded.

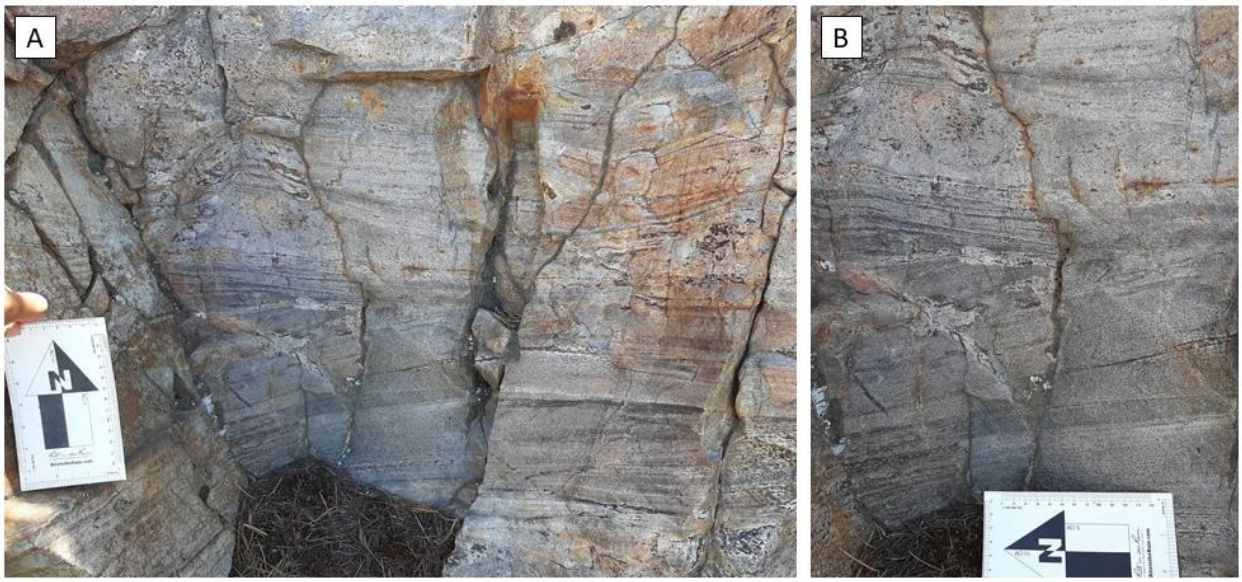

Figure 11. A-B) Low-angle tabular cross-bedded sandstone (facies 7). The white scale card is 15.3 cm long.

Facies 8: The massive sandstone with breccia clasts exposed in two locations. Bed thickness ranges from 50 cm to 2.5 m. Sand grains are medium to coarse. Clasts within the facies are hard to distinguish due to very weathered and oxidized sandstone beds. The massive sandstone is ungraded and breccia clasts are randomly distributed throughout the facies. Clasts are subangular to subrounded, ≤ 1 mm - 10 cm, white and dark gray clasts that are marble and black volcanic, respectively.

5. RESULTS

5.1 PETROGRAPHY OF THIN SECTIONS

A fine-grained groundmass makes up 85% - 95% of the rock with variable amounts of alteration to epidote, sericite or chlorite (Figs. 12, 13, 14, and 15). Samples display minor (Figs. 12 and 13) to major (Figs. 14 and 15) alteration of the groundmass. Detailed hand sample and thin section descriptions for each breccia sample can be found in Appendix B. Detailed descriptions of the corresponding facies for each breccia sample are in section 4 under rock descriptions.

Phenocrysts constitute 5% - 15% of the breccia. The phenocrysts include 2% - 8% subhedral to anhedral plagioclase; 1-2% subhedral to anhedral potassium feldspar, ≤ 2% euhedral to anhedral hornblende; ≤ 2% subhedral to anhedral quartz and biotite; ≤ 2% anhedral oxides; ≤ 1% euhedral to anhedral muscovite; ≤ 1% anhedral clinopyroxene; and ≤ 1% subhedral zircon. Glomerocrysts constitute ≤ 2% of the breccia. Phenocrysts in the glomerocrysts vary in each sample, but they are dominantly composed of plagioclase and/or quartz with minor amounts of biotite, muscovite, hornblende, clinopyroxene, oxides, sericite alteration, and/or chlorite alteration.

Various magmatic reactions and petrographic textures were observed including altered phenocrysts of dominantly plagioclase (Figs. 12, 13, and 15), resorption of plagioclase phenocrysts, rare zoning of plagioclase, exsolution lamellae on potassium feldspar phenocrysts, undulose extinction of quartz, alteration of phenocrysts through secondary mineral growth of quartz (Fig. 12) and plagioclase**,** and minor to major alteration of the groundmass through secondary mineral growth of sericite, chlorite and epidote (Figs. 12, 13, 14, and 15). Zoning and resorption textures indicate disequilibrium in the magma system, which can result from multiple

processes. Zoning is produced in solid-solution crystals as a result of continuous reactions between the crystal and the melt as thermal and chemical changes occur. Zoning forms during magma evolution through processes like injections of new magma into the existing magma chamber, magma mixing (Shcherbakov et al., 2011), or decompression (Humphreys et al., 2006). As the magma evolves, crystals such as plagioclase, cool and undergo chemical differentiation, causing zonation as the crystal changes high- to low-temperature compositional end members (Ginibre et al., 2007). Resorption occurs as a result of interaction between the melt and crystals through decompression, undersaturation and magma mixing (Hattori and Sato, 1996; Chang and Meinert, 2004). Glomerocrysts can form during crystallization or resorption (Hogan, 1993). Glomerocrysts formed during crystallization are joined along euhedral faces that result from crystals drifting together and attaching to one another. Glomerocrysts formed during resorption are joined along irregular, anhedral faces, or embayed margins that are produced when the boundary layer melt envelops dissolving crystals that create a supersaturated melt composition resulting in crystallization of new material in the boundary layer melt, bonding the resorbed crystals together. Exsolution lamellae form through dissolution of fine crystals at high metamorphic temperatures or pressures and are produced when the host mineral loses solubility resulting in exsolution through cooling to low temperatures or decompression to low pressures (Song and Cao, 2021). Undulose extinction of quartz indicates the rock was subject to stress by deformation or metamorphism (Young, 1976).

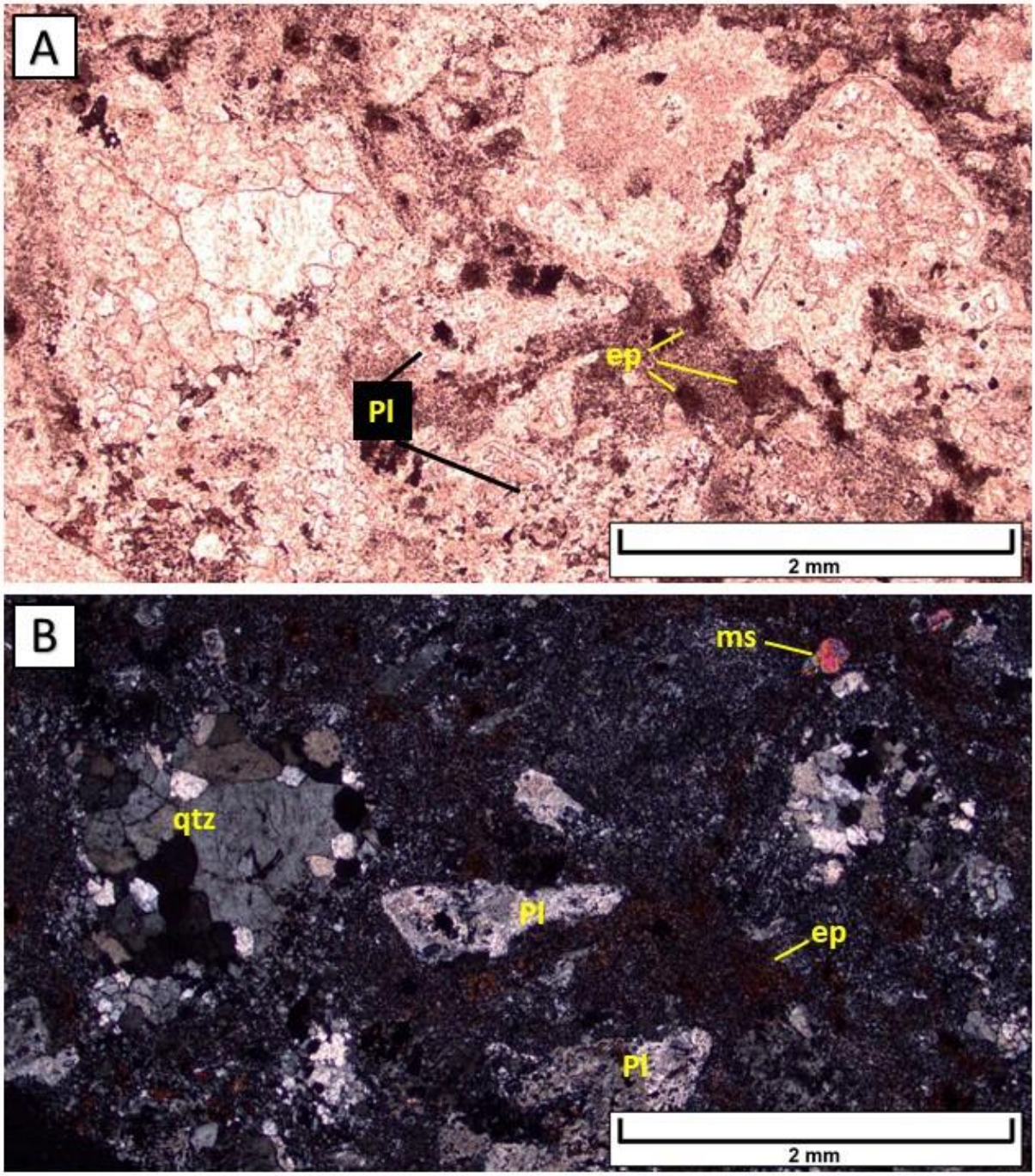

Figure 12. Photomicrograph of sample 8230-1D from facies 3 at 2x magnification. **A)** Image in plane-polarized light showing minor epidote (ep) alteration of the groundmass and spotty alteration of plagioclase phenocrysts (Pl). **B)** Image in cross-polarized light shows plagioclase phenocrysts (Pl) with secondary muscovite (ms) crystal growth in a fine-grained groundmass with epidote alteration (ep) and secondary mineral growth of quartz (qtz).

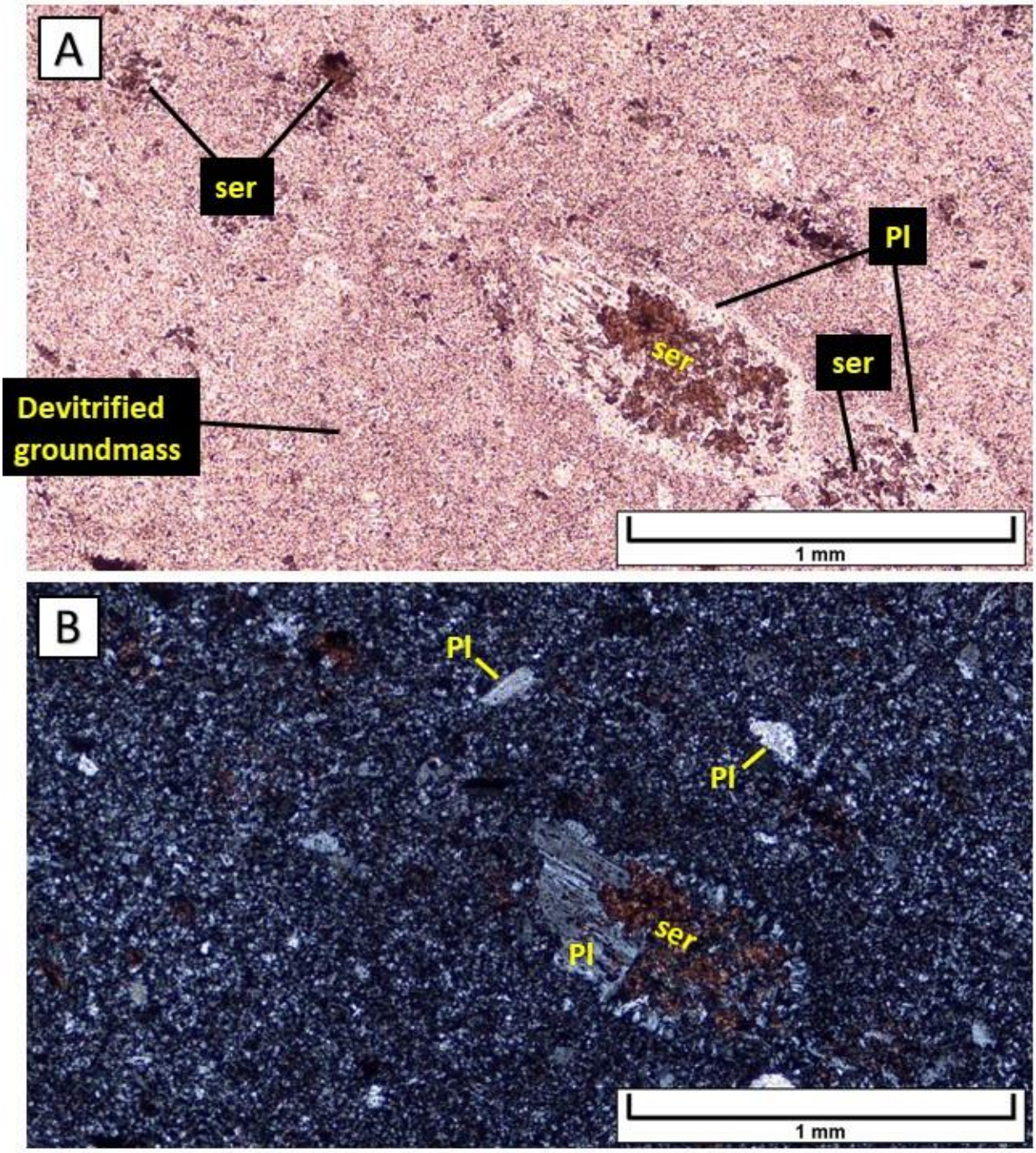

Figure 13. Photomicrograph of sample 72720-2C from facies 3 at 4x magnification. **A)** Image in plane-polarized light differentiates the devitrified groundmass from minor sericite (ser) alteration of the groundmass and shows abundant sericite alteration within a plagioclase phenocryst (Pl). **B)** Image in cross-polarized light shows some small plagioclase phenocrysts (Pl) and a large plagioclase phenocryst with sericite (ser) alteration in a fine-grained groundmass with minor epidote (ep) alteration.

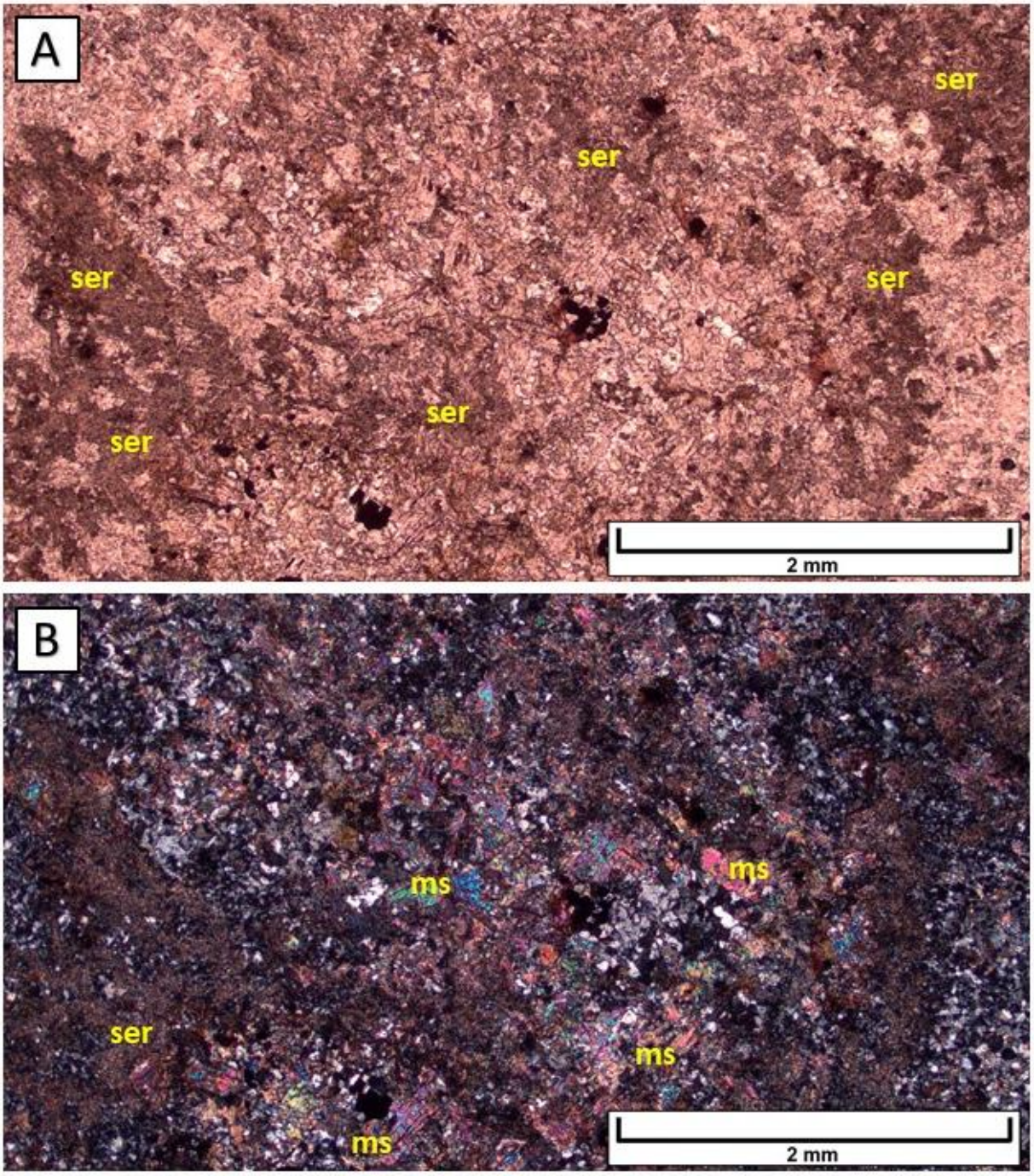

Figure 14. Photomicrograph of sample 727920-4A from facies 3 at 2x magnification. **A)** Image in plane-polarized light shows major sericite (ser) alteration of the groundmass. **B)** Image in cross-polarized light shows abundant sericite (ser) alteration of the fine-grained groundmass with secondary muscovite (ms) crystal growth.

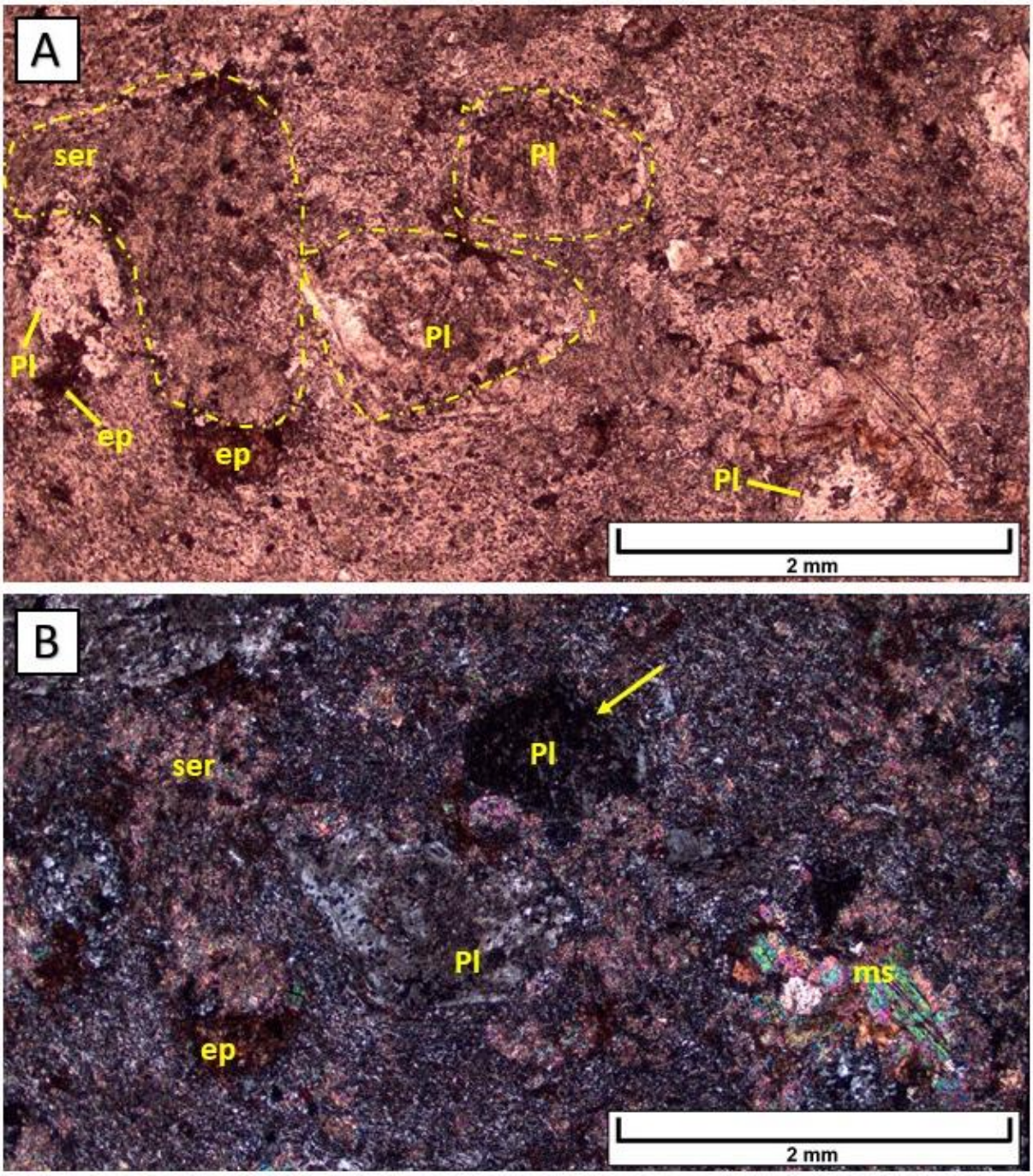

Figure 15. Photomicrograph of sample 727920-5A from facies 3 at 2x magnification. **A)** Image in plane-polarized light shows abundant sericite (ser) and moderate epidote (ep) alteration of the groundmass with highly altered spotty plagioclase phenocrysts (Pl). **B)** Image in cross-polarized light shows plagioclase (Pl) phenocryst with abundant sericite (ser) and epidote (ep) alteration of the fine-grained groundmass with secondary muscovite (ms) crystal growth. Highly altered mineral (yellow arrow) is likely plagioclase.

5.2 GEOCHEMISTRY

Whole-rock major and trace element geochemical analyses (Table 1) provide valuable data and insight into the tectonic and magmatic conditions during early arc genesis. Geochemical analyses were conducted on ten clasts from monomictic facies 1 and polymicitic facies 3 that were dominantly subangular in shape, with few angular and subrounded clasts. Zircon geochemical data were collected to supplement the whole-rock geochemical data providing information for an analysis of crustal thickness based on U/Yb concentrations, which allows for the interpretation of the tectonic and magmatic processes and paleogeography of the arc.

5.2.1 MAJOR ELEMENT GEOCHEMISTRY

The clasts in the breccia of Mammoth Rock displays an SiO_2 range between 53 and 67 weight % (Table 1). All of the breccia samples except one outlier fall into the typical andesite silica range. One sample is dacitic in composition. The clast data show a wide range of compositions on the total-alkali silica (TAS) diagram (Fig. 16). The breccia of Mammoth Rock has high K_2O weight % and low Na_2O weight %. The high K_2O weight % of the breccia results in a very high total alkali content. Breccia clast compositions ranging from basaltic trachyandesite to trachydacite, and rare rocks types including tephri-phonolite and phono-tephrite (Field, 2018) are a result of this high total alkali content (Fig. 17). The breccia of Frog Lakes (Fig. 17; Roberts, 2014; Savage, 2021) has a narrow range of clast compositions on the TAS diagram. Overall silica contents of the clasts from breccia of Frog Lakes have a lower range between 48 and 63 weight %.

IGSN #	*IE421001I*	*IE421001J*	*IE421001K*	*IE421001L*	*IE421001MX*	*IE421001N*	*IE421001O*	*IE421001P*	*IE421001Q*	*IE421001R*
Sample	**72720-2E**	**72920-5A**	**72920-5C**	**73020-1A**	**73020-1B**	**73020-1C**	**8230-1B**	**8230-1D**	**8230-3A**	**8230-3B**
SiO_2	58.94	61.73	53.99	53.82	67.05	61.29	54.86	62.49	60.43	60.20
TiO_2	0.37	0.31	0.36	0.36	0.27	0.31	0.36	0.39	0.39	0.39
Al_2O_3	20.01	19.63	25.70	25.12	15.79	19.65	21.08	19.51	20.57	20.47
Fe_2O_3	5.62	2.47	2.73	2.73	2.61	2.77	6.10	2.62	2.37	2.38
MnO	0.24	0.11	0.12	0.13	0.09	0.14	0.29	0.11	0.14	0.14
MgO	2.06	0.96	1.05	0.99	0.82	1.07	2.16	0.84	1.21	1.21
CaO	3.45	0.98	2.11	3.06	1.01	1.70	5.63	2.49	3.45	3.45
Na_2O	3.78	1.42	1.54	2.16	1.76	1.12	3.32	4.46	4.03	4.01
K_2O	4.01	10.35	9.70	8.38	8.09	9.63	3.72	5.82	6.08	6.07
P_2O_5	0.10	0.07	0.07	0.09	0.07	0.07	0.12	0.14	0.14	0.14
LOI	1.15	1.56	2.22	2.78	2.01	1.82	2.06	0.82	0.81	1.17
Sc	6.48	4.45	3.94	4.52	3.07	4.26	6.18	5.95	4.93	4.60
V	82.67	29.35	31.24	27.67	17.22	22.72	81.60	48.69	61.41	58.50
Cr	3.76	0.94	0.93	1.19	1.11	0.99	3.31	2.16	2.31	2.52
Co	7.07	1.72	1.81	1.88	3.18	1.81	7.27	2.38	2.10	2.12
Ni	6.49	1.16	1.40	1.53	1.55	1.82	5.28	2.58	3.33	2.83
Rb	275.77	342.46	420.08	412.92	294.59	371.98	270.33	217.72	285.77	270.32
Sr	194.48	245.34	194.25	176.45	95.65	174.38	228.68	208.10	195.24	188.61
Y	15.61	14.67	12.77	16.74	11.68	12.99	17.82	14.42	13.21	13.11
Zr	174.34	202.88	196.78	232.16	157.10	175.78	176.33	159.36	139.91	137.39
Nb	11.13	13.78	12.91	14.47	10.69	11.36	11.18	11.03	11.18	10.48
Cs	28.08	18.29	22.24	14.85	11.05	14.34	30.01	14.11	21.37	20.28
Ba	1775.72	2433.27	2518.65	3466.01	3289.86	2880.10	1906.25	2063.62	2628.96	2571.38
La	29.83	25.13	20.59	25.45	20.82	21.24	28.04	12.97	10.63	10.20
Ce	55.80	46.57	38.01	45.38	36.20	37.96	51.99	25.32	22.59	21.48
Pr	6.54	5.14	4.21	4.93	3.99	4.14	6.05	3.08	2.77	2.63
Nd	19.17	14.64	11.94	13.81	11.13	11.51	17.86	9.57	8.62	8.54
Sm	3.70	2.92	2.31	2.67	2.05	2.08	3.50	2.05	2.00	2.02
Eu	1.07	0.79	0.66	0.72	0.51	0.59	1.10	0.61	0.50	0.49
Gd	3.19	2.92	2.81	3.08	2.67	2.75	3.35	2.46	2.42	2.49
Tb	0.41	0.39	0.33	0.39	0.30	0.31	0.47	0.35	0.31	0.32
Dy	2.34	2.22	1.95	2.45	1.86	2.07	2.76	2.22	2.10	2.05
Ho	0.42	0.38	0.34	0.44	0.32	0.36	0.48	0.38	0.36	0.37
Er	1.71	1.42	1.34	1.68	1.23	1.35	1.84	1.55	1.35	1.37
Tm	0.28	0.25	0.23	0.29	0.21	0.23	0.31	0.25	0.24	0.23
Yb	1.83	1.65	1.55	1.89	1.35	1.48	1.97	1.63	1.49	1.51
Lu	0.28	0.26	0.23	0.30	0.22	0.23	0.29	0.25	0.23	0.23
Hf	4.39	5.10	4.98	5.86	4.03	4.60	4.49	4.17	3.61	3.59
Ta	1.37	1.47	1.46	1.68	1.31	1.32	1.27	1.26	1.23	1.20
Pb	22.65	37.56	37.84	37.95	12.05	39.93	23.93	41.85	40.98	39.93
Th	14.76	16.58	16.02	18.30	12.95	14.63	14.82	12.66	11.23	10.96
U	4.64	4.70	5.14	5.12	4.25	4.21	4.71	3.87	3.73	3.53

Table 1. Whole-rock geochemical data for the 10 clasts of the breccia of Mammoth Rock with the sample name and associated IGSN number.

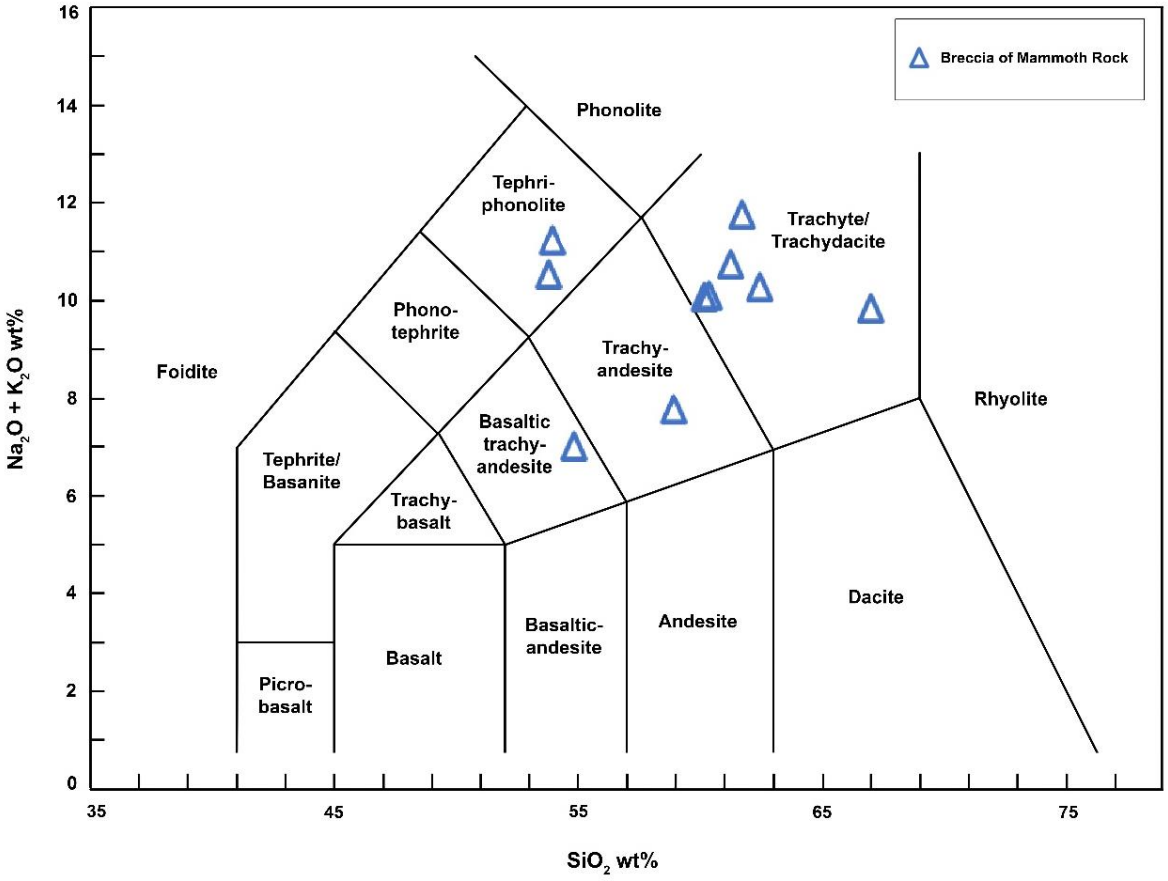

Figure 16. TAS diagram of clasts from the breccia of Mammoth Rock (BMR) for rock classification (modified from Le Bas et al., 1986). BMR clast compositions range from andesitic to dacitic.

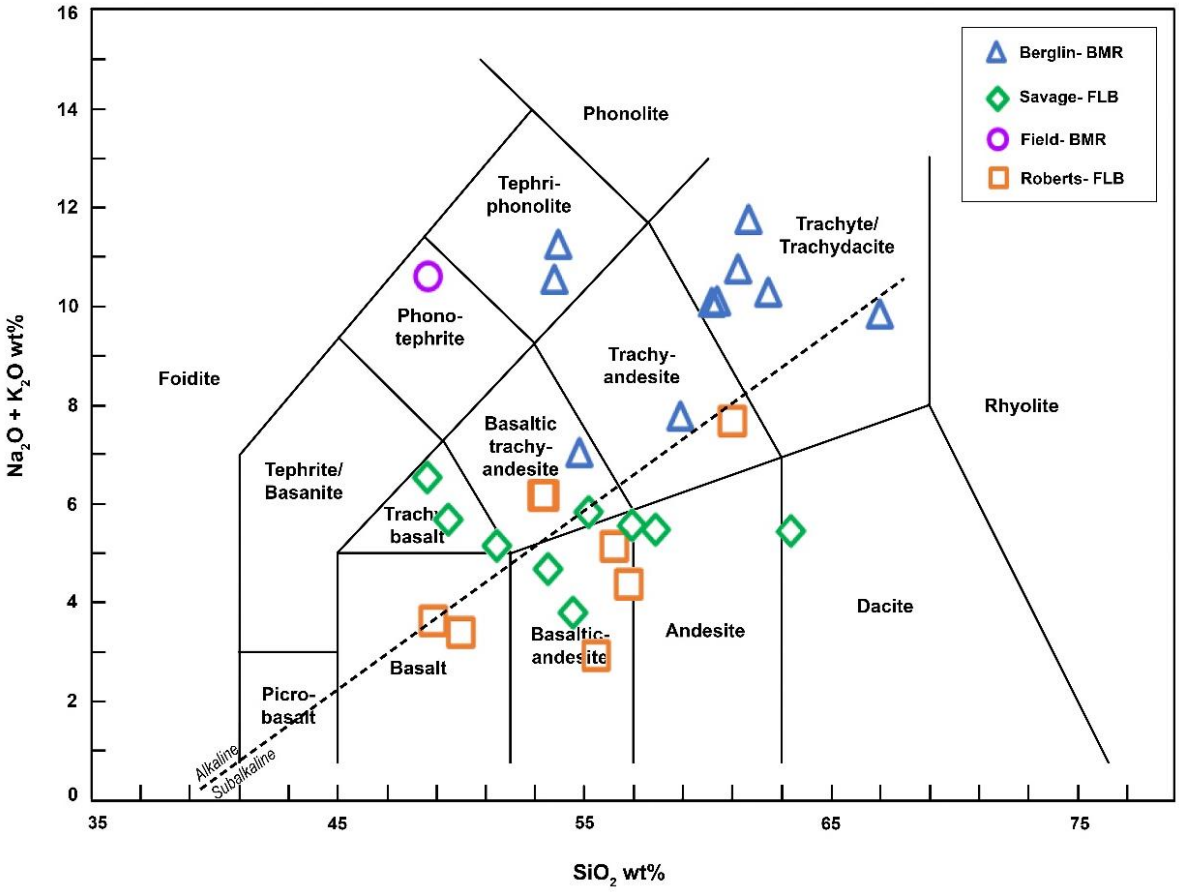

Figure 17. TAS diagram of the clasts from breccia of Mammoth Rock (BMR) and breccia of Frog Lakes (FLB) samples (modified from Le Bas et al., 1986). BMR clast compositions range from andesitic to dacitic. FLB compositions range from basaltic to andesitic. Bold dashed line denotes alkaline rocks (above line) and subalkine rocks (below line).

Harker diagrams are used to understand fractional-crystallization processes in magma systems as well as other processes including partial melting, crustal contamination and magma mixing by plotting the weight % of various major element oxides against SiO_2 (Wilson, 1994). Harker diagrams graphically show trends of evolving magma systems and often show the evolution of multiple batches of magma from a highly evolved magma chamber that are generally similar in chemistry (Wilson, 1994). K_2O and Al_2O_3 particularly have high weight %

concentrations in some clasts (Fig. 18). Additionally, geochemical analysis and fractional crystallization trends indicate the geochemical reservoirs that contributed to the evolution of magma. Primitive and evolved magma systems can be differentiated by their Al_2O_3 weight % and Mg#. The values for the breccia of Mammoth Rock range from 15.79 to 25.70 Al_2O_3 weight % (Fig. 18) and 40.6 - 41.2 Mg#.

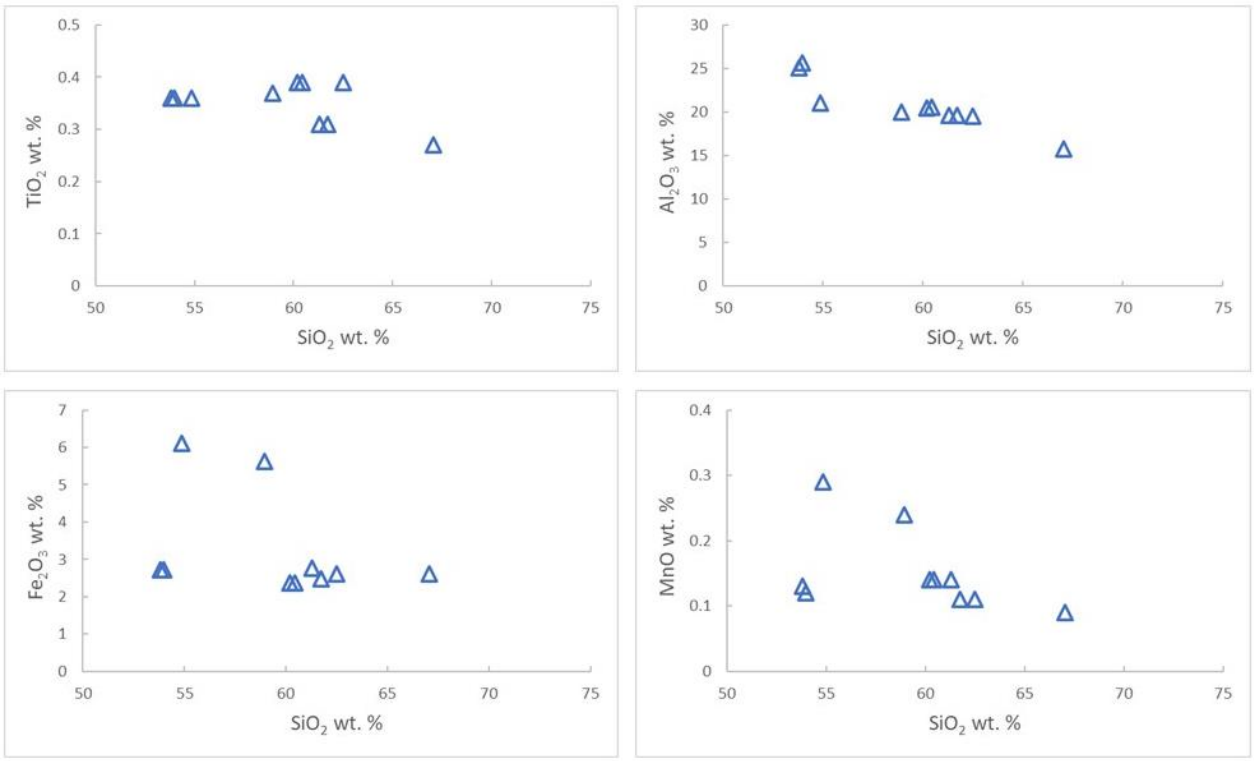

Figure 18a. Harker variation diagrams of SiO_2 versus major element oxides for clasts from the breccia of Mammoth Rock.

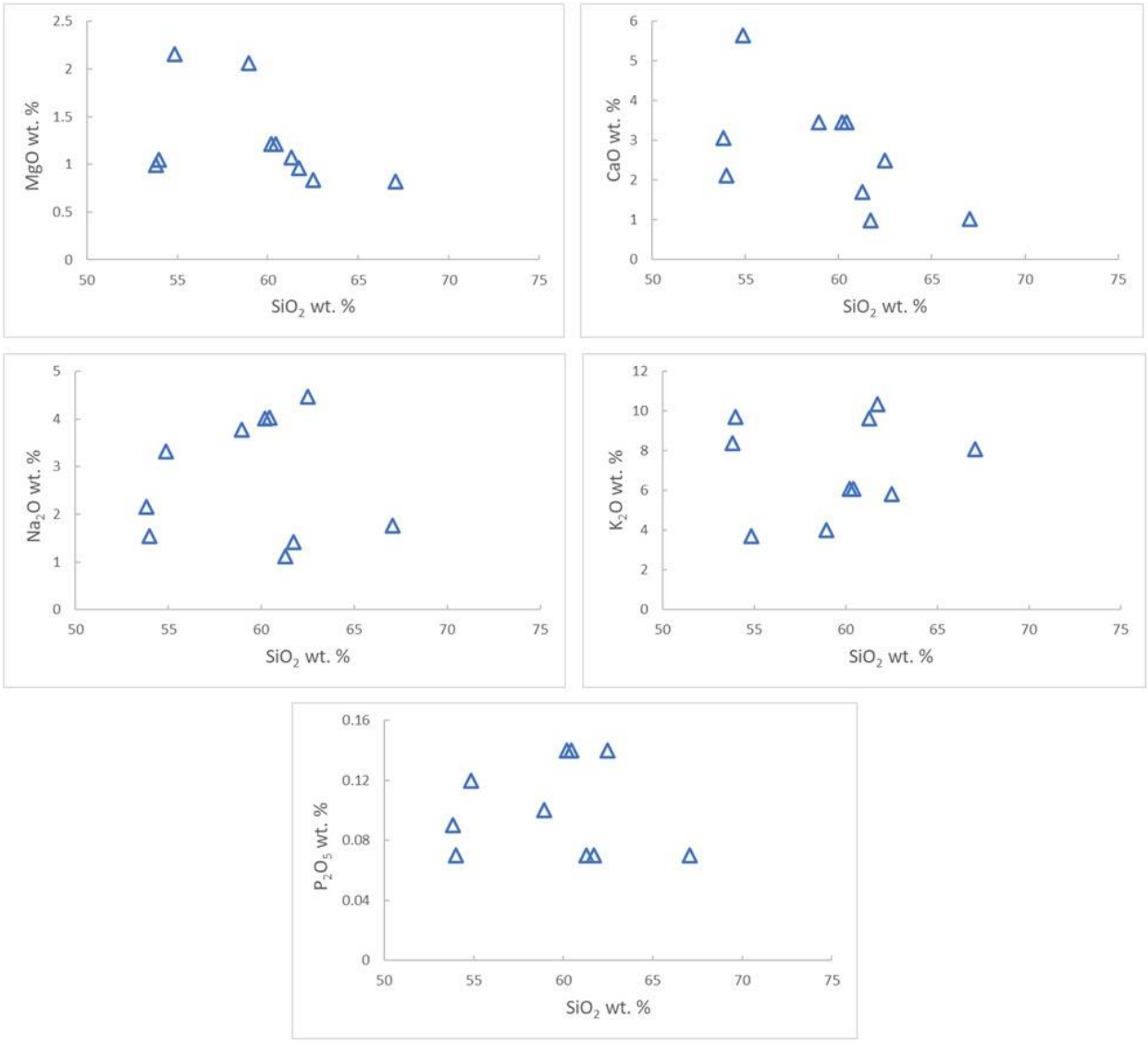

Figure 18b. Harker variation diagrams of SiO_2 versus major element oxides for clasts from the breccia of Mammoth Rock.

5.2.2 TRACE ELEMENT GEOCHEMISTRY

Trace element data are important to use in conjunction with major element data. Analysis of mobile and immobile trace elements are essential for understanding magmatic rocks that have been subjected to metasomatism, hydrothermal activity, and metamorphism. Major elements such as K, Na, and other large ion lithophile elements (LILE) are often mobilized during metamorphism and hydrothermal alteration, whereas elements like high field strength elements (HFSE), rare earth elements (REE), and transition metals are typically immobile making them more reliable elements for classifying rocks, determining magma petrogenesis, and determining the tectonic environment associated with the magmatism (Lin et al., 2016; Han et al., 2018). The immobile trace elements are particularly reliable for the breccia of Mammoth Rock since magma was generated through subduction and clasts were deposited in a shallow-marine environment and affected by low-grade metamorphism.

To supplement the TAS diagram and major element data, a SiO_2 versus immobile trace elements Nb/Y plot was created (Fig. 19; Winchester and Floyd, 1977). The compositions of the breccia clasts of Mammoth Rock based on SiO_2 versus Nb/Y plot are much more andesitic than the compositions on the TAS diagram. The majority of the breccia clasts are classified as trachyandesite (Fig. 19).

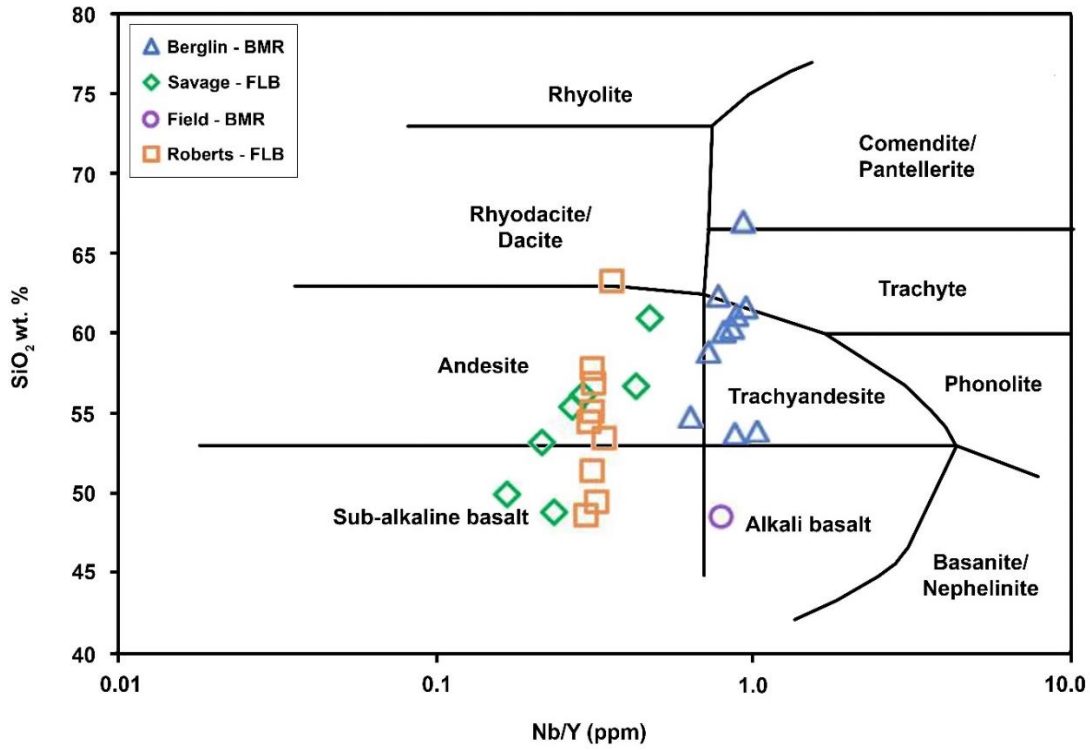

Figure 19. Discrimination plot of SiO2 versus trace elements Nb/Y to determine composition and rock classification (modified from Winchester and Floyd, 1977).

A discrimination plot of Zr/Y versus Zr is used to differentiate continental arcs from oceanic arcs (Fig. 20; Pearce, 1983). High-field-strength elements (HFSE) like zirconium are used for analyses associated with hydrothermal systems since they are typically immobile and very incompatible elements. All of the breccia of Mammoth Rock clasts are classified as continental arc rocks and cluster together; however, many of the breccia of Frog Lakes samples are borderline ocean-continental arc (Fig. 20). The breccia of Frog Lakes data show a positive slope from ocean arc to continental arc. A positive trendline is also observed between the breccia of Mammoth Rock and breccia of Frog Lakes transitioning from borderline ocean-continental arc to continental arc.

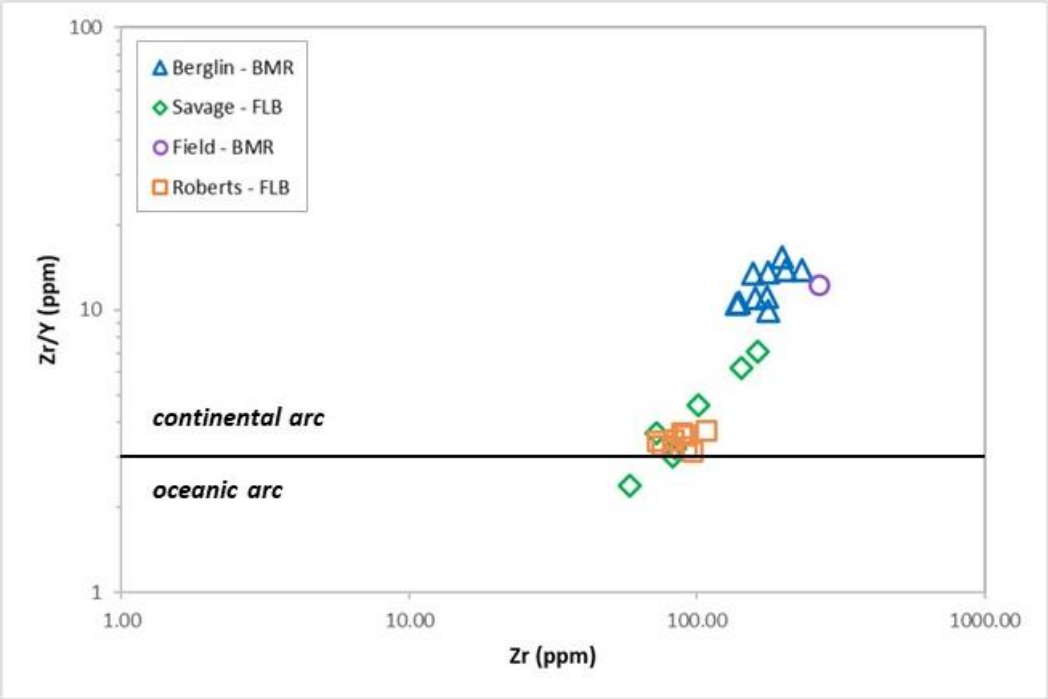

Figure 20. Discrimination plot of arc type for clasts from the breccia of Mammoth Rock (BMR) and breccia of Frog Lakes (FLB) (Pearce, 1983).

.

The Th/Yb versus Ta/Yb plot is used to differentiate magmatic settings for ocean arcs, active continental margins, MORB, and intra-plate settings (Fig. 21; Pearce, 1983). Both clasts from the breccia of Mammoth Rock and breccia of Frog Lakes data plot within the active continental margin aside from one outlier sample from the breccia of Frog Lakes (Fig. 21). Similar to the Zr/Y versus Zr plot, the breccia of Mammoth Rock data and breccia of Frog Lakes clast data show a positive slope from ocean arc to active continental margin (Fig. 21).

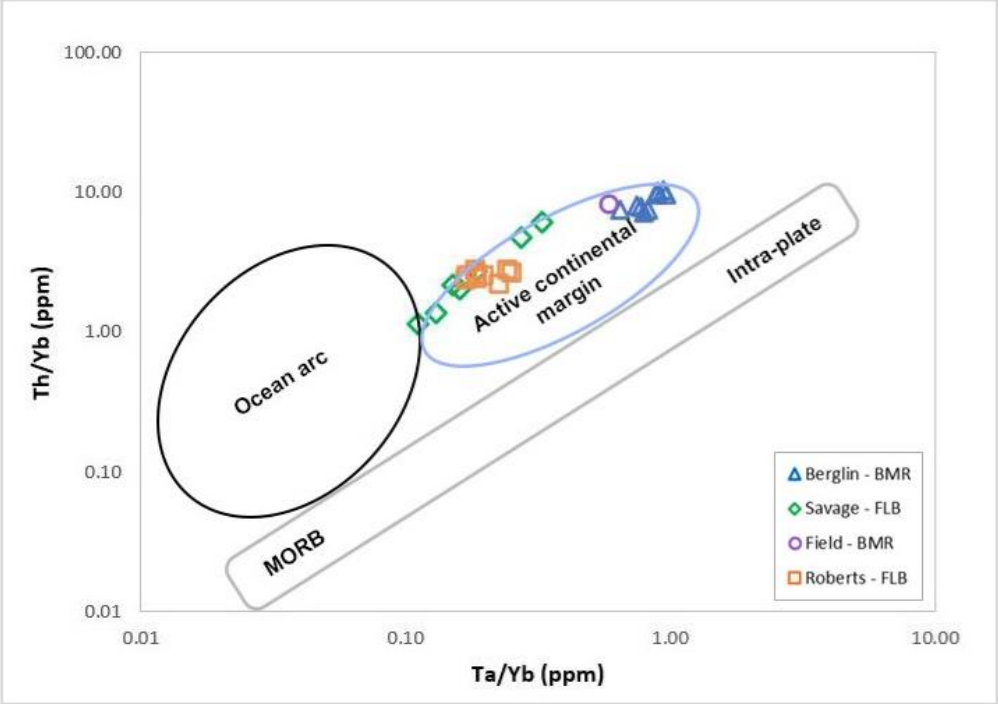

Figure 21. Discrimination plot of arc type and magmatic setting for clasts from the breccia of Mammoth Rock (BMR) and breccia of Frog Lakes (FLB) (Pearce, 1983).

The discrimination plots of immobile trace elements Nb versus Y (Fig. 22) and Ta versus Yb (Fig. 23) are used to differentiate magmas associated with volcanic arcs, syn-collisional settings, within-plate settings, and ocean ridges (Pearce et al., 1984). In the Nb versus Y plot (Fig. 22), both the breccia of Mammoth Rock and breccia of Frog Lakes data plot within the volcanic arc and sync-collisional magmatic setting. The breccia of Mammoth Rock data and breccia of Frog Lakes data from Roberts (2014) cluster while the breccia of Frog Lakes data from Savage (2021) display a positive slope for Nb. In the Ta versus Yb plot (Fig. 23), both the breccia of Mammoth Rock and breccia of Frog Lakes data plot within field for a volcanic arc magmatic setting. The breccia of Mammoth Rock data and breccia of Frog Lakes breccia data from Roberts (2014) cluster while the breccia of Frog Lakes data from Savage (2021) display an almost vertical positive slope line for Ta.

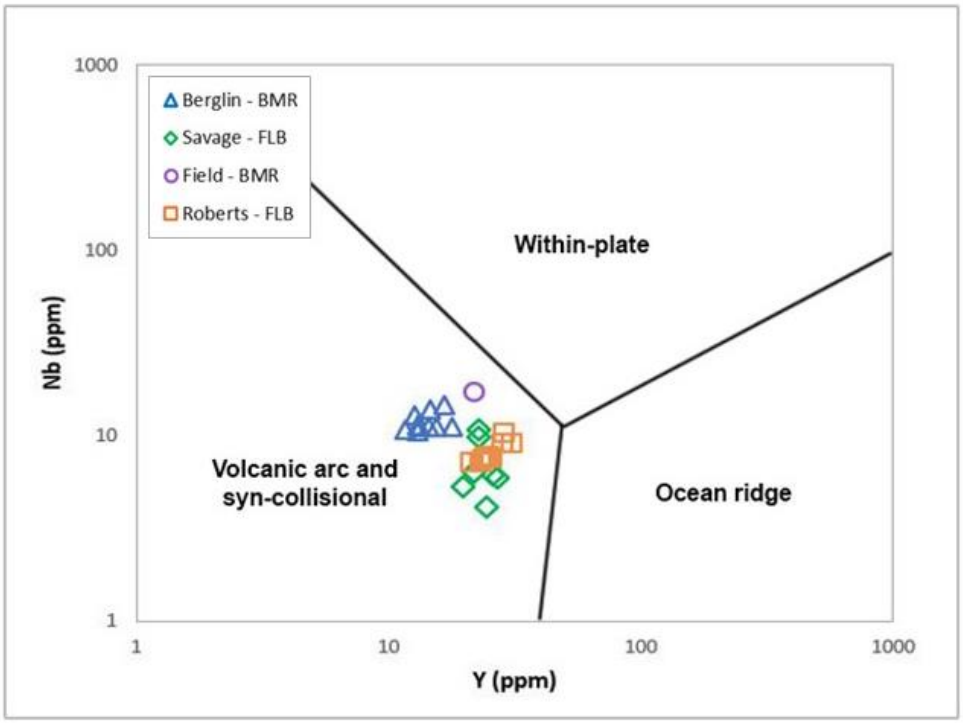

Figure 22. Discrimination plot of the magmatic setting for clasts from the breccia of Mammoth Rock (BMR) and breccia of Frog Lakes (FLB) (Pearce et al., 1984).

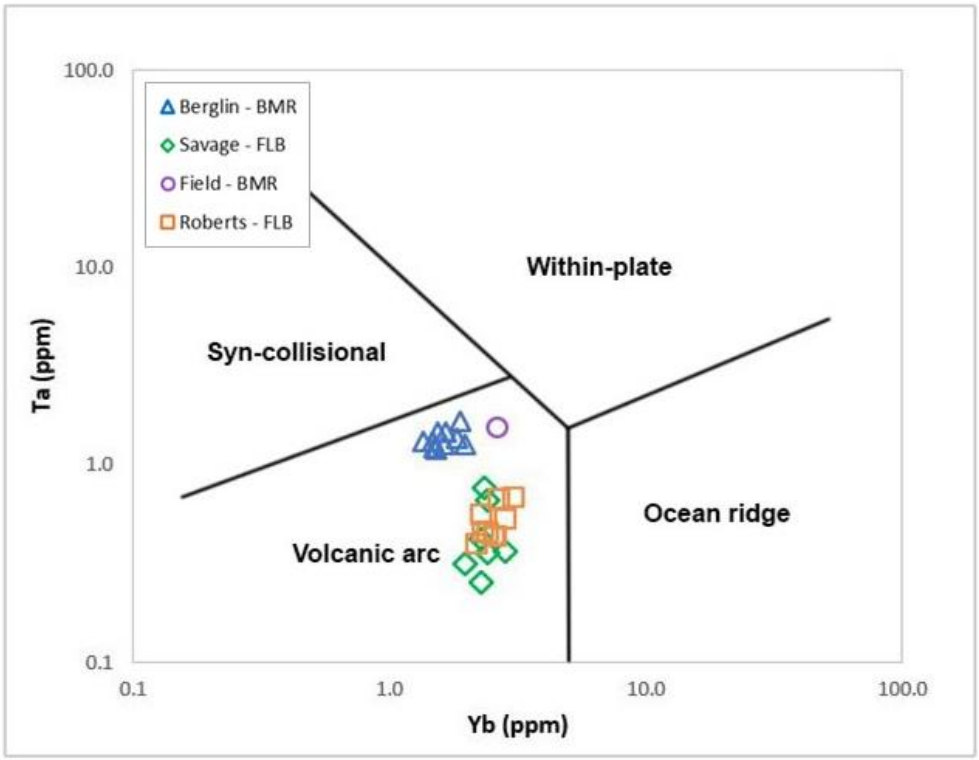

Figure 23. Discrimination plot of the magmatic setting for clasts from the breccia of Mammoth Rock (BMR) and Frog Lakes breccia (FLB) (Pearce et al., 1984).

The Ba/La versus Ba trace element plot is used to differentiate a crustal or mantle signature for the magmatic source (Fig. 24; Hildreth and Moorbath, 1988). Enrichment in the Ba content can be used to identify magma sources. A higher Ba/La ratio indicates a magma source with crustal signatures, while a lower Ba/La ratio indicates a magma source with mantle signatures. The breccia of Mammoth Rock and breccia of Frog Lakes data together show enrichment in the Ba content and a positive Ba/La slope (Fig. 24).

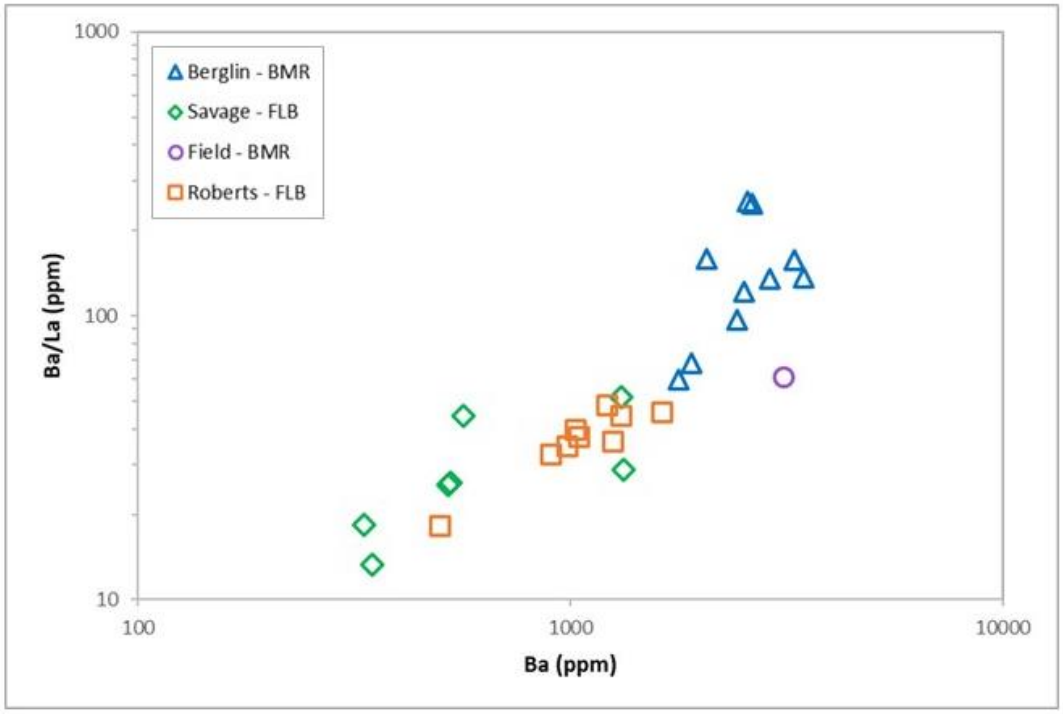

Figure 24. Trace element plot of Ba/La versus Ba for clasts from the breccia of Mammoth Rock (BMR) and breccia of Frog Lakes (FLB) (Hildreth and Moorbath, 1988).

Spider diagrams are used to show trace elements trends and anomalies in comparison to other widespread geochemical reservoirs such as primitive mantle, MORB, OIB, continental crustal values or other data. The trace element data can reveal sources that may have contributed to magmatism as well as correlate the breccia to similar magma systems in other locations. The breccia of Mammoth Rock was compared to N-MORB, E-MORB, OIB, average continental

upper-crustal, and average continental lower-crustal values (Figs. 25 and 26**;** Sun and McDonough, 1995; Lee et al., 2007). The trace-element geochemistry of the breccia closely resembles the average upper-crust abundances (Fig. 25). Negative anomalies for multiple trace elements for the breccia align with the upper-crust trend including Nb, Sr, Sm, and Eu. Some notable differences between the breccia and upper-crust trend are the Rb, Ba, and Th trace elements that have higher concentrations in the breccia compared to the average upper-crust concentrations. Tb and other REE have a higher concentration in the upper crust than in the breccia.

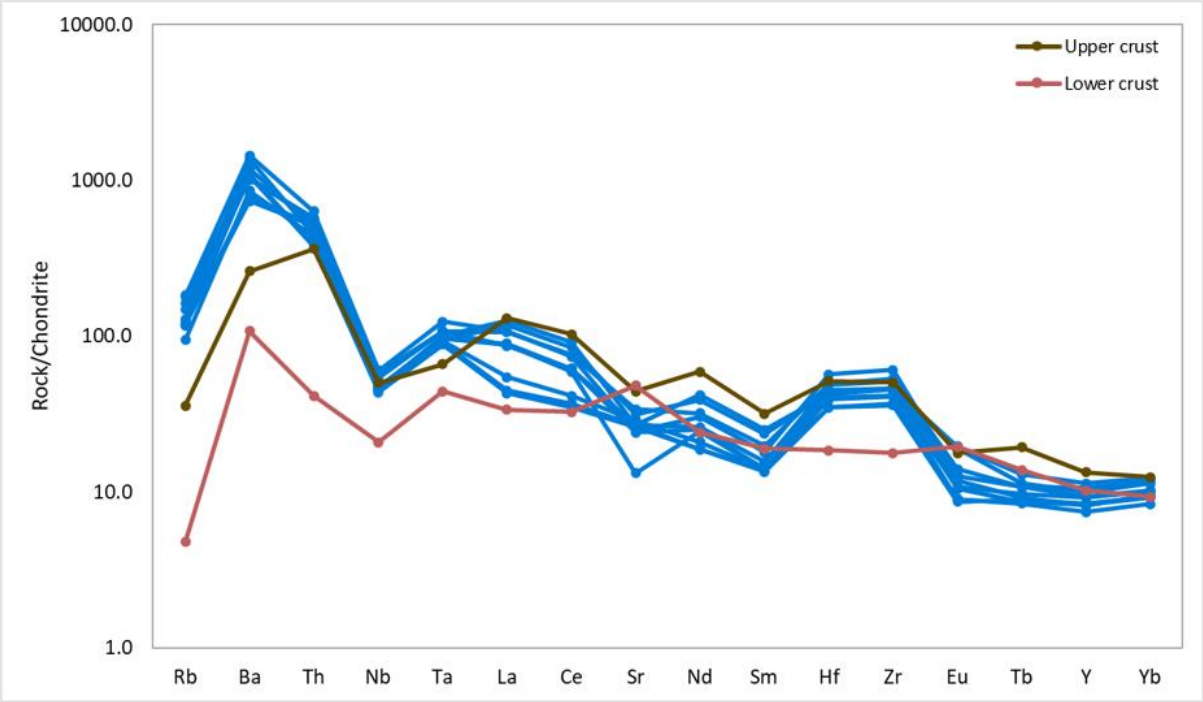

Figure 25. Spider diagram of mobile and immobile trace elements for clasts from the breccia of Mammoth Rock (BMR) normalized to chondrite (Sun and McDonough, 1995). Breccia compared to average upper and lower continental crustal values (Lee et al., 2007).

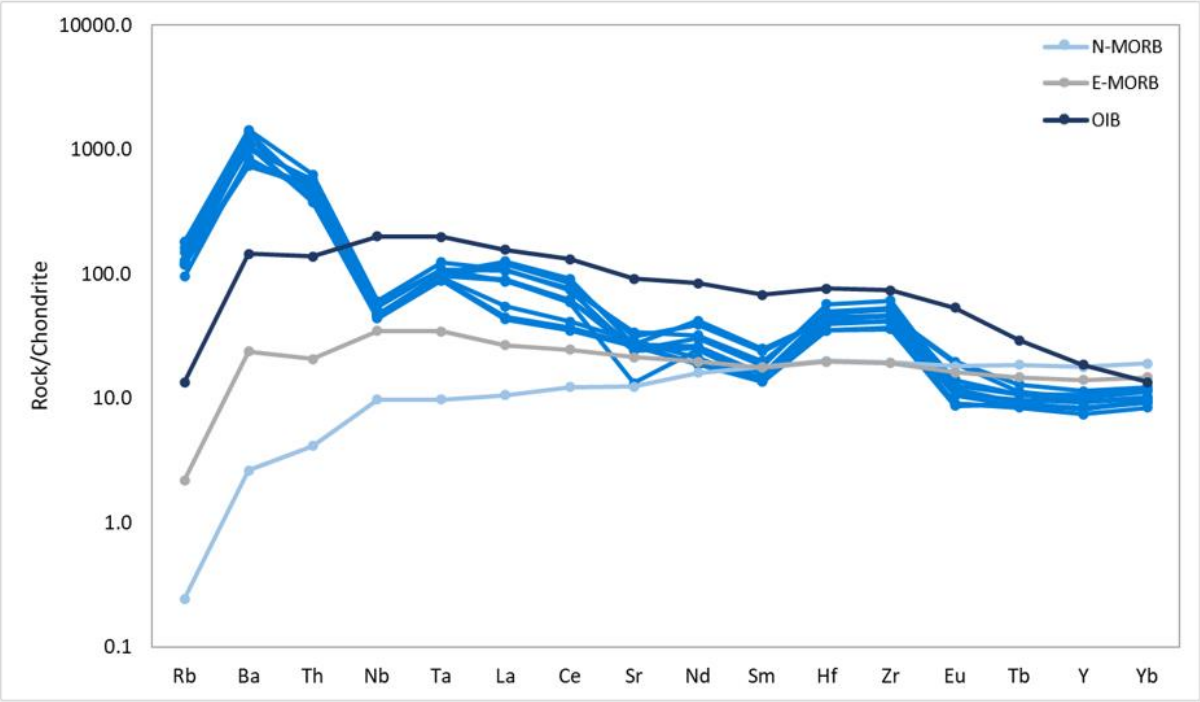

Figure 26. Spider diagram of mobile and immobile trace elements for clasts from the breccia of Mammoth Rock (BMR) normalized to chondrite (Sun and McDonough, 1995). Breccia compared to average N-MORB, E-MORB and OIB (Sun and McDonough, 1989).

The breccia of Mammoth Rock data was also compared to the Field (2018) data from the breccia of Mammoth Rock and the breccia of Frog Lakes data (Roberts, 2014; Savage, 2021). The breccia of Mammoth Rock and breccia of Frog Lakes data were both compared to N-MORB, E-MORB, OIB, average upper-crustal, and average lower-crustal values (Fig. 27 and 28; Sun and McDonough, 1995; Lee et al., 2007). The sample analyzed by Field (2018) and current breccia sample analysis both align with the upper-crustal trend (Fig. 28). The breccia of Frog Lakes has some notable differences from the breccia of Mammoth Rock. The breccia of Frog Lakes has negative anomalies for Ta, Zr, and Hf as well as positive anomalies for Sr and Eu not seen in the breccia of Mammoth Rock (Fig. 28). These align with the anomalies observed in the lower-crustal trend.

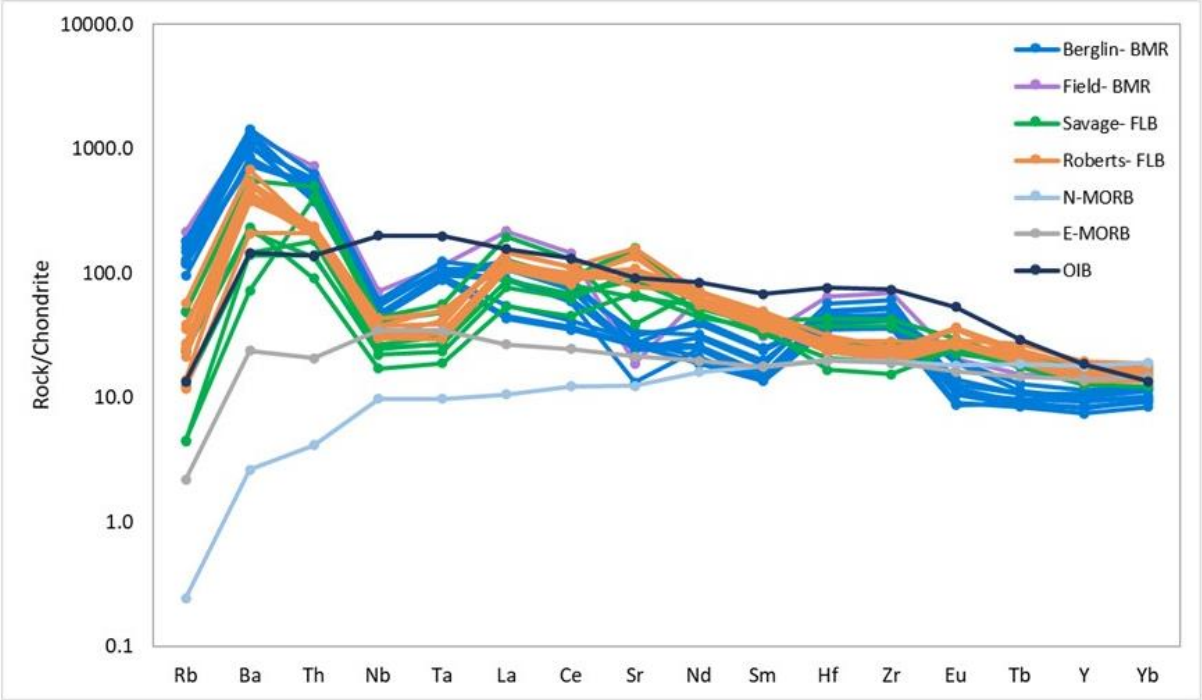

Figure 27. Spider diagram of mobile and immobile trace elements for the clasts from breccia of Mammoth Rock (BMR) and breccia of Frog Lakes (FLB) normalized to chondrite (Sun and McDonough, 1995). Breccia compared to average N-MORB, E-MORB and OIB (Sun and McDonough, 1989).

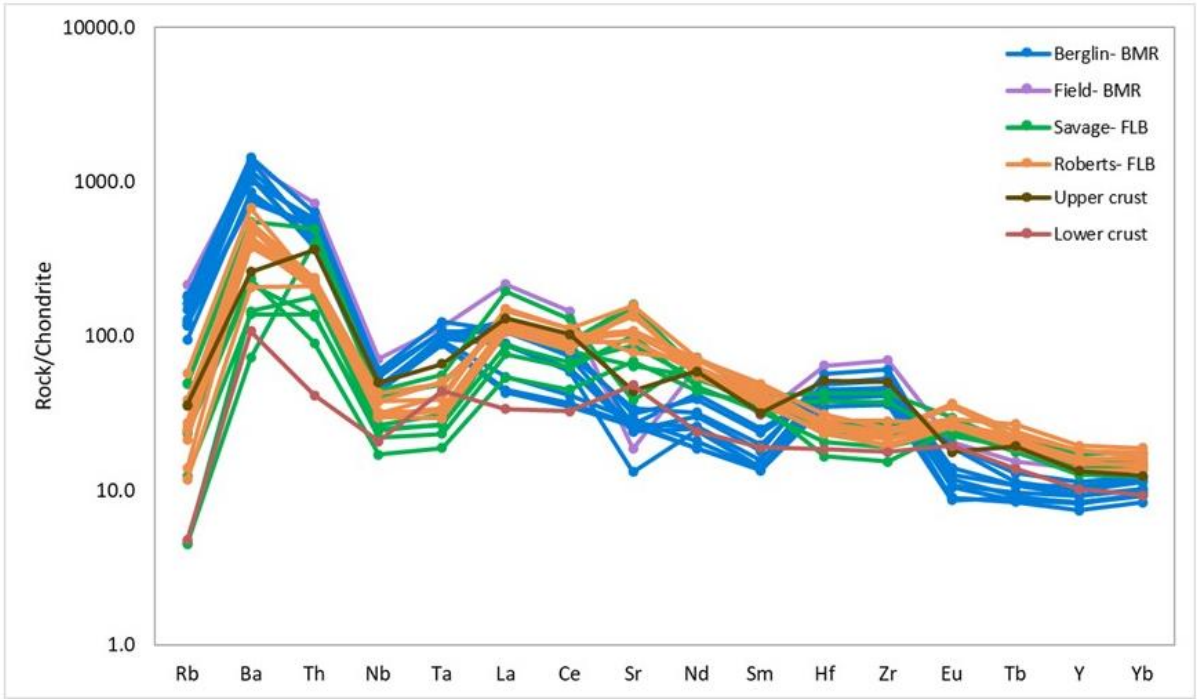

Figure 28. Spider diagram of mobile and immobile trace elements for clasts from the breccia of Mammoth Rock (BMR) and breccia of Frog Lakes (FLB) normalized to chondrite (Sun and McDonough, 1995). BMR and FLB compared to average upper and lower crustal values (Lee et al., 2007).

5.2.3 ZIRCON GEOCHEMISTRY

Analyses of the trace element geochemistry of arc zircons from volcaniclastic and siliciclastic rocks coupled with whole-rock geochemistry may provide evidence regarding tectonic setting and magmatic source rocks. Zirconium is a very incompatible and immobile trace element incorporated into the mineral zircon. Zircon is very resistant to recrystallization during hydrothermal alteration and low-grade metamorphism (Barth et al., 2018). The crustal thickness associated with arc-magma systems is interpreted through trace element zircon geochemistry discrimination plots such as U/Yb versus Hf. Arc magmas are characterized based on low, medium, or high U/Yb, which are correlated to crustal thickness. Continental-arc magma suites are characterized by zircon with U/Yb concentrations greater than ~0.1 to 0.2 and Th/Yb greater than ~0.1 (Barth et al., 2018). Only five clast samples from the breccia of Mammoth Rock produced zircon. The 48 zircon grains from the five breccia clasts, as well as 119 detrital zircon with a MSWD < 1.0 from the two sandstone samples, are used for interpretation. The breccia of Mammoth Rock data is characterized by medium and high U/Yb (Fig. 29) and the sandstone of Mammoth Rock is characterized dominantly by high U/Yb (Fig. 30).

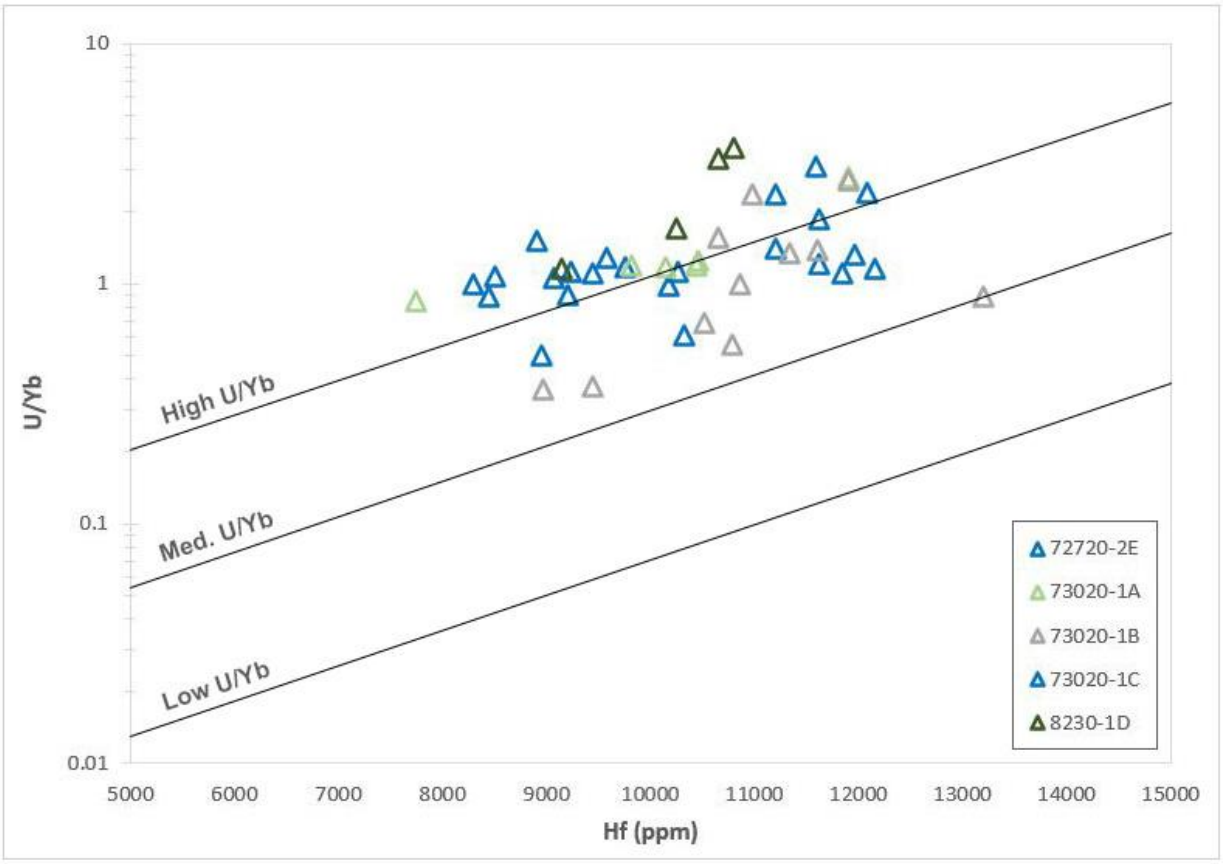

Figure 29. Trace element plot of U/Yb versus Hf from zircon trace-element geochemistry for the five clasts that produced zircon from the breccia of Mammoth Rock (BMR). All of the zircon for BMR are classified as medium to high U/Yb.

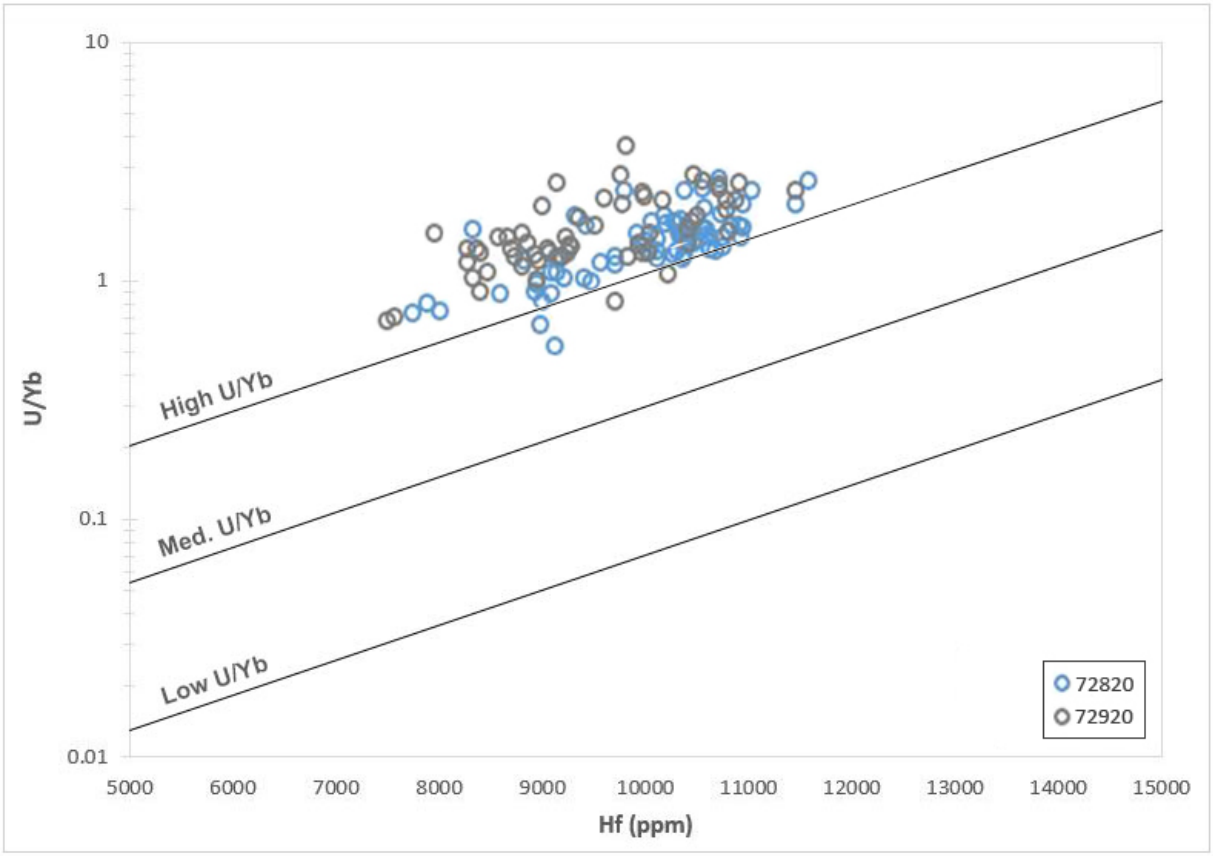

Figure 30. Trace element plot of U/Yb versus Hf from detrital zircon trace-element geochemistry for two bulk-rock samples from the sandstone of Mammoth Rock. The zircon are dominantly classified as high U/Yb.

5.3 GEOCHRONOLOGY

The breccia of Mammoth Rock and the sandstone interbeds are Late Triassic in age based on magmatic- and detrital-zircon data (Appendix D). Multiple breccia samples lacked zircon, which resulted in zircon analyses for five out of ten samples. Only two of the five clast samples provided a sufficient number of zircon for statistically relevant geochronologic analysis.

5.3.1 BRECCIA OF MAMMOTH ROCK

Two clast samples were used for geochronologic analysis: 1) 72720-2E, a black volcanic clast with plagioclase phenocrysts collected from polymictic facies 3 (Fig. 4) and 2) 73020-1A, a black volcanic clast with plagioclase phenocrysts collected from monomictic facies 1 (Fig. 4). The zircon grains yielded Late Triassic ages ranging from 230 Ma to 208 Ma. The older zircon grains from the polymictic facies 3 clast yielded a crystallization age of 225 ± 2 Ma and MSWD of 0.70 (Fig. 31). The younger zircon grains the monomictic facies 1 clast yielded a crystallization age of 216 ± 2 Ma and MSWD of 1.27 (Fig. 32)

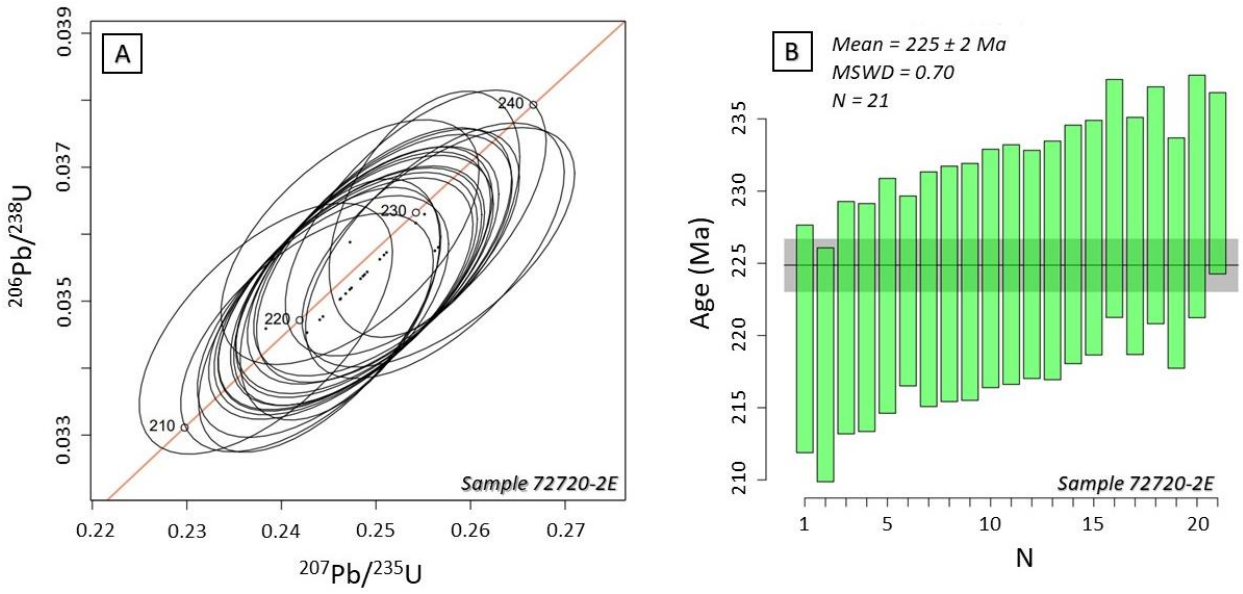

Figure 31. A) Concordia diagram of zircon from breccia-clast sample 72720-2E. **B)** Weighted mean plot of zircon from breccia-clast sample 72720-2E. MSWD = mean square of weighted deviates. N = number of crystals analyzed.

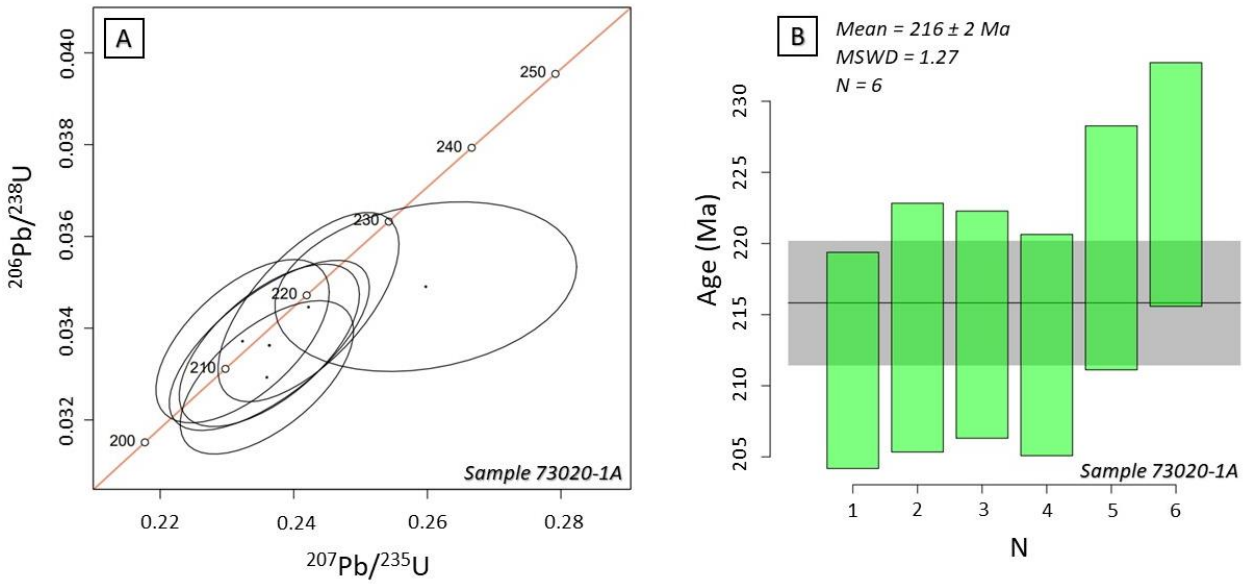

Figure 32. A) Concordia diagram of zircon from breccia-clast sample 73020-1A. **B)** Weighted mean plot of zircon from breccia-clast sample 73020-1A. MSWD = mean square of weighted deviates. N = number of crystals analyzed.

5.3.2 SANDSTONE OF MAMMOTH ROCK

Two bulk sandstone samples were collected for detrital zircon: 1) 72920, collected in the a lower sandstone bed (Fig. 4) in facies 6 (planar-laminated with breccia lenses) 72720-2E and 2) 72820, collected from an upper sandstone bed (Fig. 4) in facies 5 (planar-laminated). The lower sandstone bed sample (72920) yielded 60 detrital zircon grains that range in age from 209 Ma to 225 Ma with a weighted mean age of 222 ± 2 Ma and a MSWD of 0.98 (Fig. 33). The upper sandstone bed sample (72820) yielded 59 detrital zircon grains that range in age from 203 Ma to 221 Ma with a weighted mean age of 216 ± 2 Ma and MSWD of 0.87 (Fig. 34).

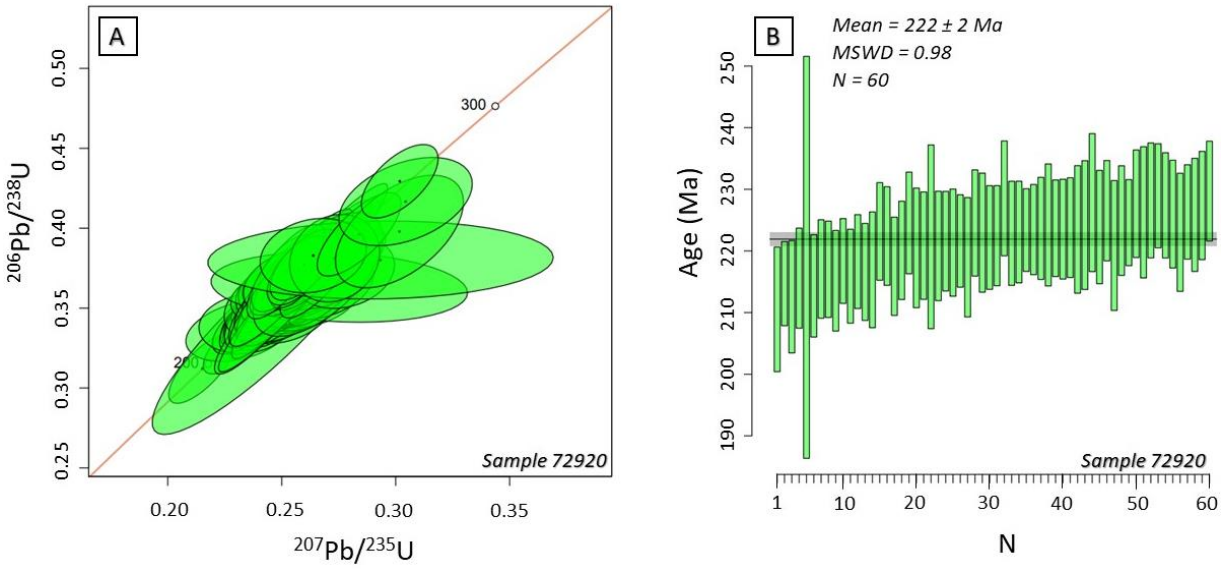

Figure 33. A) Concordia diagram of detrital zircon from the lower sandstone sample 72920. **B)** Weighted mean plot of detrital zircon from sandstone sample 72920. MSWD = mean square of weighted deviates. N = number of crystals analyzed.

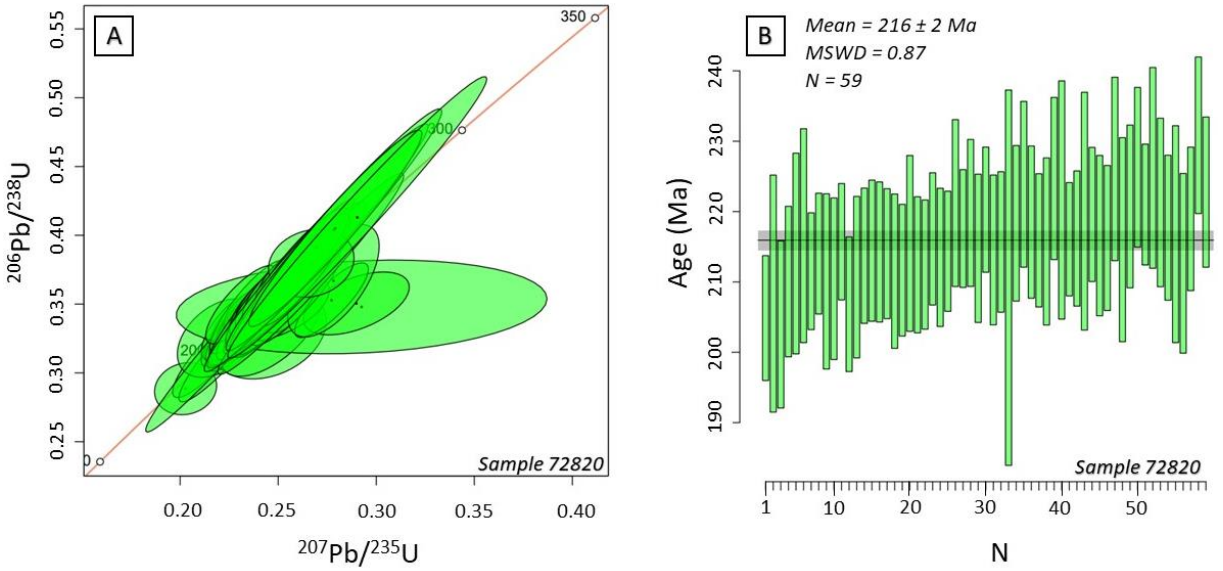

Figure 34. A) Concordia diagram of detrital zircon from the upper sandstone sample 72820. **B)** Weighted mean plot of detrital zircon from sandstone sample 72820. MSWD = mean square of weighted deviates. N = number of crystals analyzed.

6. DISCUSSION AND INTERPRETATIONS

6.1 FACIES INTERPRETATIONS

Volcanic facies analysis provides clues about the depositional environment and emplacement of breccia through characteristics such as clast shapes and volcanic successions. The sandstone interbeds provide further details about the depositional environment based on sedimentary structures within the beds. Both subaqueous and subaerial emplacement must be considered since volcanic breccias form in both environments.

The breccia clasts at Mammoth Rock have angular to subrounded, cuspate, jigsaw-fit, and fluidal clast shapes with flow-banded clast textures. The sandstone facies at Mammoth Rock include a mix of massive sandstone beds, planar laminated sandstone beds, planar laminated beds with breccia lenses, and low-angle cross bedded sandstone beds.

Breccia facies

Subaerial and subaqueous eruptions can produce both effusive and explosive volcanism, but effusive eruptions are more common for subaqueous eruptions (White et al., 2015). In subaerial settings, breccia is commonly produced in domes and calderas as carapace breccia, talus breccias, autobreccia, mesobreccia, megabreccia, and lithic breccias in outflow sheets (Branney and Acocella, 2015; Calder et al., 2015). Subaerial breccia typically has angular to subrounded, imbricated, spiny to jagged, cuspate and/or jigsaw-fit clast shapes. In subaqueous settings, hyaloclastite and peperite form in various environments including subaqueous domes, emergent islands, island arcs, mid-ocean ridges, seamounts, and glacial environments. Subaqueous breccia typically has angular to subrounded, equant, cuspate, jigsaw-fit, fluidal, clast-rotated, and/or resedimented clast shapes depending on whether the deposits are proximal

or distal (White et al., 2015). Pillow breccias and lobe-hyaloclastite may also be produced in subaqueous environments.

The cuspate and jigsaw-fit clasts suggest the breccia is hyaloclastite and deposition occurred subaqueously through autoclastic brecciation. The two sub-classes of autoclastic breccia are autobreccia and hyaloclastite. Autobreccia forms through dynamic stressing and shearing on molten lava, which causes the material to break itself apart (White et al., 2015). Hyaloclastite forms subaqueously by quenched-glass fragmentation and rapid cooling (Fisher and Schmincke, 1984; Hanson et al., 1991; Batiza and White, 2000). Autobreccia can occur in both subaerial and subaqueous settings, however hyaloclastite is limited to subaqueous settings. Clast characteristics of subaerial autobreccia including subrounded, rough, spiny, and jagged clasts are not observed in the breccia of Mammoth Rock. Even though cuspate and jigsaw-fit clasts can be found in both subaqueous and subaerial settings, the presence of subaqueous fluidal clasts with angular to subrounded equant-shaped clasts in the breccia facies are characteristics that suggest a subaqueous setting.

Fluidal clasts form both subaerially and subaqueously through fire-fountaining eruptions and differ in appearance based on the setting they form in (Simpson and McPhie, 2001). Subaerial fluidal clasts are typically highly vesicular, ragged, spindle shaped, and are welded or agglutinated. Subaqueous fluidal clasts are typically elongate or spindle shaped, with highly irregular and distorted shapes, and narrow or tapered tails. Blocky, angular hyaloclastite can also be produced through subaqueous fire-fountaining and deposited with fluidal breccia facies (Simpson and McPhie, 2001). Only breccia facies 2 displays fluidal clasts. Facies 1, 3, and 4 contain some blocky clasts with cuspate and jigsaw-fit clasts that have irregular edges, but the clasts are not highly distorted, elongate, or spindle shaped, and therefore not classified as fluidal.

The fluidal clasts of the breccia facies 2 are irregularly shaped, elongate, non-vesicular, and are neither ragged or agglutinated, suggesting emplacement in a subaqueous environment.

Sandstone facies

Sandstone is deposited in various terrestrial, transitional marine, and marine environments. These environments can produce similar characteristics, such as cross-bedding and laminae, making identification of the depositional environment very difficult without additional sedimentary structures and trace fossils. The characteristics of the sandstone facies of Mammoth Rock are very limited and non-unique and therefore can only describe a broad depositional environment.

The sandstone interbeds of Mammoth Rock are separated into planar laminated, lenticular, low-angle tabular cross-bedded, and massive facies. The beds do not exhibit any grading and particle size ranges from fine to coarse sand. Facies 6 and 8 contain subangular to subrounded breccia clasts randomly distributed throughout, but Facies 5 and 7 had few to no observable clasts. The lack of silt, clay, gravel, or carbonates may help to confine the environment associated with the sandstone facies.

Alternating fine- to coarse-grained sand with no grading and poor sorting suggests the deposition occurred in a mix of low- to high-energy environments. Subangular to subrounded breccia clasts within the sandstone facies suggests reworking and transportation likely occurred in a high-energy-environment. Shallow-marine settings, such as shoreface and tidal zones, consist dominantly of sand, vary from low to high energy, are mainly fine to medium grained but may be coarser grained, and exhibit variable bedding including planar to trough cross-bedding, low-angle to high-angle cross bedding planar laminated beds, or lenticular beds (Boggs Jr.,

2014). Siliciclastic rocks are also commonly associated with shallow-marine environments such as shallow continental shelves or epeiric seas. Deep-water marine environments are unlikely as they are typically composed of pelagic clays and muds (Boggs Jr., 2014). Terrestrial environments are also unlikely since glacial, fluvial, lacustrine, and delta systems commonly have variable sediment grain sizes including clay, silt, sand, and/or gravel, and typically display graded and sorted sediment deposits (Earle, 2015).

Overview of depositional environment

The jigsaw-fit, cuspate, and fluidal clasts of the breccia combined with the fine to coarse size of the sand grains, with the laminar, lenticular, and cross-bedded sedimentary structures of the sandstone suggest a deposition in a low- to high-energy shallow-marine environment, likely between shoreface and shallow continental shelf.

Emplacement mechanisms of facies and eruption style

The emplacement mechanisms (Table 2) suggested for the breccia of Mammoth Rock are two modes of submarine mass wasting (facies 1, 3 and 4) and submarine fall or bombs (facies 2). Sector collapse of submarine lava flows and domes can result in the emplacement of subaqueous debris avalanches (Soriano et al., 2012), which can also transition into debris flows when a large infiltration of water results in saturation and dissolution of the debris avalanche (Smith and Lowe, 1991). The angular to subangular clast shapes with local jigsaw-fit and dispersed cuspate clasts in breccia facies 1 and angular to subrounded clast shapes with dispersed cuspate clasts in breccia facies 3 and 4 suggest the breccia was initially produced by effusive volcanism involving a submarine lava flow; however, they were later emplaced through submarine mass wasting likely after the flow had cooled and solidified (Trofimovs et al., 2004)

Facies 1

Monomictic facies 1 was likely emplaced by a debris avalanche that formed as a result of collapse of a submarine lava flow. Local jigsaw-fit clasts are mildly fractured and only one blocky megaclast was observed. Jigsaw-fit clasts in facies 1 are generally located in close proximity to one another and likely fractured at the termination of the debris avalanche. Although none of the features commonly observed with jigsaw-fit clasts in subaerial debris avalanches are present, a submarine debris avalanche is the most likely mechanism of emplacement of monomictic facies 1 due to the angular to subangular clast shapes, localization of jigsaw-fit clasts, and the surrounding polymictic facies 3 and 4.

Clasts in facies 1 are dominantly angular to subangular, suggesting minimal abrasion and transport. A debris avalanche would cause disturbance of the in-situ hyaloclastite and result in resedimented hyaloclastite, which can still produce monomictic breccia and highly angular clasts if transport is minimal. No evidence of a proximal source vent is observed and monomictic facies 1 is surrounded by polymictic breccia facies 3 and 4, which show evidence of transport and reworking with clasts that are subrounded and mixed compositions. Therefore, a debris avalanche that remained intact as a large block resulting in dominantly angular to subangular clasts and localized jigsaw-fit clasts likely produced monomictic facies 1.

Facies 2

Monomictic facies 2 was likely deposited hot and emplaced in-situ as submarine fall or bombs. The fluidal clasts in the two outcrops of facies 2 are all uniform in orientation and monomictic suggesting the facies is not a product of mass wasting.

Facies 3 and 4

The emplacement mechanism for polymictic facies 3 and 4 is likely debris flows that resulted from the collapse of submarine lava flows. The collapse caused reworking of the breccia and the inclusion of sedimentary clasts as the debris flow traveled. The sedimentary clasts entrained in the debris flows were likely derived from sedimentary Paleozoic units, like the Mount Baldwin marble. Mass wasting of the hyaloclastite carapace can produce a matrix-supported debris flow (Soriano et al., 2012). The polymictic debris-flow deposits of Mammoth Rock are matrix supported with less than 35% clasts. The clasts in polymictic facies 4 are likely more rounded than in facies 3 due to further transport and longer entrainment in debris flows.

Facies	Clast characteristics	Eruption style	Emplacement mechanism
1	Monomictic Shapes: Angular to subrounded, cuspate, and jigsaw-fit Textures: Flow banded	Effusive	Submarine debris avalanche
2	Monomictic Shapes: Fluidal and subangular to subrounded	Fire-fountaining	Submarine fall or bombs
3	Polymictic Shapes: Angular to subrounded and cuspate Textures: Flow banded	Effusive	Submarine debris flow
4	Sparsely polymictic Shapes: Subangular to subrounded and cuspate Textures: Flow banded	Effusive	Submarine debris flow

Table 2. Clast characteristics, eruption style, and emplacement mechanism for breccia facies of Mammoth Rock.

6.2 PETROGRAPHIC INTERPRETATIONS

Breccia clasts in thin section reveal alteration and a few rare magmatic textures that are not seen in hand sample. The main magmatic textures observed were resorption along with rare zoning, exsolution lamellae, and undulose extinction. These textures suggest disequilibrium within the magmatic system due to a variety of potential factors including new injections of magma resulting in magma mixing (Hattori and Sato, 1996; Chang and Meinert, 2004; Shcherbakov et al., 2011), decompression (Humphreys et al., 2006), and metamorphism (Young, 1976; Song and Cao, 2021). The presence of numerous glomerocrysts in the breccia consisting dominantly of subhedral to anhedral crystals of quartz and plagioclase with less abundant biotite, muscovite, hornblende, clinopyroxene, oxides, sericite alteration, and/or chlorite alteration also supports the influence of magma mixing, decompression, and resorption (Hogan, 1993). In hand sample, the breccia clasts do not display phenocrysts indicative of metamorphism; however, in thin section the mineral assemblage of plagioclase, quartz, potassium feldspar, biotite, muscovite, epidote, chlorite, and sericite in the breccia clasts suggest metamorphism (Figs. 12,13, 14, and 15).

The breccia of Mammoth Rock underwent albite-epidote hornfels to hornblende-hornfels-grade metamorphism (Rinehart and Ross, 1964). The minerals observed in thin section for the breccia of Mammoth Rock align with the expected mineral assemblage for albite-epidote hornfels metamorphism with the exception of almandine. Groundmass alteration by epidote, chlorite, and sericite aligns with the expected mineral assemblage for albite-epidote hornfels metamorphism. Sericite is most commonly formed through metasomatism or hydrothermal alteration of feldspars (Rogers and Tolman, 1916). The Sierra Nevada arc was subject to many plutonic intrusions throughout the Mesozoic era that produced the Sierra Nevada batholith, the

largest episode occurring during the Cretaceous Period (Schweickert and Cowan, 1975). Hydrothermal fluids during emplacement of numerous plutons may be responsible for the formation of sericite, the present mineral assemblage, and the potassium-rich signature of the breccia.

6.3 GEOCHEMISTRY INTERPRETATIONS

Whole-rock major element geochemistry

Whole-rock major element geochemical data reveal abnormally high $K_2O + Na_2O$ weight % (Fig. 16) compared to other Triassic rocks like the breccia of Frog Lakes and the other Mesozoic rocks of the Mount Morrison pendant. The high $K_2O + Na_2O$ weight % is caused by the moderate to high K_2O concentration in the breccia that is likely a result of hydrothermal alteration. The major element data are not reliable due to the mobility of K during hydrothermal alteration, therefore they cannot be used to determine the composition. Nb and Y are used to determine the composition since they are immobile trace elements. Whole-rock trace element data reveal the clast compositions are predominantly trachyandesite based on SiO_2 and Nb/Y (Fig. 19) with outliers classified as trachyte to comendite.

Volatile gain, loss of Na, and infiltration of a K-rich fluid can cause an increase in potassium and other LILE (Ague, 2017). The high K_2O weight % of the breccia is likely a result of hydrothermal alteration during metamorphism. Regionally, in the eastern Sierra Nevada, more than 100 million years of potassium metasomatism is recorded in Triassic and Jurassic rocks of the Ritter Range that were affected by seawater and marine hydrothermal systems (Hanson et al., 1993). Potassium metasomatism is also recorded in the Triassic to Jurassic metavolcanic rocks of

the Inyo-White mountains and Alabama Hills that were affected by interaction with meteoric water prior to contact metamorphism (Sorensen et al., 1998). Potassium metasomatism due to subaqueous emplacement was considered for the breccia of Mammoth Rock, however other subaqueously emplaced outcrop, like the breccia of Frog Lakes, has low K_2O weight % and no evidence of potassium metasomatism. Sporadic gold- and silver-ore mining occurred from 1878 - 1941 in the Mammoth Mine, which lies on the northwest slope of Mammoth Rock topographically below the volcanic breccia deposits (Rinehart and Ross, 1964). Later mineralization as a result of hydrothermal alteration may have further contributed to the high K_2O weight % and produced the gold and silver deposits. Another potential K-rich source is the upper crust. Potassium is one of the common elements that can infiltrate the magma by crustal contamination. Volcanoes of the central Chilean arc segment of the Andean volcanic arc show increasing K_2O northward with respect to the southern region of the arc due to larger contributions from the crust and subcrustal lithosphere (Hildreth and Moorbath, 1988). K_2O increases in andesite from ~1 up to 2.5% were observed where the continental crust was thicker and more mature. Some of the high K_2O weight % may be a result of a thick upper crust and contamination, but other contemporary volcanic deposits of similar age in the eastern Sierra Nevada, such as the breccia of Frog Lakes in the Saddlebag Lake pendant, do not have high K_2O weight %. All other outcrops located in the Mount Morrison pendant that are Triassic to Cretaceous in age do not display the high K_2O weight % that is observed in the breccia of Mammoth Rock. Therefore, K-rich hydrothermal alteration and mineralization are suggested to be the primary source of potassium infiltration. The upper crust is suggested to be a secondary minor source of potassium infiltration based on trace element concentrations that correlate with

upper crust geochemistry (Fig. 25), as well as the thick crust below the arc suggested by zircon trace element geochemistry (Fig. 29).

Fractional-crystallization trends for the breccia of Mammoth Rock provide an understanding of the evolution of the magma system. The fractional-crystallization trends were created in Excel using regression with the R^2 equation and includes the data from all ten breccia clasts. The major element oxides for the breccia of Mammoth Rock do not show trends for oxides of low-charge cations, but there are weak negative trends for oxides of high-charge cations like TiO_2 and Al_2O_3 (Fig. 35). Typically, magmatic rocks from the same eruptive center display strong negative trends, but only TiO_2 and Al_2O_3 for the breccia of Mammoth Rock show weak negative trends. The lack of oxides and strong trends suggests the breccia were either produced by multiple volcanic sources or by other processes such as hydrothermal alteration, partial melting, magma mixing, or crustal contamination. Low-charge cations are mobile in fluids and the low-charge cations in clasts from the breccia of Mammoth Rock display no trends and are very scattered, which suggests the scatter was caused by hydrothermal alteration.

Al_2O_3 weight % concentration in addition to the Mg# (molar Mg) of arc magmas can be used to differentiate primitive versus evolved magmas and their correlated tectonomagmatic environment (Kelemen et al., 2014). Primitive arc andesites have 10 - 19 Al_2O_3 weight % and an Mg# > 60, while evolved arc andesites have > 20% Al_2O_3 weight % and an Mg# < 60. Primitive andesites are often a product of metasomatized lithospheric mantle or partial melting of the subarc mantle wedge in a subduction zone (Kelemen et al., 2014; Han et al., 2018). In contrast, evolved andesites with moderate Mg# may be a result of crystal fractionation of primitive melts or partial melting of the lower arc crust (Kelemen et al., 2014). Calc-alkaline evolved arc magmas can form through fractionation of a primitive andesite and result in higher SiO_2 and

alkali contents. The values for clasts from the breccia of Mammoth Rock range from 15.79 to 25.70 Al_2O_3 weight % (Table 1) and 40.6 to 41.2 for Mg#, suggesting that the magma associated with it was an evolved andesite that resulted from fractionation of a primitive andesite. Partial melting of the lower crust is unlikely based on the trace element trends normalized to chondrite that suggest an upper arc crustal signature (Fig. 25). Fractional crystallization trends for the breccia of Mammoth Rock shown by the high-charge cation oxide elements, such as plagioclase fractionation for Al_2O_3 (Fig. 35), support the inference of an evolved andesitic magma fractionating from a primitive melt. Fractional crystallization modeling was conducted on the breccia on Mammoth Rock using mineral composition data from a study by Escobar-Burciaga (2016) analyzing andesitic magmas from the Northern Cascades. Andesitic mineral compositions for plagioclase, clinopyroxene, orthopyroxene, hornblende, and magnetite were modeled at a rate of 10% fractionation for the breccia of Mammoth Rock. Modeling suggests fractionation of plagioclase for Al_2O_3 and of magnetite/oxides for TiO_2, which align with the trendlines established through regression analysis (Fig. 35). Fractionation of plagioclase is further supported by the Sr negative anomaly (Fig. 25), which is often a result of crustal contribution to the magma system and suggests that the magma source for the breccia of Mammoth Rock was a crustal source. Regression analysis trendlines were plotted on all diagrams, but the diagrams of low-charge cation oxide elements display very scattered data that do not align with the regression analysis trendline. Mineral compositions were modeled and plotted with vectors on all diagrams to further support fractionation for high-charge cations and conclude there is no fractionation for low-charge cations. Some mineral composition vectors for low-charge cations may align with the regression analysis trendline, but the scattered data do not align with the trendline or vectors.

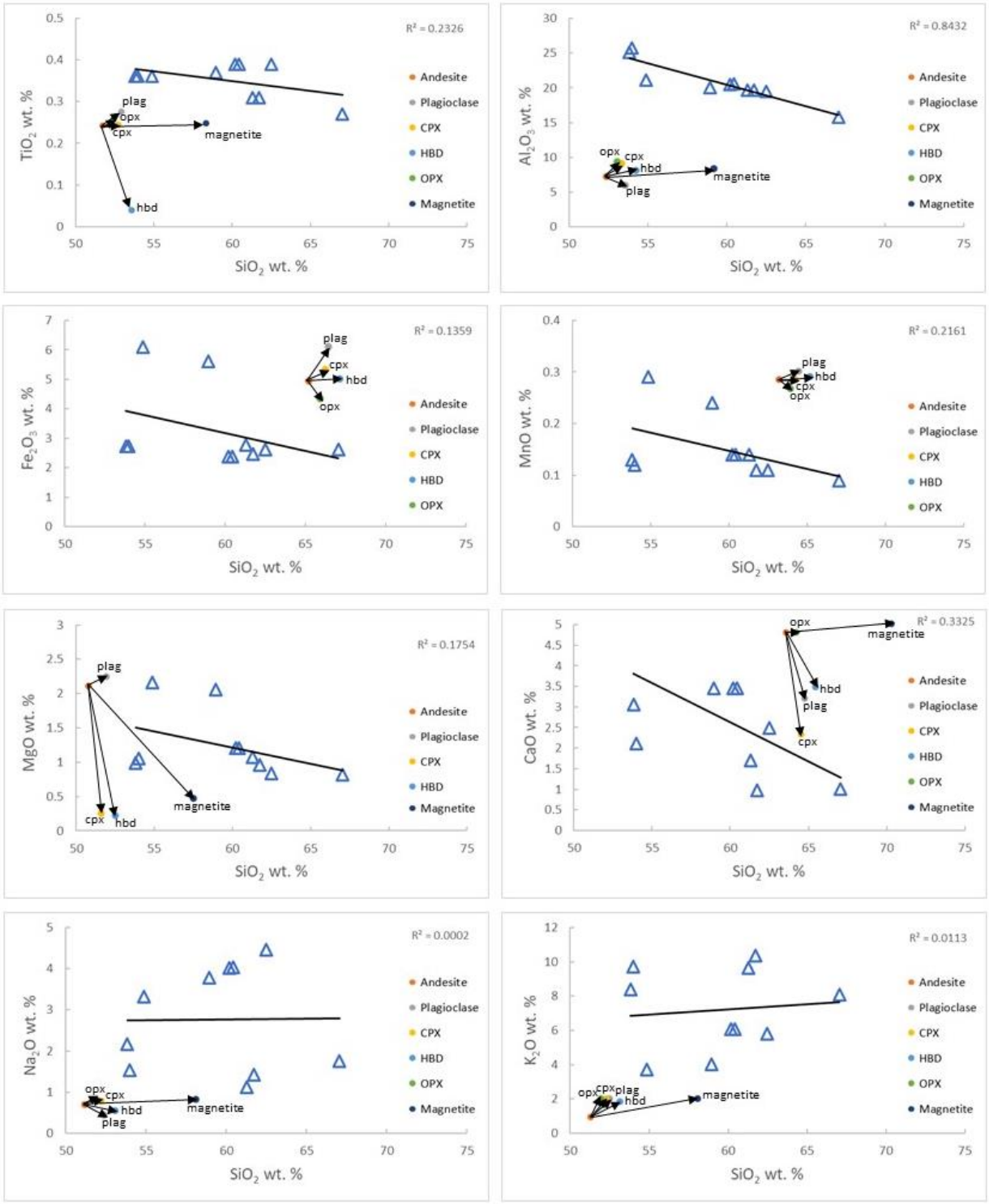

Figure 35. Interpreted fractional crystallization trends based on regression analysis for the breccia of Mammoth Rock (BMR) on Harker variation diagrams. Major element oxides for the BMR display weak negative trends for oxides of high-charge cations including TiO_2 and Al_2O_3. No trends are observed for oxides of low-charge cations. Trend arrows are vectors showing amount of change caused by 10% fractionation of the stated minerals. Compositions of the minerals are from Escobar-Burciaga (2016).

Whole-rock trace element geochemistry

Immobile trace elements have proven the most reliable for the arc discrimination and compositional classification of the breccia of Mammoth Rock. Primarily upper-crustal signatures are indicated by trace element geochemistry trends (Fig. 25). The volcaniclastic rocks were produced in a volcanic arc (Figs. 22 and 23) that formed on a continental margin (Figs. 20 and 21). Breccia of Frog Lakes data show similar results to the breccia of Mammoth Rock data (Figs. 20, 21, 22, and 23).

Arc magmas typically display enrichment of LILE and LREE with depletion in HREE (Kelemen et al., 2014). Trace element geochemical data for the breccia of Mammoth Rock compared to average upper crust, average lower crust, N-MORB, E-MORB, and OIB revealed trends that closely align with average upper-crustal values (Figs. 25 and 26). The breccia of Mammoth Rock displays a higher enrichment of LREE compared to HREE and increasing incompatibility and mobility of the LILE compared to the REE. Multiple negative and positive anomalies are observed in the trace elements trend for the breccia (Fig. 25). Rb displays an increasing value and Ba displays a positive anomaly. Rb and Ba are both water-soluble elements that increase in subduction fluids, are easily extracted from the mantle since they are incompatible, and are then concentrated in the continental crust, which suggests crustal contamination and subduction-related metasomatism. The positive slope of the Ba/La data (Fig. 24) also supports the positive anomalies in the spider diagrams for Rb and Ba. High Ba/La ratios indicate enrichment of the mantle wedge as result of Ba-rich subduction-zone fluids (Wilson, 1994) and mobility of Ba as a result of alteration or metamorphism. High concentrations of Ba/La are observed in arcs compared to MORB and intra-plate basalts. The positive trend of the Ba/La ratio also suggests a magma source with crustal signatures. Low concentrations for Nb

(and also Ta) are typical indicators of subduction-related melts. Low Nb-Ta abundances also favor contribution of continental crust (Hildreth and Moorbath, 1988). Th concentrations in the breccia are high. U, Th, and Pb are often concentrated in early melts. Concentrations of Th and U are much higher in continental arcs than intra-oceanic arcs (Hildreth and Moorbath 1988). Two distinct troughs are associated with Nb and Sr that often indicate the retention of an element during melting and may also suggest crustal contamination. Depletion of Nb particularly indicates a strong crustal influence whereas enrichment of Nb results from mantle contributions in settings like ocean island basalts (Hildreth and Moorbath, 1988). Sr behaves more incompatibly in the mantle, but more compatibly in the crust. The low concentration of Sr may indicate the compatibility within the crust due to lower pressure and the presence/substitution into plagioclase, which is a common crustal mineral. Upper-crustal assimilation and fractional crystallization (AFC) processes cause Sr concentrations to drop, which may be the cause for the Sr trough (Hildreth and Moorbath 1988). Eu displays a slight negative anomaly and is also correlated to plagioclase fractionation. Whole-rock major element geochemical data also supports the fractional crystallization of plagioclase. Trace element data suggest that the source of magmatism for the breccia of Mammoth Rock is dominantly upper crustal with minor to moderate influence from subduction metasomatism.

The breccia of Frog Lakes trace element data trends align with both average upper- and lower-crustal trends (Fig. 28). Similar to the breccia of Mammoth Rock, the breccia of Frog Lakes displays a higher enrichment of LREE compared to HREE elements and increasing incompatibility and mobility of the LILE for most breccia samples. However, the LREE and HREE of the breccia of Frog Lakes align more with the lower-crustal trend, while the LILE align partially with upper-crustal trends and partially with lower-crustal trends. The low Nb and Ta

suggest breccia of Frog Lakes was a subduction-related melt and also was potentially affected by large contributions from the crust; however, it may not have been upper crustal contributions. The LREE and HREE are typically immobile making them more reliable than the LILE in determining the crustal signature. Almost all samples from breccia of Frog Lakes (Roberts, 2014; Savage, 2021) have a positive Sr and Eu anomaly that suggests there was a lack of upper crustal contamination and likely accumulation of plagioclase. Both the breccia of Mammoth Rock and breccia of Frog Lakes trace elements suggest crustal contributions, but by potentially different parts of the crust. Sr and Eu suggest that the breccia of Frog Lakes was likely impacted by the lower crust despite some alignment of the LILE with the upper-crustal trend.

Trace element zircon geochemistry

Zircon trace elements such as U, Yb, and Hf are used to differentiate arc magmas and their tectonic setting. Continental arc magmas are characterized by zircons with a U/Yb greater than ~0.1 (Barth et al., 2018) and as high as 4 (Grimes et al., 2015). Moderately enriched continental arc magmas display U/Yb ~0.1 to 1 while strongly enriched continental arc magmas display U/Yb ≥ 1 (Barth et al., 2018). Higher continental arc U/Yb values suggest influence from a mature crust enriched in LILE (Grimes et al., 2015). The breccia of Mammoth Rock is classified as medium to high U/Yb (Fig. 29) and the sandstone of Mammoth Rock is classified as dominantly high U/Yb (Fig. 30) suggesting that the arc was a formed on thick continental crust in an oceanic-continental subduction zone. Crustal thickening, uplift of buoyant crust, and thrust faulting occur as a result of convergence (Saleeby and Dunne, 2015) and characterize induced subduction (Stern, 2004). Geochemical evidence and characteristics that reflect induced subduction are important to the understanding of the paleogeography of the arc and are further discussed in section 6.5.

6.4 GEOCHRONOLOGY INTERPRETATIONS

Initiation and termination of magmatism for BMR

Timing of magmatism and deposition of the breccia of Mammoth Rock is constrained by U-Pb zircon geochronology data. Magmatism occurred between 225 ± 2 Ma and 216 ± 2 Ma based on crystallization ages from zircon in two clasts (Figs. 31 and 32; Appendix D). The earliest mass wasting volcanic products at Mammoth Rock were deposited at ca. 222 Ma based on maximum depositional ages from detrital zircon (Figs. 33; Appendix D) extracted from sandstone interbeds that are dispersed throughout the breccia facies. Magmatism related to the breccia of Mammoth Rock terminated by ca. 216 with the deposition of the monomictic facies based on maximum depositional ages from the youngest detrital zircon grains (Figs. 34; Appendix D) from the sandstone facies. The ca. 216 Ma emplacement age of the dacite of Arrowhead Lake stratigraphically above the breccia (Field, 2018) supports the termination of volcanism related to the breccia of Mammoth Rock by ca. 216 Ma.

Effusive volcanism began with deposition of submarine lava flows around ca. 225 Ma. Emplacement of submarine debris flows began around ca. 222 Ma. Collapse of the hyaloclastic flow margin likely produced submarine debris flows that entrained the metasedimentary clasts as it traveled, producing polymictic facies 3 and 4. Continuation of effusive volcanism may have produced and deposited more submarine lava flows. Later collapse of a large block from one of the submarine lava flows likely resulted in a debris avalanche, which produced monomictic facies 1 with in-situ jigsaw-fit clasts and dominantly angular to subangular clasts. Volcanism and mass wasting of the breccia of Mammoth Rock terminated by ca. 216 Ma with a fire-fountaining eruption that deposited monomictic facies 2.

Timing of magmatism and fractional crystallization of BMR and FLB

The whole-rock major and trace element geochemical data for the breccia of Mammoth Rock and breccia of Frog Lakes create a positive trendline between subalkaline basalt and trachyandesite on the SiO_2 versus Nb/Y diagram (Fig. 19) and a positive data trendline for progression of arc formation from oceanic to continental on arc discrimination diagrams (Figs. 20 and 21). Based on major and trace-element geochemical data, the clasts from the breccia of Mammoth Rock are genetically related. When comparing the geochemical signatures and positive trends of the breccia of Mammoth Rock and breccia of Frog Lakes, a potential correlation is observed between the magmas that fed these eruptions.

Fractional crystallization of plagioclase, pyroxene, hornblende, biotite, Fe-oxides, and Fe-Ti oxides resulting in an evolved andesitic magma is suggested for the source of breccia of Mammoth Rock based on geochemical evidence; however, it is possible that fractionation of one primitive basaltic magma body produced the breccia of Frog Lakes and the breccia of Mammoth Rock. Savage (2021) suggested fractional crystallization of multiple minerals including plagioclase, olivine, clinopyroxene, orthopyroxene, and Fe-oxides in the magma that produced the breccia of Frog Lakes. Compositions for the breccia of Frog Lakes are sub-alkaline basalt to andesite and compositions are dominantly trachyandesite for the breccia of Mammoth Rock (Fig. 19). In various discrimination diagrams, major- and trace-element data trends suggest the potential of a related magma source through fractional crystallization. The age of crystallization also supports a related magma source. The age of crystallization of the breccia of Frog Lakes is confined between 224 ± 1 Ma to 219 ± 1 Ma by the tuff of Saddlebag Lake and tuff of Greenstone Lake (Barth et al., 2011) and the magmatism of the breccia of Mammoth Rock is confined between ca. 225 Ma to ca. 216 Ma by U-Pb geochronology. Despite the geochemical

and geochronologic correlations, the location of the breccia of Mammoth Rock is approximately 50 km away along strike from the breccia of Frog Lakes, suggesting a very large and widespread magma system would have to be present to feed both of these volcanic centers, which is unlikely. Both breccias have a geochemically similar magma source and were syn-depositional; however, the breccia of Frog Lakes and the breccia of Mammoth Rock were not likely erupted from the same magma due to the large distance between the breccias.

6.5 EARLY-ARC PALEOGEOGRAPHY AND SUBDUCTION INCEPTION

Geochemical data and facies analysis of Mammoth Rock imply the early eastern Sierra Nevada arc between ca. 225 Ma - 216 Ma was a shallow-marine environment. Evidence from the volcanic and siliciclastic facies of Mammoth Rock supports the inference of arc formation in a submarine environment by Saleeby and Dunne (2015). Changes in the paleogeography of the arc are further supported by the deposition of sedimentary formations, such as the Buckskin Formation and Chinle Formation. The lower member of the Triassic Buckskin Formation in southeastern California and western Arizona is composed of metasedimentary rocks that suggest a shallow- to marginal-marine environment of deposition between ca. 250 - 245 Ma in the southeastern Sierra Nevada backarc based on arc-derived detrital zircon grains (Riggs et al., 2020). A shift in the depositional environment for the Sierra Nevada arc was first observed during the middle Triassic in the southeastern region of the arc where the Triassic Chinle Formation records the transition to terrestrial depositional environments ca. 235 Ma (Riggs et al., 2020). The initiation of Sierra Nevada arc tectonics resulted in the ca. 235 Ma onset of rapid sedimentation, dynamic subsidence in the backarc due to sediment loading, and progradation (Howell and Blakey, 2013) of conglomerates with an abundance of arc-derived volcanic rock in

the lower members of the Chinle Formation that suggests deposition transitioned to fluvial and lacustrine environments (Riggs et al., 2020). The transition to terrestrial depositional environments beginning ca. 235 Ma and dynamic subsidence is only evidenced in the southeastern region of the arc. Therefore, prior to ca. 235 Ma, the depositional environment of the Sierra Nevada arc was presumably still marginal to shallow marine; after ca. 235 Ma, the east-central to northeastern regions of the arc likely remained a shallow-marine depositional environment during the emplacement of the breccia of Mammoth Rock while the southeastern region of the arc transitioned to fluvial and lacustrine depositional environments.

Induced subduction results in crustal thickening, uplift of the upper plate, thrusting, and arc magmatism (Stern, 2004). Regional transpressive fold-and-thrust deformation and uplift in the overriding upper plate are observed in the Sierra Nevada arc (Saleeby and Dunne, 2015) suggesting an induced mode of subduction inception. In the eastern Sierra Nevada, induced-subduction inception is evidenced by the geochemical signatures of the breccia of Mammoth Rock that reveal crustal thickness, as well as the initiation of magmatism that produced the volcaniclastic deposits of Mammoth Rock. The LILE enrichment (Fig. 25) and medium to high U/Yb (Figs. 29 and 30) of zircon imply thickening of the continental crust under the arc, supporting the induced subduction inception. Major elements of the host magma typically align with the U/Yb ranges in the zircon geochemical data (Barth et al., 2018) as is seen in the K_2O weight % geochemical data for the breccia of Mammoth Rock (Table 1). Association of high K_2O weight % and a thick continental crust has been observed beneath volcanic arcs like the Andes (Hildreth and Moorbath, 1988). Similarly, the K_2O weight % the breccia of Mammoth Rock is high and U/Yb in the zircon grains agree with the likelihood of a thick continental crust. However, the breccia of Mammoth Rock was also affected by metamorphism and potentially by

hydrothermal alteration. Therefore, the high K_2O weight % is dominantly suggested to be a result of hydrothermal alteration and the thick upper crust is likely a secondary source that moderately contributed to the high K_2O weight %. The breccia of Mammoth Rock is the oldest magmatic deposit in the Mount Morrison pendant with a crystallization age of ca. 225 Ma. However, the earliest magmatism in the eastern Sierra Nevada is evidenced by the 232 ± 1.4 Ma intrusion of the Spiller Canyon Pluton (Cao et al., 2015) and the 232 ± 2 Ma Black Mountain tuff (Barth et al., 2011). Arc magmatism in the eastern Sierra Nevada began ~7 m.y. before the deposition of the breccia of Mammoth Rock indicating the breccia is not a primary magmatic product of early subduction inception, but a subsequent product of arc magmatism as the magmatic arc evolved.

6.6 MODERN ANALOGY FOR THE SIERRA NEVADA

The modern Puysegur subduction zone in New Zealand closely resembles the ancient Permian subduction initiation associated with Sierra Nevada volcanic arc (Stern, 2004; Saleeby and Dunne, 2015; Lodes et al., 2020). Dextral slip occurred along the Eocene passive margin initiating the Alpine Fault at 23 Ma (Lamarche and Lebrun, 2000; Lebrun et al., 2003; Sutherland et al., 2006). The Puysegur subduction zone initiated at 20 Ma (Lebrun et al., 2003) along the dextral Alpine Fault (Lamarche and Lebrun, 2000; Sutherland et al., 2006) resulting in oblique convergence of the Australian plate and Pacific plate (Sutherland et al., 2006; Patel et al., 2017). Subduction inception resulted in uplift, shortening, crustal thickening, thrust faulting, and subsidence (Sutherland et al., 2006), which are characteristics of induced subduction inception (Stern, 2004). Middle Miocene uplift in the Balleny Basin to the south (Sutherland et al., 2006) was followed by uplift 5 Ma later in the Fiordlands (Lebrun et al., 2003) to the north as a result of lateral propagation (Zhou et al., 2020) and the northward migration of the subduction

inception (House et al., 2002). Adakitic to andesitic volcanic rocks were deposited on Solander Island (Leng et al., 2012; Stern and Gerya, 2018) in the last 2 m.y. (Lemarche and Lebrun, 2000; House et al., 2002; Levy et al., 2021) representing the first products of arc magmatism related to the Puysegur subduction zone (Patel et al., 2017).

The mode of induced subduction inception for the Sierra Nevada arc closely resembles the inception of the Puysegur subduction zone. Both subduction zones initiated through the mode of induced subduction due to convergence along a strike-slip boundary at a continental margin and as a result produced similar tectonic characteristics of uplift, shortening, crustal thickening, and thrust faulting.

7. CONCLUSIONS

The formation of the Cordilleran arc was a result of the initiation of convergence and subduction along the California-Coahuila transform fault that truncated the southwestern Laurentian passive margin. The upper plate experienced crustal thickening, uplift, thrusting, and arc magmatism as a result of induced-subduction inception. The Triassic breccia of Mammoth Rock is the oldest volcanic deposit in the Mount Morrison pendant in eastern Sierra Nevada. The volcaniclastic facies and geochemical signatures of the breccia of Mammoth Rock provide a clearer context of the early-arc paleogeography and support the mode of induced-subduction inception.

The characteristics of the volcaniclastic and siliciclastic facies of Mammoth Rock suggest deposition of submarine lava flows ca. 225 Ma - 216 Ma in a low- to high-energy shallow-marine environment likely between shoreface and a shallow-continental shelf. The breccia was

initially emplaced through effusion of submarine lava flows ca. 225 Ma, but the final emplacement of the breccia at Mammoth Rock was the result of mass wasting initiating at ca. 222 Ma. Collapse of solidified submarine lava flows likely resulted in submarine debris flows that entrained metasedimentary clasts and produced polymictic facies 3 and 4. Effusive volcanism presumably continued and produced more submarine lava flows. Later, a debris avalanche likely resulted from another collapse of a solidified submarine lava flow that produced monomictic facies 1 with local in-situ jigsaw-fit clasts and dominantly angular to subangular clasts. Volcanism related to the breccia of Mammoth Rock terminated by ca. 216 Ma with a submarine fire-fountaining eruption that produced fall and bombs resulting in the emplacement of monomictic facies 2. Termination of volcanism related to the breccia of Mammoth Rock by ca. 216 is supported by the ca. 216 Ma emplacement of the dacite of Arrowhead Lake stratigraphically above monomictic facies 2.

Breccia clasts are fine grained, contain dominantly plagioclase phenocrysts, and are trachyandesite in composition. Thin sections show dominantly plagioclase with minor amounts of potassium feldspar, hornblende, quartz, biotite, muscovite, clinopyroxene, oxides, and variable amounts of epidote, sericite, and chlorite groundmass alteration. Alteration of the breccia was likely a result of hydrothermal alteration and contact metamorphism potentially during the emplacement of the Sierra Nevada batholith.

Geochemistry of the breccia clasts shows a high K_2O and Al_2O_3 weight %, low Mg#, LILE and LREE enrichment, HREE depletion, and medium to high U/Yb zircon trace-element values. The high K_2O weight % is dominantly suggested to be a result of K-rich hydrothermal alteration due to mineralization and Mesozoic metamorphism. The thick continental upper crust had a minor influence on the high K_2O weight %. The low Mg# and high Al_2O_3 weight %

indicate the magma source was an evolved andesite that may have fractionated from a primitive melt. The lack of trends for low-charge cations on Harker diagrams and mobility of low-charge cations in fluids further suggests the breccia was affected by hydrothermal alteration. Fractional crystallization of plagioclase and Fe-oxides such as magnetite are suggested by modeling and regression analysis trends on Harker variation diagrams for the breccia. The LILE, LREE, and HREE concentrations for the breccia align with typical enrichments and depletions of arc magmas. Trace element anomalies suggest crustal contamination likely from the upper crust, possible metasomatism during subduction, and fractional crystallization of plagioclase. The LREE enrichment and U/Yb values suggest a thick continental crust, which supports the mode of induced-subduction inception.

The Sierra Nevada subduction zone initiated through the mode of induced subduction due to convergence along a strike-slip boundary at a continental margin resulting in uplift, shortening, crustal thickening, and thrust faulting. The Puysegur subduction zone initiated similarly through induced-subduction inception, producing similar tectonic characteristics and closely resembling the Sierra Nevada subduction zone.

REFERENCES

Ague, J.J., 2017, Element mobility during regional metamorphism in crustal and subduction zone environments with a focus on the rare earth elements (REE), American Mineralogist: Journal of Earth and Planetary Materials, v. 102, n. 9, p. 1796-1821.

Barth, A.P., Walker, J.D., Wooden, J.L., Riggs, N.R. and Schweickert, R.A., 2011, Birth of the Sierra Nevada magmatic arc: Early Mesozoic plutonism and volcanism in the east-central Sierra Nevada of California, Geosphere, v. 7, no. 4, p. 877-897.

Barth, A.P., Feilen, A.D.G., Yager, S.L., Douglas, S.R., Wooden, J.L., Riggs, N.R., and Walker, J.D., 2012. Petrogenetic connections between ash-flow tuffs and a granodioritic to granitic intrusive suite in the Sierra Nevada arc, California, Geosphere, v. 8, no. 2, p. 250-264.

Barth, A.P., Tani, K., Meffre, S., Wooden, J.L., Coble, M.A., Arculus, R.J., Ishizuka, O. and Shukle, J.T., 2017, Generation of silicic melts in the early Izu-Bonin Arc recorded by detrital zircons in proximal arc volcaniclastic rocks from the Philippine Sea, Geochemistry, Geophysics, Geosystems, v. 18, n. 10, p. 3576-3591.

Barth, A.P., Wooden, J.L., Riggs, N.R., Walker, J.D., Tani, K., Penniston-Dorland, S.C., Jacobson, C.E., Laughlin, J.A. and Hiramatsu, R., 2018, Marine volcaniclastic record of early arc evolution in the eastern Ritter Range pendant, central Sierra Nevada, California, Geochemistry, Geophysics, Geosystems, v. 19, no. 8, p. 2543-2559.

Batiza, R., and White, J.D.L., 2000, Submarine Lavas and Hyaloclastite *in* Sigurdsson, H., Houghton, B., McNutt, S., Rymer, H., and Stix, J., eds., The encyclopedia of volcanoes, p. 361-380.

Branney, M. and Acocella, V., 2015, Calderas in Sigurdsson, H., Houghton, B., McNutt, S., Rymer, H., and Stix, J., eds., The encyclopedia of volcanoes, v. 2, p. 299-315.

Boggs Jr, S., 2014, Principles of sedimentology and stratigraphy, Pearson Education, v. 5., 564 p.

Calder, E.S., Lavallée, Y., Kendrick, J.E. and Bernstein, M., 2015, Lava dome eruptions in Sigurdsson, H., Houghton, B., McNutt, S., Rymer, H., and Stix, J., eds., The encyclopedia of volcanoes, v. 2, p. 343-362.

Cao, W., Paterson, S., Memeti, V., Mundil, R., Anderson, J.L. and Schmidt, K., 2015, Tracking paleodeformation fields in the Mesozoic central Sierra Nevada arc: Implications for intra-arc cyclic deformation and arc tempos, Lithosphere, v. 7, no. 3, p. 296-320.

Cas, R. and Simmons, J., 2018, Why deep-water eruptions are so different from subaerial eruptions, Frontiers in Earth Science, v. 6, p. 198.

Chang, Z. and Meinert, L.D., 2004. The magmatic–hydrothermal transition—evidence from quartz phenocryst textures and endoskarn abundance in Cu–Zn skarns at the Empire Mine, Idaho, USA. Chemical Geology, v. 210, no. 1-4, p. 149-171.

Dickinson, W.R., 1977, Paleozoic plate tectonics and the evolution of the Cordilleran continental margin.

Dickinson, W.R., 2004, Evolution of the North American cordillera, Annu. Rev. Earth Planet, Sci., v. 32, p. 13-45.

Earle, S., 2015. Physical geology.

Escobar-Burciaga, R.D., 2016, Mineral Complexities as Evidence for Open-system Processes in Formation of Intermediate Magmas of the Mount Baker Volcanic Field, Northern Cascade Arc [Master's thesis]: Western Washington University, 173 p.

Field, D.M., 2018, Episodic Sierran arc magmatism expressed in Mesozoic rocks of the Mount Morrison Pendant, east-central Sierra Nevada, California [Master's thesis]: Northern Arizona University, 130 p.

Fisher, R.V. and Schmincke, H.U., 1984, Submarine volcaniclastic rocks in Pyroclastic Rocks, p. 265-296.

Ginibre, C., Wörner, G. and Kronz, A., 2007, Crystal zoning as an archive for magma evolution. Elements, v. 3, no. 4, p. 261-266.

Grimes, C.B., Wooden, J.L., Cheadle, M.J. and John, B.E., 2015, "Fingerprinting" tectono-magmatic provenance using trace elements in igneous zircon, Contributions to Mineralogy and Petrology, v. 170, n. 5, p. 1-26.

Harris, A.J. and Rowland, S.K., 2015, Lava flows and rheology in Sigurdsson, H., Houghton, B., McNutt, S., Rymer, H., and Stix, J., eds., The encyclopedia of volcanoes, v. 2, p. 321-342.

Han, Q., Peng, S., Polat, A., Kusky, T., Deng, H. and Wu, T., 2018, A ca. 2.1 Ga Andean-type margin built on metasomatized lithosphere in the northern Yangtze craton, China: Evidence from high-Mg basalts and andesites, Precambrian Research, v. 309, p. 309-324.

Hanson, R.B., Sorensen, S.S., Barton, M.D. and Fiske, R.S., 1993, Long-term evolution of fluid–rock interactions in magmatic arcs: evidence from the Ritter Range pendant, Sierra Nevada, California, and numerical modeling, Journal of Petrology, v. 34, n. 1, p. 23-62.

Hanson, R.E., 1991, Quenching and hydroclastic disruption of andesitic to rhyolitic intrusions in a submarine island-arc sequence, northern Sierra Nevada, California, Geological Society of America Bulletin, v. 103, n. 6, p. 804-816.

Hattori, K. and Sato, H., 1996, Magma evolution recorded in plagioclase zoning in 1991 Pinatubo eruption products, American Mineralogist, v. 81, no. 7-8, p. 982-994.

Kelemen, P.B., Hanghøj, K. and Greene, A.R., 2003, One view of the geochemistry of subduction-related magmatic arcs, with an emphasis on primitive andesite and lower crust, Treatise on geochemistry, v. 3, p. 659.

Hildreth, W. and Moorbath, S., 1988, Crustal contributions to arc magmatism in the Andes of central Chile, Contributions to mineralogy and petrology, v. 98, n. 4, p. 455-489.

Hogan, J.P., 1993, Monomineralic glomerocrysts: textural evidence for mineral resorption during crystallization of igneous rocks, The Journal of geology, v. 101, no. 4, p. 531-540.

House, M.A., Gurnis, M., Kamp, P.J. and Sutherland, R., 2002, Uplift in the Fiordland region, New Zealand: Implications for incipient subduction, Science, v. 297, no. 5589, p. 2038-2041.

Howell, E.R. and Blakey, R.C., 2013, Sedimentological constraints on the evolution of the Cordilleran arc: New insights from the Sonsela Member, Upper Triassic Chinle Formation, Petrified Forest National Park (Arizona, USA), Bulletin, v. 125, n. 7-8, p. 1349-1368.

Humphreys, M.C., Blundy, J.D. and Sparks, R.S.J., 2006, Magma evolution and open-system processes at Shiveluch Volcano: Insights from phenocryst zoning, Journal of Petrology, v. 47, no. 12, p. 2303-2334.

Lamarche, G. and Lebrun, J.F., 2000, Transition from strike-slip faulting to oblique subduction: active tectonics at the Puysegur Margin, South New Zealand, Tectonophysics, v. 316, n. 1-2, p. 67-89.

Le Bas, M.J., Le Maitre, R.W., Streckeisen, A., and Zanettin, B., 1986, A chemical classification of volcanic rocks based on the total alkali-silica diagram: Journal of Petrology, v. 27, p. 745-750.

Lebrun, J.F., Lamarche, G. and Collot, J.Y., 2003, Subduction initiation at a strike-slip plate boundary: The Cenozoic Pacific-Australian plate boundary, south of New Zealand, Journal of Geophysical Research: Solid Earth, v. 108, n. B9.

Lee, C.T.A., Morton, D.M., Kistler, R.W. and Baird, A.K., 2007, Petrology and tectonics of Phanerozoic continent formation: From island arcs to accretion and continental arc magmatism, Earth and Planetary Science Letters, v. 263, n. 3-4, p. 370-387.

Leng, W., Gurnis, M., and Asimow, P., 2012, From basalts to boninites: The geodynamics of volcanic expression during induced subduction initiation, Lithosphere, v. 4, no. 6, p. 511-523.

Levy, D.A., Zuza, A.V., Haproff, P.J. and Odlum, M.L., 2021, Early Permian tectonic evolution of the Last Chance thrust system: an example of induced subduction initiation along a plate boundary transform, Bulletin, v. 133, n. 5-6, p. 1105-1127.

Lin, M., Peng, S., Jiang, X., Polat, A., Kusky, T., Wang, Q. and Deng, H., 2016, Geochemistry, petrogenesis and tectonic setting of Neoproterozoic mafic–ultramafic rocks from the western Jiangnan orogen, South China, Gondwana Research, v. 35, p. 338-356.

Lodes, E., Riggs, N.R., Smith, M.E., Stone, P. and Abu-Alam, T.S., 2020, Cordilleran Subduction Initiation: Retroarc Timing and Basinal Response in the Inyo Mountains, Eastern California, Lithosphere, v. 2020, n. 1.

McDonough, W.F. and Sun, S.S., 1995, The composition of the Earth. Chemical geology, v. 120, n. 3-4, p. 223-253.

Patel, J., Sutherland, R., Gurnis, M., Van Avendonk, H., Gulick, S.P., Shuck, B., Stock, J. and Hightower, E., 2021, Stratigraphic architecture of Solander Basin records Southern Ocean currents and subduction initiation beneath southwest New Zealand, Basin Research, v. 33, n. 1, p. 403-426.

Pearce, J.A., 1982, Trace element characteristics of lavas from destructive plate boundaries, Andesites, v. 8, p. 525-548.

Pearce, J.A., 1983, Role of the sub-continental lithosphere in magma genesis at active continental margins.

Riggs, N.R., Sanchez, T.B. and Reynolds, S.J., 2020, Evolution of the early Mesozoic Cordilleran arc: The detrital zircon record of back-arc basin deposits, Triassic Buckskin Formation, western Arizona and southeastern California, USA, Geosphere, v. 16, n. 4, p. 1042-1057.

Rinehart, C.D., and Ross, D.C., 1964, Geology and mineral deposits of the Mount Morrison quadrangle, Sierra Nevada, California, with a section on a gravity study of Long Valley, Geological Survey Professional Paper, no. 385, v. 106.

Roberts, S.E., 2014, Breccia of Frog Lakes: reconstructing Triassic volcanism and subduction initiation in the east-central Sierra Nevada, California, [Master's thesis]: Indiana University, 64 p.

Rogers, A.F. and Tolman, C.F., 1916, Sericite a low temperature hydrothermal mineral, Economic Geology, v. 1, n. 2, p. 118-150.

Saleeby, J.B., and Dunne, G., 2015, Temporal and tectonic relations of early Mesozoic arc magmatism, southern Sierra Nevada, California. Late Jurassic margin of Laurasia—A record of faulting accommodating plate rotation: Geological Society of America Special Paper 513, p. 223-268.

Savage, J.A., 2021, Mafic magmatism, subaqueous volcanism, and dome growth in the early Triassic Sierran arc, east-central, Sierra Nevada, California [Master's thesis]: Northern Arizona University, 120 p.

Schweickert, R.A., and Cowan, D.S., 1975, Early Mesozoic tectonic evolution of the western Sierra Nevada, California. Geological Society of America Bulletin, v. 86, no. 10, p. 1329-1336.

Shcherbakov, V.D., Plechov, P.Y., Izbekov, P.E. and Shipman, J.S., 2011, Plagioclase zoning as an indicator of magma processes at Bezymianny Volcano, Kamchatka, Contributions to Mineralogy and Petrology, v. 162, no. 1, p. 83-99.

Simpson, K. and McPhie, J., 2001, Fluidal-clast breccia generated by submarine fire fountaining, Trooper Creek Formation, Queensland, Australia, Journal of volcanology and geothermal research, v. 109, n. 4, p. 339-355.

Smith, G.A. and Lowe, D.R., 1991, Lahars: Volcano hydrologic-events and deposition in the debris flow—hyperconcentrated flow continuum.

Snow, C.A., and Scherer, H., 2006, Terranes of the western Sierra Nevada Foothills metamorphic belt, California: A critical review, International Geology Review, v. 48, no. 1, p. 46-62.

Song, S. and Cao, Y., 2021, Textures and structures of metamorphic rocks, Encyclopedia of Geology, p. 375-388.

Sorensen, S.S., Dunne, G.C., Brooks Hanson, R., Barton, M.D., Becker, J., Tobisch, O.T. and Fiske, R.S., 1998, From Jurassic shores to Cretaceous plutons: Geochemical evidence for paleoalteration environments of metavolcanic rocks, eastern California. Geological Society of America Bulletin, v. 110, n. 3, p. 326-343.

Soriano, C., Riggs, N., Giordano, G., Porreca, M. and Conticelli, S., 2012, Cyclic growth and mass wasting of submarine Los Frailes lava flow and dome complex in Cabo de Gata, SE Spain, Journal of Volcanology and Geothermal Research, v. 231, p. 72-86.

Speed, R.C., 1979, Collided Paleozoic microplate in the western United States, The Journal of Geology, v. 87, n. 3, p. 279-292.

Stern, R.J., 2004, Subduction initiation: spontaneous and induced, Earth and Planetary Science letters, v. 226, p. 275-292.

Stern, R.J. and Gerya, T., 2018, Subduction initiation in nature and models: A review, Tectonophysics, v. 746, p. 173-198.

Stevens, C.H. and Greene, D.C., 1999, Stratigraphy, depositional history, and tectonic evolution of Paleozoic continental-margin rocks in roof pendants of the eastern Sierra Nevada, California, Geological Society of America Bulletin, v. 111, n. 6, p. 919-933.

Stevens, C.H. and Greene, D.C., 2000, Geology of Paleozoic rocks in eastern Sierra Nevada roof pendants, California, Field Guides, v. 2, p. 237-254.

Sun, S.S. and McDonough, W.F., 1989, Chemical and isotopic systematics of oceanic basalts: implications for mantle composition and processes, Geological Society, London, Special Publications, v. 42, n. 1, p. 313-345.

Sutherland, R., Barnes, P. and Uruski, C., 2006, Miocene-Recent deformation, surface elevation, and volcanic intrusion of the overriding plate during subduction initiation, offshore southern Fiordland, Puysegur margin, southwest New Zealand, New Zealand Journal of Geology and Geophysics, v. 49, n. 1, p. 131-149.

Tobisch, O.T. and Fiske, R.S., 1982, Repeated parallel deformation in part of the eastern Sierra Nevada, California and its implications for dating structural events, Journal of Structural Geology, v. 4, no. 2, p. 177-195.

Trofimovs, J., Cas, R.A.F. and Davis, B.K., 2004, An Archaean submarine volcanic debris avalanche deposit, Yilgarn Craton, western Australia, with komatiite, basalt and dacite megablocks: The product of dome collapse, Journal of Volcanology and Geothermal Research, v. 138, no. 1-2, p. 111-126.

Walker, J.D., 1988, Permian and Triassic rocks of the Mojave Desert and their implications for timing and mechanisms of continental truncation, Tectonics, v. 7, n. 3, p. 685-709.

White, J.D., McPhie, J. and Soule, S.A., 2015. Submarine lavas and hyaloclastite in Sigurdsson, H., Houghton, B., McNutt, S., Rymer, H., and Stix, J., eds., The encyclopedia of volcanoes, v. 2, p. 363-375.

White, J.D., Schipper, C.I. and Kano, K., 2015, Submarine explosive eruptions in Sigurdsson, H., Houghton, B., McNutt, S., Rymer, H., and Stix, J., eds., The encyclopedia of volcanoes, v. 2, p. 553-569.

Wilson, M., 1994, Igneous petrology, Chapman & Hall, 488 p.

Winchester, J.A. and Floyd, P.A., 1977, Geochemical discrimination of different magma series and their differentiation products using immobile elements. Chemical geology, v. 20, p. 325-343.

Young, S.W., 1976, Petrographic textures of detrital polycrystalline quartz as an aid to interpreting crystalline source rocks, Journal of Sedimentary Research, v. 46, no. 3, p. 595-603.

Zhou, X., Li, Z.H., Gerya, T.V. and Stern, R.J., 2020, Lateral propagation–induced subduction initiation at passive continental margins controlled by preexisting lithospheric weakness, Science advances, v. 6, n. 10, p. eaaz1048.

APPENDIX A

Sample Number	GPS location	Rock collected/analyzed for:
72720-2C*	37.612155° N, -118.991988° W	▪ Whole-rock geochemistry ▪ Petrographic thin sections
72720-2E-1*	37.612155° N, -118.991988° W	▪ Whole-rock geochemistry ▪ Petrographic thin sections ▪ Zircon geochronology ▪ Zircon geochemistry
72720-2E-2*	37.612155° N, -118.991988° W	▪ Whole-rock geochemistry ▪ Petrographic thin sections
72920-4A	37.614775° N, -118.992771° W	▪ Whole-rock geochemistry ▪ Petrographic thin sections
72920-5A	37.614774° N, -118.992672° W	▪ Whole-rock geochemistry ▪ Petrographic thin sections
72920-5B	37.614774° N, -118.992672° W	▪ Whole-rock geochemistry ▪ Petrographic thin sections
72920-5C	37.614774° N, -118.992672° W	▪ Whole-rock geochemistry ▪ Petrographic thin sections
73020-1A	37.614619° N, -118.992891° W	▪ Whole-rock geochemistry ▪ Petrographic thin sections ▪ Zircon geochronology ▪ Zircon geochemistry
73020-1B	37.614619° N, -118.992891° W	▪ Whole-rock geochemistry ▪ Petrographic thin sections ▪ Zircon geochronology ▪ Zircon geochemistry
73020-1C	37.614619° N, -118.992891° W	▪ Whole-rock geochemistry ▪ Petrographic thin sections ▪ Zircon geochronology ▪ Zircon geochemistry

Table 3a. GPS locations of breccia clast samples and type of analyses conducted on the sample.

Sample Number	GPS location	Rock collected/analyzed for:
8230-1B	37.612462° N, -118.99195° W	▪ Whole-rock geochemistry ▪ Petrographic thin sections
8230-1D	37.612462° N, -118.99195° W	▪ Whole-rock geochemistry ▪ Petrographic thin sections ▪ Zircon geochronology ▪ Zircon geochemistry
8230-3A-1*	37.612462° N, -118.99195° W	▪ Whole-rock geochemistry ▪ Petrographic thin sections
8230-3A-2*	37.612462° N, -118.99195° W	▪ Whole-rock geochemistry ▪ Petrographic thin sections
8230-3B*	37.612462° N, -118.99195° W	▪ Whole-rock geochemistry ▪ Petrographic thin sections

Table 3b. GPS locations of breccia clast samples and type of analyses conducted on the sample.

APPENDIX B

Samples were collected in-situ in all cases except where outcrop access was limited. In this case samples were collected from a talus pile at the base of the outcrop (made up of eroded breccia blocks from the outcrop) and are indicated by a *.

Sample Number	Description
72720-2C*	*Hand sample:* Polymictic breccia float from facies 3. Clast is subrounded, white-gray volcanic clast, 5 cm in diameter with 3% black pyroxene phenocrysts ≤ 2 mm. *Thin section:* Fine-grained groundmass with chlorite and epidote alteration makes up 92% of rock. Phenocrysts throughout include: 3% subhedral to anhedral plagioclase with small amounts of sericite and epidote alteration; 2% subhedral to anhedral clinopyroxene; < 1% subhedral biotite; and 2% anhedral oxides.
72720-2E-1* ***K-spar stain	*Hand Sample:* Polymictic breccia float from facies 3. Clast is subangular, black volcanic clast, 8 cm in diameter with 10% plagioclase feldspar phenocrysts ranging from ≤ 1 mm - 2 mm. *Thin Section:* Fine-grained groundmass with epidote and sericite alteration makes up 89% of rock. Phenocrysts throughout include: 4% subhedral to anhedral plagioclase with sericite and epidote alteration and black alteration rims; 2% anhedral potassium feldspar with exsolution lamellae; 2% subhedral to anhedral clinopyroxene; ≤ 1% subhedral to anhedral hornblende black rims pr partial black cores; 1% subhedral to anhedral

	muscovite; and 1% anhedral oxides. Glomerocrysts throughout are dominantly subhedral to anhedral plagioclase and potassium feldspar with minor amounts of clinopyroxene.
72720-2E-2*	*Hand Sample:* Polymictic breccia groundmass sample float from facies 3. Groundmass is gray and fine grained. *Thin Section:* Fine-grained groundmass with epidote alteration and minor chlorite alteration makes up 92% of rock. Phenocrysts throughout include: 4% subhedral to anhedral plagioclase with minor zoning; 1% subhedral potassium feldspar with exsolution lamellae; < 1% anhedral clinopyroxene; ≤ 1% subhedral hornblende; and 1% anhedral oxides. Glomerocrysts are dominantly subhedral to anhedral plagioclase with minor amounts of clinopyroxene and hornblende.
72920-4A	*Hand Sample:* Polymictic breccia sample from facies 3. On the weathered surface, clast is white with black spots that is 9 cm in size. On the fresh surface. Clast is subrounded, black volcanic with feldspar phenocrysts. *Thin Section:* Fine-grained groundmass with dominantly sericite alteration and minor epidote alteration makes up 90% of the rock. Phenocrysts throughout include: 4% subhedral to anhedral plagioclase with resorption texture and rare zoning; 1% subhedral to anhedral potassium feldspar with exsolution lamellae; < 1% anhedral clinopyroxene; ≤ 1% anhedral hornblende; 1% subhedral to anhedral biotite with chlorite alteration; 1% subhedral to anhedral muscovite with sericite alteration; and ≤ 2% anhedral oxides. Glomerocrysts are present and include dominantly

	subhedral to anhedral plagioclase with less dominant clinopyroxene and chlorite.
72920-5A	*Hand Sample:* Polymictic breccia sample from facies 3. Clast is subangular, black volcanic clast, 7.5 cm in diameter with 5% plagioclase feldspar phenocrysts ranging from ≤ 1 mm - 6 mm. *Thin Section:* Fine-grained groundmass with epidote, chlorite, and sericite alteration makes up 93% of the rock. Phenocrysts throughout include: 3% subhedral to anhedral plagioclase with resorption texture and epidote alteration; 1% subhedral to anhedral biotite with chlorite alteration; 2% subhedral to anhedral muscovite with sericite alteration; and ≤ 1% anhedral oxides.
72920-5B	*Hand Sample:* Polymictic breccia sample from facies 3. Clast is subangular, white-gray volcanic clast, 6 cm in diameter with 2% black pyroxene phenocrysts ≤ 2 mm. *Thin Section:* Fine-grained groundmass with epidote and sericite alteration makes up 93% of the rock. Phenocrysts throughout include: 1% subhedral to anhedral plagioclase; 2% subhedral to anhedral biotite; 1% anhedral muscovite; < 1% anhedral hornblende; and < 2% anhedral oxides. Glomerocrysts are present and include dominantly subhedral to anhedral plagioclase with sericite and epidote alteration.
72920-5C	*Hand Sample:* Polymictic breccia sample from facies 3. Clast is subangular, black volcanic clast, 5 cm in diameter with 3% plagioclase feldspar phenocrysts ranging from ≤ 1 mm - 4 mm.

	Thin Section: Fine-grained groundmass with dominantly sericite alteration and minor epidote and chlorite alteration makes up 92% of the rock. Phenocrysts throughout include: 3% subhedral to anhedral plagioclase with resorption texture, sericite alteration, and black alteration rims; 2% subhedral to anhedral biotite; 1% anhedral muscovite; 1% anhedral hornblende; and 1% anhedral oxides. Glomerocrysts are present and include anhedral plagioclase.
73020-1A	*Hand Sample:* Monomictic breccia sample from facies 1. Clast is angular, black volcanic, 10 cm in diameter with 2% feldspar phenocrysts ranging from ≤ 1 mm - 4 mm. *Thin Section:* Fine-grained groundmass with epidote and sericite alteration makes up 93% of the rock. Phenocrysts include: 2% subhedral to anhedral plagioclase; 1% anhedral potassium feldspar; 2% anhedral biotite; 1% subhedral to anhedral muscovite; and < 1% oxides. Glomerocrysts are present and include dominantly subhedral to anhedral plagioclase with potassium feldspar, muscovite, and oxides.
73020-1B	*Hand Sample:* Monomictic breccia sample from facies 1. Clast is angular, black volcanic clast that is 6 cm in diameter with 5% feldspar phenocrysts ranging from ≤ 1 mm - 4 mm. *Thin Section:* Fine-grained groundmass with dominantly epidote alteration and minor sericite and chlorite alteration makes up 85% of the rock. Phenocrysts include: 8% subhedral to anhedral plagioclase; 2% anhedral potassium feldspar; 1% anhedral biotite; 2% subhedral to anhedral

	muscovite; 1% subhedral to anhedral hornblende; and < 1% oxides. Glomerocrysts are present and include dominantly subhedral to anhedral plagioclase with varying phenocrysts of potassium feldspar, biotite, muscovite, hornblende, oxides and sericite alteration.
73020-1C	*Hand Sample:* Monomictic breccia sample from facies 1. Clast is subangular, black volcanic clast, 7 cm in diameter with 2% feldspar phenocrysts ranging from ≤ 1 mm - 3 mm. *Thin Section:* Fine-grained groundmass with dominantly epidote alteration and minor chlorite alteration makes up 91% of the rock. Phenocrysts include: 3% subhedral to anhedral plagioclase with sericite and chlorite alteration; 2% anhedral potassium feldspar; 1% anhedral biotite; 1% subhedral to anhedral muscovite; < 1% euhedral to subhedral hornblende; and < 1% anhedral oxides. Glomerocrysts are present and include dominantly anhedral plagioclase with biotite and muscovite.
8230-1B ***K-spar stain	*Hand Sample:* Polymictic breccia sample from facies 3. Clast is a subrounded, black volcanic clast, 6.5 cm in diameter with 3% feldspar phenocrysts ranging from ≤ 1 mm - 5 mm. *Thin Section:* Fine-grained groundmass with dominantly epidote alteration and minor sericite and chlorite alteration makes up 92% of the rock. Phenocrysts include: 3% subhedral to anhedral plagioclase with epidote, sericite and chlorite alteration; 1% subhedral to anhedral potassium feldspar; 2% subhedral to anhedral biotite; < 1% subhedral to anhedral muscovite; and < 1% oxides.

8230-1D	*Hand Sample:* Polymictic breccia sample from facies 3. Clast is a subangular, black volcanic clast, 5 cm in diameter with 3% feldspar phenocrysts ranging from ≤ 1 mm - 5 mm. *Thin Section:* Fine-grained groundmass with epidote alteration makes up 92% of the rock. Phenocrysts include: 4% subhedral to anhedral plagioclase with resorption texture, and secondary growth of smaller plagioclase phenocrysts on the rims of the larger phenocrysts; 1% anhedral potassium feldspar; 1% euhedral to subhedral muscovite; and 2% oxides. Glomerocrysts are present and include subhedral to anhedral quartz.
8230-3A-1*	*Hand Sample:* Polymictic breccia sample from facies 3. Sample is the breccia groundmass with marble and metasedimentary clasts. Groundmass is gray and very fine grained. Marble clast is white, subrounded and 1.5 cm in diameter. Metasedimentary clast is gray, fine grained, subangular and 2 cm in diameter. *Thin Section:* Fine-grained groundmass with dominantly chlorite and epidote alteration makes up 92% of the rock. Phenocrysts include: 2% subhedral to anhedral plagioclase; 2% anhedral hornblende with black alteration rims and cores; 2% quartz with undulose extinction and minor intergrowth of chlorite laths; < 1% subhedral zircon; and < 1% oxides. Glomerocrysts are present and include subhedral to anhedral plagioclase.
8230-3A-2*	*Hand Sample:* Polymictic breccia sample from facies 3. Clast is subrounded, purple-gray devitrified volcanic clast, 7 cm in diameter with phenocrysts eroded out.

	Thin Section: Fine-grained groundmass with dominantly epidote alteration and minor chlorite alteration makes up 95% of the rock. Phenocrysts include: < 2% subhedral to anhedral plagioclase with sericite and epidote alteration in larger phenocrysts; 2% total of the following phenocrysts: anhedral clinopyroxene with embayment, anhedral biotite, subhedral to anhedral muscovite, and 1% oxides.
8230-3B*	*Hand Sample:* Polymictic breccia sample from facies 3. Clast is a subangular, black volcanic clast, 8 cm in size with 3% feldspar phenocrysts ranging from ≤ 1mm - 5 mm. *Thin Section:* Fine-grained groundmass with dominantly epidote alteration and minor chlorite alteration makes up 93% of the rock. Phenocrysts include: 3% subhedral to anhedral plagioclase with minor sericite and epidote alteration; 1% subhedral to anhedral clinopyroxene; 1% anhedral biotite; < 1% subhedral hornblende; and 1% oxides. Glomerocrysts are present and include dominantly subhedral to anhedral quartz with minor anhedral potassium feldspar.

Table 4. Hand sample and thin sections descriptions of breccia samples.

APPENDIX C

Sample	Si (cps)	P (cps)	Ti (ppm)	Y (ppm)	Zr (ppm)	La (ppm)	Ce (ppm)	Pr (ppm)	Nd (ppm)	Sm (ppm)
72720-2E A-1	1.90E+07	364	1.95	1173	4.61E+05	0	14.82	0.056	1.39	3.99
72720-2E A-2	1.81E+07	383	1.12	1449	4.61E+05	0.054	11.34	0.093	2.59	6.45
72720-2E A-3	1.88E+07	191	3.11	718	4.50E+05	0.013	11.14	0.04	1.06	2.15
72720-2E A-4	1.87E+07	296	3.39	986	4.53E+05	0.009	15.4	0.056	1.12	2.94
72720-2E A-5	1.85E+07	343	1.71	1045	4.67E+05	0.108	19.43	0.155	1.42	3.2
72720-2E A-6	1.85E+07	193	2.74	835	4.62E+05	0.027	24.79	0.087	1.22	2.41
72720-2E A-7	1.91E+07	389	1.49	1671	4.66E+05	0.027	12.31	0.13	2.88	6.84
72720-2E A-8	1.86E+07	423	3.4	1667	4.61E+05	0.063	12.77	0.195	3.43	8.81
72720-2E A-9	1.92E+07	382	4.2	1392	4.72E+05	0.022	15.8	0.09	1.67	4.32
72720-2E B-1	1.83E+07	296	4.8	1093	4.45E+05	0	12.19	0.09	1.67	3.97
72720-2E B-2	1.88E+07	313	4.2	1420	4.47E+05	0.036	12.41	0.288	5.43	8.5
72720-2E B-3	1.79E+07	322	3.9	1810	4.53E+05	0.031	15.3	0.449	7.32	11.7
72720-2E B-4	1.84E+07	340	3.5	1483	4.53E+05	0.022	13.59	0.207	4.94	9.2
72720-2E B-5	1.90E+07	555	2.5	2340	4.61E+05	0.1	22.23	0.195	3.16	8.18
72720-2E B-6	1.88E+07	261	5.6	1928	4.39E+05	0.072	15.2	0.445	8.51	15.4
72720-2E B-7	2.02E+07	136.6	2.33	784	4.68E+05	0.279	15.8	0.152	1.12	2.34
72720-2E B-8	1.92E+07	311	4.4	1690	4.51E+05	0.0045	26.5	0.093	2.12	5.4
72720-2E B-9	1.96E+07	421	3.3	2150	4.53E+05	0.036	24.2	0.35	5.92	13.2
72720-2E B-10	1.82E+07	266	5.2	826	4.31E+05	0.054	10.97	0.093	2.35	4.65
72720-2E B-11	1.87E+07	217	5.1	1178	4.46E+05	0.022	15.47	0.192	2.49	4.53
72720-2E B-12	1.88E+07	289	5.2	1315	4.59E+05	0.018	21.1	0.105	2.26	5.49
72720-2E B-13	1.86E+07	213	6.1	714	4.56E+05	0.0045	8.71	0.09	1.53	2.8
73020-1A A-1	1.84E+07	310	3.6	1499	4.32E+05	0.067	20.1	0.164	4.45	8.34
73020-1A A-2	1.79E+07	377	3.16	1191	4.43E+05	1.48	29.8	0.47	3.6	3.55
73020-1A A-3	1.76E+07	350	2.49	1059	4.39E+05	2.3	29.8	0.67	4.6	3.78
73020-1A A-4	1.76E+07	138.4	2.8	904	4.38E+05	0.013	22.2	0.019	1.02	2.8
73020-1A B-1	1.94E+07	358	2.42	1726	4.48E+05	1.88	27.8	0.43	3.43	4.63
73020-1A B-2	1.88E+07	260	1.82	1328	4.39E+05	0.067	32.4	0.096	1.53	4.02
73020-1A B-3	1.74E+07	260	0.65	940	4.30E+05	0.067	13.96	0.068	1.47	3.64
73020-1B 3-1	1.93E+07	282	2.31	1506	4.55E+05	0.77	36.9	0.32	2.9	4.77
73020-1B 3-2	1.82E+07	366	2.2	1671	4.59E+05	0.009	25.02	0.111	1.69	5
73020-1B 3-3	1.87E+07	530	2.07	1102	4.60E+05	3.94	32.2	1	5.8	3.95
73020-1B 3-4	1.86E+07	277	1.95	1494	4.60E+05	0.013	26.5	0.062	1.27	3.81
73020-1B 3-5	1.92E+07	418	4.3	1060	4.64E+05	6.5	47.5	1.8	11.8	8.2
73020-1B 3-6	1.90E+07	376	14.9	2090	4.36E+05	3.91	201	15.7	109	69.1
73020-1B 3-7	1.81E+07	562	12.6	2120	4.48E+05	2.8	19.8	1.71	16.9	21.3
73020-1B 3-8	1.98E+07	262	4.17	999	4.76E+05	0.198	64	0.95	7.2	7.4
73020-1B 3-9	1.78E+07	349	19.2	1440	4.19E+05	3.7	112	11	82	50
73020-1B 3-10	1.90E+07	526	30	1724	4.52E+05	1.48	49.9	1.2	10	12
73020-1B 3-11	1.93E+07	2030	7.6	2042	4.71E+05	10.36	38.8	5.16	33.6	18.8
73020-1B 3-12	1.88E+07	424	9.2	1750	4.52E+05	1.22	76	5.7	46.5	35.5
73020-1B 3-13	1.86E+07	252	19.1	489	4.31E+05	0.031	19.8	0.111	2.02	3.18
73020-1C B-1	1.87E+07	364	11.1	1312	4.13E+05	0.031	56.4	0.288	4.84	9.4
73020-1C B-2	1.89E+07	334	13.4	1559	4.41E+05	2	53.7	0.58	6.55	10.9
8230-1D A-1	1.88E+07	1420	2.07	913	4.32E+05	25.4	70.4	6.79	33.8	9.2
8230-1D A-2	1.82E+07	148	1.38	861	4.39E+05	0.009	16.52	0.028	0.55	2.36
8230-1D A-4	1.73E+07	292	16.7	1151	4.01E+05	0.99	22.4	0.32	1.94	3.69
8230-1D A-5	1.88E+07	237	4.9	1532	4.25E+05	0.009	33.6	0.18	2.02	3.99

Table 5a. Zircon trace element geochemical data for 48 zircon from the breccia of Mammoth Rock.

Sample	Eu (ppm)	Gd (ppm)	Tb (ppm)	Dy (ppm)	Ho (ppm)	Er (ppm)	Tm (ppm)	Yb (ppm)	Lu (ppm)	Hf (ppm)
72720-2E A-1	0.369	16.6	6.41	89.5	37.6	192.7	43.8	443	100.5	12080
72720-2E A-2	0.653	23.2	8.2	104	46.8	225.6	53.6	551	128.6	11620
72720-2E A-3	0.476	9.27	3.32	48.2	21.18	119	29.4	312	77.6	10260
72720-2E A-4	0.52	11.22	4.58	64.6	29.9	161.3	39.9	446	106.2	11200
72720-2E A-5	0.65	12.7	5.28	69.1	31.41	165.2	41.3	451	111	11620
72720-2E A-6	0.56	12.49	4.39	59.8	25.7	129.5	31.4	330	78.5	11590
72720-2E A-7	0.84	29.7	10.83	127.6	54.4	258	59.8	597	133.9	12150
72720-2E A-8	0.8	30.2	9.97	129.1	53.9	263.4	60.7	621	135.1	11850
72720-2E A-9	0.516	21.1	7.63	103.1	43.2	212.9	51.8	528	119	11200
72720-2E B-1	0.79	16.2	5.73	77.1	34	174	40	447	103.2	8290
72720-2E B-2	1.8	27.9	9.17	110.8	44	216	48.9	509	117.5	8450
72720-2E B-3	1.98	36.2	11.73	143.4	56.8	273	63.5	630	143.1	9070
72720-2E B-4	1.36	27.3	9.25	115.4	46.4	223	50.6	520	121	9440
72720-2E B-5	0.85	32.2	11.88	171.9	71.9	367	88.2	922	206.9	11960
72720-2E B-6	2.78	43.3	14.18	161.9	65.9	298	67.4	677	146.7	9200
72720-2E B-7	0.345	8.8	3.63	49	23	121.4	31.4	353	83.3	11570
72720-2E B-8	0.95	23.8	8.58	126.8	55.6	282	68	691	157	1.02E+04
72720-2E B-9	2.19	42.6	14.2	180	72	332	75.5	764	168.3	9580
72720-2E B-10	0.66	13.1	4.67	61	25.3	133.4	32.2	355	82.4	9760
72720-2E B-11	1.03	17.6	6.27	86.3	36.3	180.1	45.2	481	113.5	9230
72720-2E B-12	1.15	20.8	7.59	98.3	41.6	208.6	49.5	518	116.5	8910
72720-2E B-13	0.63	10.2	4.19	51.6	22.3	116	28.5	305	69.3	8500
73020-1A A-1	1.39	23.3	8.94	108.3	45.5	230.2	59.1	609	145.7	7740
73020-1A A-2	0.57	12.89	5.16	73.6	34.2	197.2	50.5	581	137.6	10460
73020-1A A-3	0.65	14.9	5.15	74.4	32.8	175.3	44.5	509	122.2	10150
73020-1A A-4	0.407	9.87	3.93	55.9	27.3	147.9	39.6	438	105.2	10450
73020-1A B-1	0.78	22.4	8.99	121.9	54.5	271.9	66.5	730	156.8	11900
73020-1A B-2	0.78	17.3	6.78	96.5	40.6	214.3	53.8	563	120.5	10800
73020-1A B-3	0.72	13.1	4.98	68.6	29.9	159.3	37.4	429	95.3	9820
73020-1B 3-1	0.79	20.7	7.92	114.4	47.3	239	55.4	594	133.9	10980
73020-1B 3-2	0.86	22.3	8.2	114.3	49.7	262	62.5	672	154.7	10650
73020-1B 3-3	0.482	15.45	6.17	81.6	33.8	177	42.7	445	103.2	1.19E+04
73020-1B 3-4	0.708	17.2	6.46	94.8	43.3	239.2	60.8	661	149.8	11330
73020-1B 3-5	0.73	19.9	7.17	87.6	33.9	160.1	35.2	339	69.1	1.05E+04
73020-1B 3-6	21.9	80.5	21.5	203	61	236	48.2	453	93.1	1.16E+04
73020-1B 3-7	1.21	64.1	19.6	218	76.4	315	59.8	500	97.4	9440
73020-1B 3-8	1.49	16	5.77	72.4	30.7	153.6	36.9	402	87.5	13200
73020-1B 3-9	15.8	52.2	15.3	146	40.6	169	38.2	379	86.3	10830
73020-1B 3-10	1.37	35.4	11.78	151.8	56.1	251.2	52.6	494	95.9	10790
73020-1B 3-11	1.81	47.1	14.82	178.9	67.2	303	62.6	583	115.2	8970
73020-1B 3-12	8.5	53.5	16.6	181	57.3	242	48	423	82.1	10860
73020-1B 3-13	0.46	11	3.33	43.7	16.46	75.6	16.01	152.1	31.6	9110
73020-1C B-1	1.46	28	10	110.4	44.3	209	43.8	411	81.4	8950
73020-1C B-2	1.82	35.1	11.33	141.3	51.4	250	53.9	524	106.9	10320
8230-1D A-1	0.54	15	4.92	63.4	26.4	140.8	35.7	407	88.7	1.08E+04
8230-1D A-2	0.302	11	4.01	59.1	25.5	134	36.1	388	84.1	10650
8230-1D A-4	0.568	13	5.16	77.5	35.2	186.4	46.1	533	115.6	1.03E+04
8230-1D A-5	0.77	17	7.19	105.7	46.6	247	65.5	708	153.8	9150

Table 5b. Zircon trace element geochemical data for 48 zircon from the breccia of Mammoth Rock.

Sample	Si (ppm)	P (ppm)	Ti (ppm)	Y (ppm)	Zr (ppm)	Nb (ppm)	La (ppm)	Ce (ppm)	Pr (ppm)	Nd (ppm)
72820-1	1.52E+05	145	2.3	1035	4.30E+05	1.74	-2.1	9.9	0.35	2.16
72820-2	1.51E+05	144.4	2.23	2051	4.30E+05	6.89	-7	21.56	0.37	2.5
72820-3	1.54E+05	103.6	3.13	1281	3.99E+05	7.18	0.79955	22.89	0.083	0.71
72820-4	1.54E+05	144	1.47	1111	4.28E+05	5.15	-20	25.3	0.6	2.2
72820-5	1.51E+05	124	1.42	521	4.08E+05	1.86	-4.2	4.74	0.052	0.28
72820-6	1.49E+05	3.80E+03	3.9	1322	3.99E+05	6.53	-2620	169	68	112
72820-7	1.46E+05	124	1.73	701	4.18E+05	2.14	0	12.67	0.073	0.59
72820-8	1.47E+05	167	2.66	1059	4.10E+05	3.39	-28.1	16	0.367	1.46
72820-9	1.56E+05	173	1.02	815	4.12E+05	2.56	0	11	0.039	0.6
72820-10	1.57E+05	236	26	2290	3.87E+05	4.41	-69	21.1	1.36	6.8
72820-11	1.54E+05	99	1.45	1165	4.22E+05	6.05	-0.26	23.5	0.101	1.07
72820-12	1.54E+05	101.1	1.89	951	4.23E+05	3.48	-1	10.87	0.155	0.71
72820-13	1.53E+05	197	1.68	947	4.23E+05	2.89	-19.2	9.18	0.146	0.52
72820-14	1.52E+05	115	2.13	1215	4.39E+05	7.01	-1.3	16.25	0.109	0.67
72820-15	1.49E+05	140	4.5	980	4.27E+05	3.6	-9.3	13.8	0.22	1.11
72820-16	1.55E+05	143	2.11	890	4.32E+05	2.83	-1.1	9.4	0.036	0.74
72820-17	1.48E+05	123.7	3.4	1088	4.22E+05	6.56	-24.7	13.3	0.162	0.63
72820-18	1.53E+05	103	4.1	369	4.22E+05	0.85	-29.2	4.78	0.39	1.43
72820-19	1.50E+05	152	2.15	693	4.22E+05	1.92	-0.9	6.55	0.1	0.52
72820-20	1.54E+05	159	1.76	776	4.13E+05	2.52	-14.9	8.26	0.052	0.59
72820-21	1.53E+05	200	1.82	1290	4.26E+05	5.06	-1.6	12.8	0.106	1.05
72820-22	1.55E+05	273	1.73	3920	4.50E+05	8.24	-84	34.3	1.65	7.5
72820-23	1.52E+05	2.90E+03	2.13	959	4.01E+05	2.93	-1.70E+04	330	113	170
72820-24	1.23E+05	22.9	1.29E+05	438	375	423	-1.15E+05	2744	895	1326
72820-25	1.55E+05	188	2.49	1218	4.32E+05	4.78	-120	18.2	1	1.9
72820-26	1.53E+05	227	3.5	1356	4.33E+05	4.53	-8	13.78	0.086	1.25
72820-27	1.49E+05	88.9	3	838	4.19E+05	4.79	-2.5	18.9	0.099	0.66
72820-28	1.51E+05	136	1.63	1657	4.42E+05	10.8	0	23.7	0.09	1.05
72820-29	1.48E+05	89	5.2	344	4.33E+05	0.95	0	4.73	0.108	0.55
72820-30	1.50E+05	2060	1.55	1231	4.22E+05	3.92	-2.80E+03	59	22	64
72820-31	1.45E+05	152	2.18	880	4.10E+05	3.09	-47	10.69	0.18	0.64
72820-32	1.50E+05	237	1.47	1261	4.24E+05	4.2	0	12.28	0.063	0.52
72820-33	1.63E+05	195	1.16	1213	4.29E+05	5.24	-43	19.64	0.135	1.08
72820-34	1.50E+05	147	15.5	2670	4.30E+05	3.8	-8.8	17.76	1.81	13.4
72820-35	1.55E+05	127	2.32	1070	4.41E+05	1.3	-2.7	8.3	0.55	3.67
72820-36	1.54E+05	104.9	2.25	1311	4.17E+05	6.64	-10	20.3	0.09	1.15
72820-37	1.47E+05	305	9.8	3550	4.34E+05	8.8	-31	38.1	0.89	8.5
72820-38	1.54E+05	175	2.8	1497	4.43E+05	7.05	-244	18.1	0.27	1.27
72820-39	1.59E+05	184	0.87	1390	4.46E+05	3.43	-55	15.4	0.188	1.95
72820-40	1.60E+05	153	3.37	2230	4.40E+05	9.46	-175	32.9	0.4	3.36
72820-41	1.56E+05	200	1.32	1111	4.48E+05	3.94	-15	14.2	0.026	0.72
72820-42	1.54E+05	368	5.7	4380	4.29E+05	7.14	233	68.2	1.92	15.1
72820-43	1.61E+05	235	1.82	1077	4.34E+05	3.12	8.7	10.4	0.054	0.67
72820-44	1.50E+05	144	1.54	1415	4.29E+05	6.06	21	17.92	0.2	1.19
72820-45	1.51E+05	186	1.24	1023	4.29E+05	2.61	0	10.85	0.062	0.44
72820-46	1.57E+05	192	3.65	2600	4.42E+05	3.92	33	25.1	1.03	7.69
72820-47	1.57E+05	110	4	822	4.14E+05	2.44	3.2	9.3	0.214	1.43
72820-48	1.54E+05	650	4.7	1040	4.13E+05	2.83	1.50E+03	25	4.8	8.7
72820-49	1.50E+05	98	4.2	1274	4.26E+05	5.53	27	34.1	0.25	1.68
72820-50	1.48E+05	99	2.42	1076	4.15E+05	5.3	0	19.3	0.071	0.87
72820-51	1.39E+05	4.50E+03	1.14	740	3.97E+05	2.83	2360	70	29	60
72820-52	1.63E+05	169	4.5	3070	4.35E+05	4.49	7.8	33.3	1.44	10.6
72820-53	1.61E+05	96.2	3.1	1099	4.28E+05	1.25	3.1	7.2	0.53	3.56
72820-54	1.48E+05	193	3.11	2850	4.08E+05	2.34	23	12.4	0.42	5.48

Table 6a. Zircon trace element geochemical data for 266 detrital zircon from the sandstone of Mammoth Rock.

Sample	Sm (ppm)	Eu (ppm)	Gd (ppm)	Tb (ppm)	Dy (ppm)	Ho (ppm)	Er (ppm)	Tm (ppm)	Yb (ppm)	Lu (ppm)	Hf (ppm)
72820-1	2.4	0.95	17.2	6.03	76	33.1	157	46.6	473	96.9	9080
72820-2	4.17	1.29	28.1	10.76	153.1	64.5	344	91.2	905	183.4	10040
72820-3	1.69	0.64	14.4	5.78	87.9	38.2	219.5	66.1	661	147.2	10620
72820-4	1.96	0.83	16	6.26	81.4	36.5	191	50.2	501	106.6	10540
72820-5	0.55	0.227	5.24	2.25	34.3	15.2	91.2	26	291	63.8	10210
72820-6	12	2.46	28	7.95	103.6	40.4	202.6	55.9	556	118.4	9780
72820-7	1.04	0.415	7.9	2.98	47.3	20.9	118	34	356	79	9990
72820-8	2.04	0.69	13.5	5.04	73.9	31.9	174.3	50.6	490	116.5	9490
72820-9	0.88	0.291	8.2	3.68	53.7	24.8	137	38.9	414	92.9	10360
72820-10	7.6	3.6	47	16	205	80	379	93	900	182	7880
72820-11	1.32	0.665	12.9	5.04	76.4	35.1	210	61.6	593	135.1	10660
72820-12	1.34	0.51	11.4	4.55	63.5	29.6	156.6	44.7	453	103.1	9690
72820-13	1.11	0.339	10.5	4.71	65.3	29.6	163.8	44.9	462	98	10820
72820-14	1.36	0.56	12.7	5.4	83.8	37.2	211	57.9	642	138.5	10620
72820-15	1.45	0.61	13.5	5.4	72	32.4	169	46	430	98	9010
72820-16	0.94	0.47	10.2	4.16	63	27.6	156	41.8	447	94	9900
72820-17	1.36	0.51	11.1	4.6	69.9	31.5	196	54.8	576	126.7	10300
72820-18	0.87	0.62	4.5	1.91	26	11.6	63	16.9	182	39.9	9250
72820-19	0.77	0.301	8	2.86	48.2	21.2	115.7	33.9	335	77.4	9920
72820-20	0.83	0.34	6.9	3.52	50.8	23.8	135	36.7	400	90.5	10650
72820-21	1.7	0.61	13.6	6.24	91.5	41.5	230	59.9	599	131.4	10090
72820-22	9.42	2.32	65.4	26.7	339	131.5	674	170	1480	301	10930
72820-23	15	2.3	23.4	5.6	69	27.7	156.7	46	468	103.7	10110
72820-24	104.2	32.8	95.4	12.21	70.4	14.23	44.5	6.64	40.6	8.07	37.4
72820-25	1.48	0.65	13.1	5.5	78.3	36.4	197.3	56.3	567	130.4	9970
72820-26	1.69	0.659	14.8	6.68	98.2	42.5	222	61	611	132.6	10290
72820-27	1.43	0.52	12.7	4.51	64.7	26.7	140	38.6	392	78.8	10100
72820-28	1.86	0.72	16.6	7.39	108.3	51.1	289	81.7	827	179	10340
72820-29	0.64	0.404	4.8	1.69	24.5	10.49	55.8	14.8	141.6	32.1	8860
72820-30	8.1	1.28	19.3	6.6	88.8	35.9	193	55.3	528	112.5	10180
72820-31	1.12	0.468	9.1	4.2	57.8	26.2	150	42.3	423	93.6	9890
72820-32	1.36	0.54	13.4	6.01	86.9	37.7	211	59.2	590	128.4	10330
72820-33	1.7	0.599	15.7	6.4	88.3	36.6	199	53.4	531	111.1	10710
72820-34	13.96	0.63	74.2	24.5	290	96.1	409	85.4	660	108.6	10410
72820-35	3.31	1.28	18.1	6.79	86	32.2	176	42.8	404	85.8	9140
72820-36	1.4	0.72	12.5	5.72	89.7	40.4	236	67.2	712	153	10350
72820-37	9.7	3.55	63.8	24.1	283	116	574	144	1250	267	8800
72820-38	1.77	0.72	16.2	7.15	104	47.2	253	71.2	729	152.2	10380
72820-39	2.73	0.86	19.5	7.29	99.5	42	227	62.5	610	125.6	10400
72820-40	3.88	1.75	28.4	11.37	162.5	69.9	375	103.8	992	210	10100
72820-41	1.5	0.45	11.4	4.65	73.7	33.7	187	52	552	121.4	10890
72820-42	15.3	8.31	85.6	30.5	366	136.4	663	171.1	1580	340	8920
72820-43	1.42	0.404	10.8	4.91	73.9	31.4	179	47.1	465	105.3	10050
72820-44	1.85	0.86	16.8	7.03	101	43.9	243	66.6	681	146	10380
72820-45	1.14	0.464	10	4.6	67.2	29.8	168.7	47.3	488	111.3	10350
72820-46	7.77	3.03	47.6	17.7	213	80	412	103.2	1038	206	8940
72820-47	1.39	0.49	10.38	4.13	56.3	24.8	137.2	37.7	379	85.5	9690
72820-48	3.5	1.42	18.3	6.9	93	34.7	173	41.7	417	92	9960
72820-49	2.57	1.12	16.9	7.12	93.8	38.6	205	55.4	546	118.9	9300
72820-50	1.38	0.6	12.6	5.41	75.7	32.4	194	51.5	535	119	10570
72820-51	7.4	1.47	15.7	4.23	55	23.4	127	35.7	362	79	9810
72820-52	11.2	4.34	64.1	21.1	255	95.6	475	124.1	1137	234.2	9400
72820-53	3.44	1.43	18.4	6.78	88.5	32.2	170.7	41.5	424	89.3	8810
72820-54	6.83	1.49	57.5	21.1	267	99.8	461	100.1	832	150.4	9920

Table 6b. Zircon trace element geochemical data for 266 detrital zircon from the sandstone of Mammoth Rock.

Sample	Si (ppm)	P (ppm)	Ti (ppm)	Y (ppm)	Zr (ppm)	Nb (ppm)	La (ppm)	Ce (ppm)	Pr (ppm)	Nd (ppm)
72820-55	1.49E+05	137	3.8	598	4.38E+05	1.2	0	5.97	0.115	0.78
72820-56	1.58E+05	109	1.93	1158	4.20E+05	5.78	0.9	17.3	0.049	0.83
72820-57	1.48E+05	104.4	131	556	4.21E+05	6.65	0.8	20.9	0.159	1.03
72820-58	1.52E+05	134	2.67	980	4.34E+05	2.2	3.6	16.2	0.186	1.9
72820-59	1.53E+05	105.8	4.09	554	4.31E+05	1.69	0	6.61	0.141	0.78
72820-60	1.59E+05	99.7	1.89	1248	4.15E+05	6.69	20.9	17.1	0.214	0.86
72820-61	1.53E+05	163	1.25	1870	4.17E+05	3.75	6	18.2	0.23	2.63
72820-62	1.60E+05	173	1.31	920	4.34E+05	3.19	16.2	11.5	0.132	0.91
72820-63	1.55E+05	160	2.57	2550	4.34E+05	15.6	2.7	37.4	0.158	1.62
72820-64	1.50E+05	146	1.33	770	4.29E+05	2.86	-0.6586	8.1	0.069	0.49
72820-65	1.50E+05	243	9	2450	4.15E+05	4.56	32	25.1	1.2	7.03
72820-66	1.58E+05	181	1.76	1153	4.26E+05	3.38	1.3	13.8	0.149	1.05
72820-67	1.47E+05	181	1.39	856	4.11E+05	3.08	0.2	9.99	0.019	0.6
72820-68	1.54E+05	197	1.4	1417	4.25E+05	5.5	1.3	14.3	0.12	0.75
72820-69	1.54E+05	67	2.29	358	4.27E+05	0.55	0.52	5.45	0.038	0.344
72820-70	1.56E+05	76.9	2.24	836	4.23E+05	1.47	0.7	9.1	0.28	2.41
72820-71	1.52E+05	135	10.2	1050	4.20E+05	3.78	4.8	12.2	0.236	2
72820-72	1.46E+05	149	2.96	1520	4.25E+05	8.3	0.42	27.1	0.26	2.15
72820-73	1.51E+05	179	1.19	1380	4.14E+05	4.71	1.9	14.2	0.175	1.66
72820-74	1.52E+05	150	1.53	1348	4.35E+05	7.8	1.18	16.16	0.028	0.95
72820-75	1.62E+05	261	3.07	1396	4.26E+05	3.04	1.4	12.19	0.175	1.77
72820-76	1.61E+05	164	1.61	1001	4.15E+05	3.54	18.4	13.93	0.32	0.99
72820-77	1.58E+05	120	1.12	1990	4.34E+05	3.19	1.4	20.7	0.28	3.6
72820-78	1.47E+05	133.7	2.11	692	4.15E+05	2.04	-0.23	7.21	0.058	0.76
72820-79	1.51E+05	156.2	4.21	1260	4.23E+05	4.43	1.1	18.22	0.131	1.84
72820-80	1.51E+05	156	2.06	700	4.13E+05	1.66	5	8.43	0.16	0.92
72820-81	1.57E+05	202	0.91	968	4.30E+05	3.29	0	11.8	0.026	0.55
72820-82	1.48E+05	147	2.89	970	4.05E+05	1.66	0	9	0.3	2.03
72820-83	1.52E+05	242	0.91	1081	4.20E+05	3.7	1.7	14.03	0.084	0.9
72820-84	1.51E+05	62.4	1.17	410	4.19E+05	1.71	0	6.73	0	0.23
72820-85	1.54E+05	105	2.25	1422	4.08E+05	9.09	0	20.9	0.078	0.94
72820-86	1.52E+05	114	3.35	1071	4.38E+05	2.5	1.9	12.6	0.6	3.6
72820-87	1.55E+05	149	3.1	675	4.20E+05	1.09	0.16	5.82	0.061	1
72820-88	1.49E+05	162	2.41	686	4.05E+05	1.2	1.6	64.3	0.47	4.43
72820-89	1.56E+05	310	1.74	940	4.10E+05	3.29	160	23.4	3.6	7.4
72820-90	1.52E+05	161	1.71	832	4.24E+05	3.01	4.9	8.42	0.121	0.64
72820-91	1.57E+05	166	1.91	810	4.18E+05	2.24	0.57	10.1	0.112	0.71
72820-92	1.54E+05	243	3.6	2250	4.41E+05	6.32	1.8	13.19	0.164	2.3
72820-93	1.66E+05	149	2.11	2060	4.30E+05	15.01	4.3	26.4	0.16	1.22
72820-94	1.47E+05	165	2.13	1740	4.26E+05	9.5	0.82	28.6	0.215	1.49
72820-95	1.49E+05	169	1.27	775	4.08E+05	2.61	0.62	7.87	0.06	0.57
72820-96	1.52E+05	82.3	1.81	960	4.28E+05	1.26	0	8.4	0.37	2.57
72820-97	1.56E+05	130	3.7	956	4.31E+05	1.88	1.7	8.46	0.32	2.91
72820-98	1.54E+05	150	6.2	1720	4.23E+05	11.03	4.4	32.2	1.05	4.86
72820-99	1.50E+05	255	2.33	1604	4.34E+05	3.66	14	17.9	0.52	3.35
72820-100	1.54E+05	132	10.1	705	4.32E+05	0.95	-0.34999	13.41	0.197	1.4
72820-101	1.50E+05	209	3.34	954	4.26E+05	1.77	0.56	9.48	0.12	1.25
72820-102	1.53E+05	156	3.1	785	4.34E+05	1.15	-0.127076	6.44	0.197	1.23
72820-103	1.49E+05	136	1.94	1999	4.40E+05	12.5	0.44	22.87	0.075	1.61
72820-104	1.51E+05	173	1.39	996	4.45E+05	4.09	0	13.7	0.009	0.61
72820-105	1.52E+05	179	3.5	1340	4.18E+05	6.94	20.7	18.6	0.57	1.8
72820-106	1.54E+05	209	1.14	1074	4.26E+05	3.56	0	12.3	0.026	0.69
72820-107	1.52E+05	143	3.4	992	4.18E+05	2.72	0.09	10.38	0.25	1.92
72820-108	1.58E+05	119.4	4.28	710	4.30E+05	1.82	0	5.79	0.145	0.86
72820-109	1.59E+05	132	2.03	600	4.19E+05	1.12	0	5.2	0.068	0.57
72820-110	1.58E+05	119	2.54	1500	4.26E+05	9.9	0	26.5	0.162	1.81

Table 6c. Zircon trace element geochemical data for 266 detrital zircon from the sandstone of Mammoth Rock.

Sample	Sm (ppm)	Eu (ppm)	Gd (ppm)	Tb (ppm)	Dy (ppm)	Ho (ppm)	Er (ppm)	Tm (ppm)	Yb (ppm)	Lu (ppm)	Hf (ppm)
72820-55	0.95	0.479	7.4	3.12	41.5	16.8	100.2	26.7	274	63.1	9470
72820-56	1.41	0.62	13.5	5.8	84.3	35.7	194	52.6	499	107.1	10930
72820-57	1.34	0.35	9.2	3.36	42.8	16.19	89.5	21.5	202	40.5	9550
72820-58	2.18	0.7	14.7	6.3	79	32.1	170	45	470	101	10680
72820-59	1.1	0.63	7.7	3.12	42.6	16.04	90.2	23.9	253	58.6	9130
72820-60	1.42	0.54	13.5	5.77	87.6	37.5	210	60.3	609	132.5	10300
72820-61	3.82	1.26	27.3	10.52	148	60.4	314	79.7	781	167	10920
72820-62	1.11	0.6	9.8	4.54	63.2	27.7	160	44.4	463	105.1	10360
72820-63	3.1	1.15	26.6	12.33	180	77.4	423	110.9	1064	225	10730
72820-64	0.82	0.37	8.3	3.61	56	24.8	138	40.1	407	89	10100
72820-65	7.17	2.39	47.3	17.5	212.9	85.2	408	94	823	157.1	8970
72820-66	1.8	0.73	13.3	5.43	79.9	35.6	187	51.6	540	120	10460
72820-67	1.19	0.431	9.3	3.99	57.6	28.1	146.8	40.4	433	89.4	10310
72820-68	1.48	0.58	13.6	7.15	94.6	43.1	238	63	636	139.6	10560
72820-69	0.39	0.399	4.35	1.76	26.1	11.5	63	17.3	179	42.9	9230
72820-70	2.12	0.99	13	4.8	61.2	27	138	34.5	371	86.7	11020
72820-71	2	0.86	13.4	5.21	76	33	182	47.9	484	110	9420
72820-72	3.22	0.46	21.8	9	123	45.6	246	57	580	107	9940
72820-73	1.72	0.71	16.2	7.22	99.7	43.2	241	61.4	638	137	10460
72820-74	1.31	0.55	14.3	6.44	95	44.4	246	63.5	687	151.7	10580
72820-75	2.43	1.09	17.3	6.95	93.8	43.2	238	60.4	623	136.4	8590
72820-76	1.5	0.48	10.8	4.61	71.1	31.9	183.7	49	499	114.7	10740
72820-77	4.66	1.56	31.8	12.21	159	64.8	334	83.9	828	174.6	10740
72820-78	0.8	0.408	8.2	3.5	49.2	22.2	124.8	33.8	361	79	9200
72820-79	2.68	1.55	21.8	7.95	97.6	39.4	222	54.4	542	124.6	8320
72820-80	1.17	0.54	8.3	3.68	48.6	22.8	127.8	33.7	362	83.5	9550
72820-81	0.86	0.47	8.5	4.44	62.1	27.4	162	43.9	478	106	10610
72820-82	2.28	0.99	15.1	5.52	77	32.5	185	47.1	492	106	8980
72820-83	1.37	0.659	11.2	5.07	75.8	33.8	204	50.9	522	118.8	10200
72820-84	0.43	0.256	4.4	1.96	27.8	13.05	73.3	19.5	208	48.4	10370
72820-85	1.35	0.704	14.6	6.01	95	45.5	258	68.8	751	163.5	10270
72820-86	3.31	1.4	18.9	7.31	87.2	34.9	181	41.9	395	88.6	9130
72820-87	1.23	0.79	9.1	3.54	43.9	20.7	113.7	29.8	322	76.5	7740
72820-88	3.78	1.18	21	6.53	71.1	26	117.4	25	232	46.3	7760
72820-89	1.75	0.75	12.3	5	72	31.6	179	48.6	504	113	10210
72820-90	1.02	0.282	10.3	4.52	61.8	27.5	153	38.2	388	81.8	10380
72820-91	1.28	0.462	8.6	3.95	55.8	24.4	152	40.2	450	97	9440
72820-92	3.47	0.86	29.2	11.96	171.6	71.8	387	92.6	919	181.2	11440
72820-93	1.9	0.8	21.1	9.32	147	67.1	364	95.7	959	204	10540
72820-94	2.28	1.18	20	8.6	123.1	57	314	81.2	815	175	10100
72820-95	0.84	0.336	7.3	3.4	54.3	25.5	143.1	38.1	399	89.5	10270
72820-96	2.48	1.12	15.4	5.9	75	31.9	159	39.2	387	80	9100
72820-97	2.63	0.99	13.4	5.77	72.4	31.4	168	43.7	426	92.3	9080
72820-98	4.28	2.81	25.8	10.67	135.6	56.4	287	70.4	721	147.7	10370
72820-99	3.12	1.26	20.3	9.07	120.3	52.1	274	67.5	702	147.9	10470
72820-100	1.56	0.312	12.7	5.06	62.7	24.1	117.3	25.3	202	38.3	11540
72820-101	1.52	1.1	11	5.05	70	29.9	164.2	43.2	433	103.8	8000
72820-102	1.67	0.708	10.6	4.56	61.9	25.3	138	36.4	366	83.6	8500
72820-103	2.28	0.83	18.5	9.44	144	60.6	339	91	940	206.9	10580
72820-104	0.88	0.387	9.2	4.25	69.2	30.1	169	46.8	483	106.9	9910
72820-105	1.76	0.8	12.4	6.8	101.6	42.6	240	62.3	633	136	10570
72820-106	0.97	0.57	9.8	4.98	74.8	32.7	194.1	52.6	526	117.2	10270
72820-107	2.07	1	12.82	5.5	81.1	31.4	176.4	41.2	398	88.6	9920
72820-108	0.81	0.72	7.34	3.4	49.3	22.6	112.1	30.9	307	71.3	9110
72820-109	1.11	0.39	6	2.78	39.7	16.3	88	24.3	257	57	9050
72820-110	2.66	1.29	18.8	8.2	120	44.5	235	61.4	618	123	11570

Table 6d. Zircon trace element geochemical data for 266 detrital zircon from the sandstone of Mammoth Rock.

Sample	Si (ppm)	P (ppm)	Ti (ppm)	Y (ppm)	Zr (ppm)	Nb (ppm)	La (ppm)	Ce (ppm)	Pr (ppm)	Nd (ppm)
72920-01-1	1.54E+05	186	4.8	1357	4.22E+05	2.95	-0.58	12.63	0.57	2.32
72920-01-2	1.53E+05	150	2.59	984	4.24E+05	3.51	-0.12	20.3	0.31	1.29
72920-01-3	1.55E+05	139	3.71	1204	4.16E+05	2.86	-0.2	9.92	0.32	1.64
72920-01-4	1.54E+05	313	4.12	2620	4.21E+05	4.15	-0.07	23.5	1.29	6.1
72920-01-5	1.51E+05	149	4.66	1385	4.34E+05	2.68	0	12.73	0.36	2.26
72920-01-6	1.49E+05	171.5	2.85	1066	4.24E+05	2.18	-0.19	11.73	0.78	2.77
72920-01-7	1.51E+05	166	2.46	1160	4.29E+05	3.14	-0.12	14.6	0.2	1.84
72920-01-8	1.50E+05	142.2	2.64	930	4.24E+05	1.8	-0.28	11.4	0.79	3.6
72920-01-9	1.50E+05	129	3.1	550	4.27E+05	1.2	-0.07	6.84	0.23	0.91
72920-01-10	1.47E+05	203	6.5	1242	4.20E+05	3.22	-0.25	13.67	0.31	1.84
72920-01-11	1.51E+05	102	3.12	680	4.18E+05	2.16	0	8.73	0.074	0.73
72920-01-12	1.53E+05	198	4.15	1442	4.27E+05	6.2	-0.54	22.05	0.41	2.47
72920-01-13	1.62E+05	285	0.86	1270	4.19E+05	3.34	0	9.75	0.07	1.05
72920-01-14	1.53E+05	197	3.29	2203	4.17E+05	5.36	-0.13	35.5	0.6	3.99
72920-01-15	1.61E+05	186	3.6	1360	4.20E+05	3.44	0.108	15.5	0.42	2.18
72920-01-16	1.53E+05	411	2.5	1097	3.99E+05	2.61	-54.7	23.4	7.46	9.64
72920-01-17	1.44E+05	6970	2.22	1405	3.88E+05	3.85	-2.70E+03	740	250	250
72920-01-18	1.46E+05	584	8	1220	4.23E+05	2.38	-45	27	9.2	13.3
72920-01-19	1.55E+05	113	3.7	805	4.21E+05	2.19	0	11.31	0.22	1.22
72920-01-20	1.56E+05	74.3	2.16	566	4.31E+05	2.07	-0.13	14.37	0.074	0.87
72920-01-21	1.44E+05	90.6	3.02	380	4.15E+05	1.07	0.0384709	6.37	0.053	0.44
72920-01-22	1.51E+05	145	2.2	797	4.18E+05	0.93	-0.1	6.16	0.23	1.62
72920-01-23	1.54E+05	145	3.49	1640	4.16E+05	1.47	-0.22	10.8	1.11	4.7
72920-01-24	1.56E+05	141	4.43	1110	4.06E+05	2.18	-0.13	8.66	0.26	1.18
72920-01-25	1.52E+05	205	2.57	894	3.95E+05	2.17	-4.1	9.95	0.45	1.77
72920-01-26	1.54E+05	417	5.08	1502	4.01E+05	2.64	-0.54	5.31	0.43	2.1
72920-01-27	1.51E+05	116	3.58	770	4.04E+05	2.65	-0.14	9.92	0.2	1.09
72920-01-28	1.56E+05	139	1.49	1197	4.07E+05	3.99	-0.069	16.21	0.2	1.31
72920-01-29	1.52E+05	210	8.3	1390	4.13E+05	4.64	-0.48	16.9	0.53	2.01
72920-01-30	1.55E+05	146	2.26	821	4.26E+05	1.13	-0.029	8.33	0.32	1.4
72920-01-31	1.51E+05	116	2.54	827	4.27E+05	2.37	-0.18	10.52	0.25	1.1
72920-01-32	1.48E+05	157	3.93	771	4.14E+05	2.02	0	8.22	0.25	0.91
72920-01-33	1.58E+05	214	6.03	1820	4.09E+05	3.53	-0.74	27.9	1.85	9.1
72920-01-34	1.48E+05	330	1.63	639	4.13E+05	1.72	-41	23	4.7	7.9
72920-01-35	1.56E+05	122.6	0.86	1119	4.04E+05	4.91	0.0411121	12.2	0.083	0.58
72920-01-36	1.47E+05	171	3.8	2140	4.19E+05	3.92	-0.25	17.2	0.71	4.4
72920-01-37	1.47E+05	63.7	2.05	255	4.05E+05	0.7	-0.65	3.62	0.104	0.4
72920-01-38	1.54E+05	110.9	2.35	928	3.94E+05	3.05	-0.14	15.74	0.25	1.64
72920-01-39	1.52E+05	146	3.7	1417	4.14E+05	1.28	-0.22	10.36	1.05	4.47
72920-01-40	1.55E+05	167	6	1799	4.14E+05	4.76	0	18.5	0.4	1.97
72920-01-41	1.57E+05	92	3.64	411	3.98E+05	1.03	-0.18	5.08	0.041	0.435
72920-01-42	1.60E+05	173	3.27	1013	4.06E+05	3.82	-0.07	14.2	0.16	1.13
72920-01-43	1.56E+05	183	3.2	1170	4.08E+05	1.98	-0.1	11.4	0.54	2.75
72920-01-44	1.48E+05	179	4.8	990	4.02E+05	1.07	-0.19	8.2	0.44	2.52
72920-01-45	1.46E+05	211	3.43	1550	3.97E+05	5.84	-0.4	15.6	0.27	1.61
72920-01-46	1.50E+05	178	2.86	775	4.04E+05	1	0	5.33	0.165	0.58
72920-01-47	1.51E+05	194	3	701	4.05E+05	1.89	-1.14	7.74	0.187	1.37
72920-01-48	1.55E+05	90	3.3	353	4.22E+05	0.57	-0.42	3.91	0.186	1.11
72920-01-49	1.49E+05	105.4	4.63	508	4.07E+05	0.91	-0.22	5.57	0.223	0.97
72920-01-50	1.58E+05	152.3	2.49	2160	4.17E+05	6.13	-0.18	16.08	0.88	4.36
72920-01-51	1.48E+05	105	2.9	602	4.15E+05	1.9	-0.12	10.14	0.29	1.03
72920-01-52	1.46E+05	161	4.82	1150	3.83E+05	2.65	-5.7	18.7	0.77	3.26

Table 6e. Zircon trace element geochemical data for 266 detrital zircon from the sandstone of Mammoth Rock.

Sample	Sm (ppm)	Eu (ppm)	Gd (ppm)	Tb (ppm)	Dy (ppm)	Ho (ppm)	Er (ppm)	Tm (ppm)	Yb (ppm)	Lu (ppm)	Hf (ppm)
72920-01-1	2.84	1.22	20.4	7.6	110.3	46.8	225.3	54.5	562	126.6	9050
72920-01-2	1.92	0.91	13.7	5.39	79.7	30.7	156	37.7	394	88.1	10780
72920-01-3	2.54	1.06	14.7	5.75	90.3	39.6	201.5	53.4	550	123.7	8950
72920-01-4	9.7	1.18	53.6	18	247	90	379	86.2	800	152	8800
72920-01-5	2.75	1.14	18.7	7.02	104.6	43.4	221	56.4	583	130.6	9160
72920-01-6	3.59	1.35	19.9	6.76	91.1	34	164	39.7	408	86.8	10210
72920-01-7	2.17	0.778	15.9	6.16	85.4	36.9	177	48.7	490	103.7	9590
72920-01-8	4.6	1.46	18.6	6.7	80	30.8	141	35.1	358	76.8	9980
72920-01-9	1.5	0.67	7.42	2.79	41.3	16.2	81.2	22.5	238	56.7	9580
72920-01-10	2.54	1.25	17.3	7.01	94.4	41	200.9	51	539	113.6	8930
72920-01-11	1.28	0.78	9.6	3.74	51.5	21.7	110.5	28.7	303	69.5	10010
72920-01-12	3.35	1.32	22.3	8.49	117.1	45.3	218	52.8	539	115.8	10500
72920-01-13	2.15	0.37	14.4	6.41	97	41.7	213	57.5	587	123.4	10800
72920-01-14	6.1	2.01	39.8	14.8	190.4	77.4	344	87.3	840	174.9	7950
72920-01-15	3.33	1.57	23.8	8.9	112	42.7	199	49.8	491	110	9670
72920-01-16	3.43	0.548	16.2	6.95	90.4	37.9	185	44.3	450	92.4	9700
72920-01-17	27.1	5.01	36	9.04	115.9	44.1	217	54.7	561	128.7	9980
72920-01-18	5.25	1.66	21.8	7.66	106.8	41	194	53.8	523	111	10050
72920-01-19	1.73	0.9	12.4	4.82	63.5	25.1	121.2	32.4	333	71.1	9960
72920-01-20	1.07	0.472	7.48	2.89	40.3	16.5	82.7	23.8	257	57.8	10920
72920-01-21	0.77	0.294	4.95	2.15	28.9	11.9	64.2	17.7	183	43.5	9970
72920-01-22	2.2	0.63	12.6	4.57	66	26.3	128	33.8	341	80.5	9330
72920-01-23	6.3	2.45	33	11.4	146	52	243	61	620	128	8800
72920-01-24	2.27	0.94	15.6	5.91	83	34.9	166.8	45.5	473	101.6	8360
72920-01-25	2.22	0.92	11.9	5.04	72.8	28.5	148	37.3	400	88.8	9830
72920-01-26	3.35	0.252	24.1	11.04	145.3	54.7	246	56.7	520	98.3	12050
72920-01-27	1.52	0.85	9.8	4.04	57.4	24.1	118.9	33.3	330	77.2	9190
72920-01-28	2.23	0.513	14.2	6.08	91.9	39	200	56	572	124.4	9240
72920-01-29	2.88	0.69	20.3	8.59	120	47.6	235	57.6	578	112	10550
72920-01-30	2.17	0.57	12.2	4.66	63.9	26.2	127	34.4	354	80	10080
72920-01-31	1.84	0.61	10.5	4.58	64.1	25.5	133.3	35.8	387	83.7	9690
72920-01-32	1.48	0.82	10.8	4.15	58.6	23.2	115.5	30.8	332	77.1	8810
72920-01-33	11.26	4.81	47.5	15.7	182	63.3	273	67.5	669	139.9	8680
72920-01-34	1.83	0.335	8.5	3.33	49	18.98	106.1	27.4	289	61.5	10860
72920-01-35	1.64	0.226	12.6	5.48	84.5	37.3	182	49.5	497	101.9	10770
72920-01-36	5.9	2.33	35.7	13.62	181	70.8	343	84.7	875	175.9	8840
72920-01-37	0.78	0.3	3.85	1.44	21	8.35	40.3	10.69	113.4	27.3	10160
72920-01-38	2.83	0.8	16.7	5.94	83.2	31.5	153	40.1	410	88.6	10450
72920-01-39	4.93	1.88	26	9.44	122.6	46.2	225	57.4	564	124.3	8880
72920-01-40	2.99	1.09	21.6	8.98	133	56	286	72.5	711	157.3	8570
72920-01-41	1.04	0.464	5.05	1.93	31.1	12.3	64	17.7	188	45.7	8720
72920-01-42	2.17	0.766	16.6	5.9	83.8	34.8	168.6	43.4	435	93.4	10240
72920-01-43	3.8	1.92	20.4	7.2	102	37	181	45	480	113	9000
72920-01-44	3.21	1.38	19	6.5	79	31.6	158	38.9	389	85.2	7550
72920-01-45	2.7	1.04	22	8.53	123	48	235	55.8	547	115.7	9200
72920-01-46	1.47	0.479	10.7	4.01	57.2	23.7	131	34.2	365	80.7	8760
72920-01-47	1.73	0.69	12.2	4.78	64.1	23.5	112	30.6	312	69.3	9460
72920-01-48	1.42	0.6	6.5	2.26	30.2	11.1	51.5	13.9	144	33.7	9090
72920-01-49	1.55	0.67	8.9	3.04	41.4	16.5	79.4	19.9	221	48	9430
72920-01-50	6.65	0.81	42.3	15.1	198	75.5	343	81.6	731	149.3	10040
72920-01-51	1.56	0.65	10.8	3.88	50.3	19.5	96.6	25.8	257	59.8	9710
72920-01-52	4.2	2.05	25	7.43	95	35.4	172	45.3	461	102	8050

Table 6f. Zircon trace element geochemical data for 266 detrital zircon from the sandstone of Mammoth Rock.

Sample	Si (ppm)	P (ppm)	Ti (ppm)	Y (ppm)	Zr (ppm)	Nb (ppm)	La (ppm)	Ce (ppm)	Pr (ppm)	Nd (ppm)
72920-01-53	1.58E+05	172	5.3	1203	4.20E+05	2.97	-0.07	16.42	0.246	1.93
72920-01-54	1.55E+05	125	0.63	1076	3.94E+05	3.49	-0.2	16.8	0.27	1.13
72920-01-55	1.50E+05	115.8	3.98	515	4.06E+05	1.2	0	5.44	0.3	1
72920-01-56	1.43E+05	171	3.85	732	4.14E+05	2.87	-2.8	13.5	0.55	1.32
72920-01-57	1.52E+05	105.5	3.22	1190	3.96E+05	0.98	-0.44	6.96	0.78	4.27
72920-01-58	1.47E+05	133	2.47	708	4.07E+05	2.53	-0.08	8.9	0.17	0.94
72920-01-59	1.46E+05	84	2.5	459	4.05E+05	0.9	0	5.07	0.146	0.44
72920-01-60	1.56E+05	157	4	1220	4.05E+05	3.95	0	18.1	0.23	1.48
72920-01-61	1.56E+05	102	3.92	649	4.03E+05	1.91	-0.21	8.37	0.183	0.87
72920-01-62	1.48E+05	267	3.11	922	4.15E+05	2.36	-14.8	18	1.35	3.4
72920-01-63	1.44E+05	1570	3	520	3.98E+05	1.16	-53	29.1	12.3	20.2
72920-01-64	1.46E+05	153	5.8	924	4.11E+05	2.9	0	12.06	0.203	1.15
72920-01-65	1.51E+05	55.8	2.16	320	4.03E+05	1.91	-0.17	14.5	0.041	0.31
72920-01-66	1.50E+05	227	3.86	1591	4.09E+05	2.49	-0.52	12.82	0.63	3.42
72920-01-67	1.37E+05	107	3.26	904	3.98E+05	1.73	0	8.39	0.33	2.3
72920-01-68	1.58E+05	146	4.25	902	3.89E+05	3.49	-0.09	16.4	0.22	1.58
72920-01-69	1.57E+05	112.9	4.26	604	4.02E+05	1.62	-0.09	7.35	0.142	0.96
72920-01-70	1.51E+05	103	4.5	479	4.01E+05	1.38	0.04998	6.03	0.101	0.56
72920-01-71	1.48E+05	91.7	3.26	438	4.15E+05	1.29	0.050913	5.82	0.152	0.49
72920-01-72	1.48E+05	100	3.32	444	3.85E+05	1.3	0.051181	6.22	0.131	0.65
72920-01-73	1.54E+05	143	5.96	1320	3.82E+05	3.42	-0.13	13.97	0.24	1.35
72920-01-74	1.58E+05	120	3.69	650	3.98E+05	1.66	-0.22	7.41	0.24	2.09
72920-01-75	1.52E+05	218	3.55	1302	4.06E+05	4.34	-0.19	19.6	0.27	1.82
72920-01-76	1.61E+05	174	1.52	1440	4.04E+05	8.07	-0.045	13.41	0.18	0.78
72920-01-77	1.52E+05	539	1.39	2160	4.19E+05	4.89	-6.1	13.9	1.34	4.09
72920-01-78	1.59E+05	133	4.6	950	3.98E+05	2.54	0	10.28	0.24	1.59
72920-01-79	1.51E+05	142	2.01	646	3.86E+05	1.38	-0.12	10.8	0.1	0.92
72920-01-80	1.42E+05	107	4.8	443	3.88E+05	1.41	-0.05	6.63	0.14	0.61
72920-01-81	1.54E+05	164	3.9	927	4.05E+05	2.22	-0.05	8.52	0.28	1.22
72920-01-82	1.52E+05	152	2.84	988	4.27E+05	2.67	-0.52	16	0.24	1.46
72920-01-83	1.50E+05	155	3.44	700	3.99E+05	1.52	-0.58	6.8	0.2	1.04
72920-01-84	1.45E+05	138	3.45	959	4.17E+05	3.03	-0.29	13.4	0.27	1.24
72920-01-85	1.53E+05	99.4	3.67	511	3.89E+05	1.24	0	6.76	0.14	0.91
72920-01-86	1.53E+05	116.4	3.36	585	4.07E+05	2.05	-0.29	7.86	0.113	0.7
72920-01-87	1.55E+05	145	2.9	939	4.28E+05	2.8	0	16.25	0.14	1.46
72920-01-88	1.57E+05	103.6	2.74	910	4.17E+05	3.16	-0.05	18.92	0.15	0.82
72920-01-89	1.52E+05	82	2.41	475	4.13E+05	1.51	-0.1	8.43	0.14	0.67
72920-01-90	1.52E+05	410	2.83	1021	4.17E+05	3.75	-4.4	21.7	0.92	2.8
72920-01-91	1.54E+05	156	4.93	1470	3.97E+05	1.82	-0.61	17.2	1.19	6.45
72920-01-92	1.52E+05	93	3.73	335	4.11E+05	1	-0.1	4.51	0.047	0.59
72920-01-93	1.57E+05	108	3.1	690	4.11E+05	0.98	-0.31	8.4	0.51	3.5
72920-01-94	1.55E+05	118.3	3.76	736	4.16E+05	2.42	-0.17	9.04	0.21	0.81
72920-01-95	1.54E+05	144.2	3.6	960	4.07E+05	1.77	-0.21	8.2	0.24	1.59
72920-01-96	1.47E+05	132	4.11	801	4.05E+05	2.45	0	9.26	0.158	0.76
72920-01-97	1.44E+05	98	3.15	471	3.92E+05	1.32	-0.11	6.09	0.17	0.73
72920-01-98	1.54E+05	141	1.82	2530	4.05E+05	4.33	0	26.5	0.55	4.19
72920-01-99	1.51E+05	77.1	2.57	366	3.95E+05	0.94	0	5.02	0.079	0.48
72920-01-100	1.52E+05	990	2.08	1129	4.22E+05	1.89	-24	18.9	4.1	9
72920-01-101	1.56E+05	103.7	2.32	448	4.02E+05	1.66	0	8.48	0.096	0.46
72920-01-102	1.47E+05	153	2.6	640	4.10E+05	1.12	0.190784	6.36	0.092	0.56
72920-01-103	1.43E+05	197	4.5	1292	3.98E+05	1.44	-0.21	11.4	0.83	4.87
72920-01-104	1.43E+05	84.5	2.95	476	4.05E+05	1.62	-0.28	7.08	0.118	0.5

Table 6g. Zircon trace element geochemical data for 266 detrital zircon from the sandstone of Mammoth Rock.

Sample	Sm (ppm)	Eu (ppm)	Gd (ppm)	Tb (ppm)	Dy (ppm)	Ho (ppm)	Er (ppm)	Tm (ppm)	Yb (ppm)	Lu (ppm)	Hf (ppm)
72920-01-53	3.08	1.17	20.1	7.32	100.9	40.2	191	47.8	459	104.6	8400
72920-01-54	1.85	0.37	15.1	5.52	79.9	33.1	176.3	47.3	460	98.1	10700
72920-01-55	1.38	0.66	9.4	3.21	44.7	17.7	85.5	22.1	230	55.8	9070
72920-01-56	2.12	0.6	13.4	4.74	64	23.9	115.5	28	278	59.3	10100
72920-01-57	4.95	1.61	25.7	8.78	109.7	38.9	183	46.2	454	95.2	8510
72920-01-58	1.34	0.628	10.9	3.8	51.1	21.5	114.9	29.5	319	72.7	9450
72920-01-59	1.12	0.351	7.09	2.7	36.7	15.9	80.8	20.48	221	46.1	9850
72920-01-60	2.74	1.34	22.1	7.74	103.1	37.8	202	48.8	476	107.2	9440
72920-01-61	1.28	0.62	8.65	3.43	48.8	21.5	114.5	31.6	323	74.3	9840
72920-01-62	2.77	0.78	15.9	5.5	71.1	28	146.4	36.9	373	79.6	10050
72920-01-63	4.2	0.78	10	3.11	36.8	14.9	80	21.4	239	52.7	8830
72920-01-64	1.93	1.02	15.1	6.17	81	30.3	149.9	38.8	394	87.9	8260
72920-01-65	0.7	0.319	4.43	1.68	24	10.14	57.9	14.93	177	38.7	10720
72920-01-66	4.63	1.64	31.9	10.48	141	52.1	260.8	67.1	668	134.9	8160
72920-01-67	3.09	0.91	15.6	5.62	74.1	29.7	142	34.7	385	84.9	8830
72920-01-68	2.47	1.02	15.1	5.5	72.7	30.4	136.1	36.3	365	84.1	9700
72920-01-69	1.43	0.633	9.43	3.07	44.3	19.1	96.7	26.7	252	58.4	8430
72920-01-70	1.05	0.6	6.45	2.46	37.3	14.7	78.5	21.6	228	51.5	8310
72920-01-71	1.27	0.443	7.2	2.76	34.8	14.77	72.2	19.8	211	44.9	9520
72920-01-72	1.24	0.42	6.52	2.46	34.3	14.4	73.8	20.2	200	47.9	8920
72920-01-73	2.19	0.93	19.1	7.52	103.1	44.2	213	55.1	537	110.3	9040
72920-01-74	2.31	0.77	12	4.05	47.6	19.5	101.3	26.3	291	62	8580
72920-01-75	2.87	0.9	22.4	8.23	105.6	43.6	206	50.4	488	104.3	9130
72920-01-76	2.39	0.288	17.1	7.12	103.1	47.1	243	67.8	690	147.3	10570
72920-01-77	4.51	0.75	31.3	12.25	166	71.5	360	91.7	896	188	10400
72920-01-78	1.96	1.19	15.4	5.87	68.1	30	139.3	42.1	424	91.9	7710
72920-01-79	1.48	0.49	9.2	3.57	50	20.3	106	29.8	309	77.8	10210
72920-01-80	1.11	0.51	6.7	2.41	33	14.26	73.8	19.7	215	47.1	7910
72920-01-81	1.98	1.09	14.4	5.03	62.2	26.6	141.6	36.7	404	88.4	9000
72920-01-82	2.56	0.95	16.9	6.12	75.2	30.8	152.1	37.6	387	82.6	9800
72920-01-83	1.57	0.53	10.7	4.1	50.3	19	97	25.3	267	56.7	9820
72920-01-84	2.25	0.92	13.9	5.42	69.5	30.2	151	40.1	398	89.6	9650
72920-01-85	1.18	0.429	7.62	2.74	37.1	16.12	83.6	21.53	228	48.7	8980
72920-01-86	1.54	0.64	8.1	3.38	41.2	18.5	94.1	24.8	255	60.7	9060
72920-01-87	2.32	0.68	15.2	5.39	69	30.4	138.9	37.8	371	80.2	10070
72920-01-88	1.79	0.72	13.1	5.35	67.8	28.6	145.3	36.9	376	81.1	9750
72920-01-89	1.38	0.55	7.04	2.84	33.8	14	74	18.8	220	49.1	9560
72920-01-90	2.2	0.74	11.8	4.85	68.3	30.4	168.1	44.8	484	116	10160
72920-01-91	8.12	3.23	33.7	11.4	128	48	213	51.7	491	103.4	8990
72920-01-92	0.45	0.348	5.02	1.73	24.3	9.29	52.6	13.9	139	34	8850
72920-01-93	3.9	1.41	17.5	5	58	21.6	98	23.5	242	56.4	9350
72920-01-94	1.51	0.76	8.6	3.91	51.9	21.2	112.2	30.1	303	68.1	9270
72920-01-95	2.29	0.82	13.1	5.2	67.4	30.4	160.4	43.9	442	94	8450
72920-01-96	1.58	0.82	10.92	4.65	59.1	25.2	128.1	34.4	354	78.9	8960
72920-01-97	1.32	0.55	6.6	2.71	34.2	14	68.7	18.8	199	46.1	9270
72920-01-98	7.4	1.95	43.4	16.1	195	80.2	407	101.3	972	198.4	10400
72920-01-99	0.89	0.494	5.67	2.28	24.3	11.3	55.9	16.6	174	39.3	10820
72920-01-100	4.6	1.04	16.7	6.78	79.6	35.4	182	47.7	479	105.2	9530
72920-01-101	1.08	0.388	6.32	2.44	33.4	12.88	67.1	17.3	178.9	37.7	10310
72920-01-102	1.01	0.34	7.9	2.97	42	17.9	94	25.2	264	59	9930
72920-01-103	5.7	2.12	26.8	9.47	112.8	42	201	49	462	101.1	8380
72920-01-104	1.01	0.371	6.45	2.58	33.5	14.34	72.7	21.2	209	49.4	10630

Table 6h. Zircon trace element geochemical data for 266 detrital zircon from the sandstone of Mammoth Rock.

Sample	Si (ppm)	P (ppm)	Ti (ppm)	Y (ppm)	Zr (ppm)	Nb (ppm)	La (ppm)	Ce (ppm)	Pr (ppm)	Nd (ppm)
72920-01-105	1.56E+05	135	2.54	554	4.03E+05	0.71	-0.09	3.32	0.118	0.95
72920-01-106	1.48E+05	156	6.1	948	3.92E+05	2.15	-0.85	6.71	0.47	3.47
72920-01-107	1.49E+05	522	19.1	1960	3.79E+05	4.52	-410	72	44	88
72920-01-108	1.49E+05	960	5.16	1007	3.96E+05	2.16	-113	30	11	15.4
72920-01-109	1.39E+05	89	2.27	511	3.91E+05	2	0.078745	9.33	0.167	0.69
72920-01-110	1.47E+05	121	3.46	587	4.04E+05	1.7	-0.44	8.58	0.137	0.98
72920-01-111	1.51E+05	119	4.04	575	4.06E+05	2.08	-0.11	12.15	0.202	1.07
72920-01-112	1.46E+05	230	3.8	1480	3.84E+05	1.96	0	7.53	0.38	1.9
72920-01-113	1.52E+05	68	2.48	309	3.66E+05	0.64	-0.11	3.44	0.119	0.76
72920-01-114	9.83E+04	89.7	2.1	934	2.47E+05	1.95	-0.43	10.6	0.25	1.17
72920-01-115	1.39E+05	55.1	3.9	523	3.53E+05	0.97	0	11.5	0.134	0.97
72920-01-116	1.39E+05	980	3.4	687	3.57E+05	2.5	-170	47	8	7.3
72920-01-117	1.41E+05	123	2.7	458	3.56E+05	0.6	0.15543	3.48	0.049	0.55
72920-01-118	1.42E+05	268	2.16	890	3.71E+05	1.56	0	6.39	0.085	0.9
72920-01-119	1.51E+05	75	4	451	3.53E+05	0.71	-0.51	5.51	0.34	1.59
72920-01-120	1.57E+05	128	1.6	1653	4.15E+05	10.35	-0.05	23	0.117	0.81
72920-01-121	1.48E+05	111.9	5	638	4.20E+05	2.05	-0.07	9.01	0.16	1.11
72920-01-122	1.54E+05	140	6.4	2120	4.27E+05	2.84	-0.59	15.85	0.68	4.31
72920-01-123	1.53E+05	157	3.67	1084	4.09E+05	1.77	-0.6	10.6	0.32	2.32
72920-01-124	1.55E+05	106.1	3.7	568	4.27E+05	1.05	0	7.64	0.15	0.72
72920-01-125	1.52E+05	81.3	2.28	578	4.12E+05	0.92	-0.76	6.27	0.18	1.75
72920-01-126	1.48E+05	358	12.9	3100	4.20E+05	9.14	-1.54	40.5	0.8	5.65
72920-01-127	1.52E+05	211	5.65	1154	4.29E+05	3.11	0.17	10.38	0.28	1.38
72920-01-128	1.45E+05	130	5.3	602	4.04E+05	0.7	-0.98	5.5	0.43	2.1
72920-01-129	1.43E+05	202	32	677	3.89E+05	3.05	-4	8.83	0.36	1.17
72920-01-130	1.51E+05	122	3.39	790	4.17E+05	2.15	-0.43	9.47	0.28	1.17
72920-01-131	1.50E+05	102	4	414	3.95E+05	1.27	-0.63	6.86	0.13	0.89
72920-01-132	1.54E+05	91.6	3.03	243	4.12E+05	0.78	-0.11	5.43	0.079	0.56
72920-01-133	1.48E+05	318	2.26	1880	4.33E+05	6.18	0.19	15.33	0.32	2.51
72920-01-134	1.53E+05	224	4.5	1530	4.10E+05	1.55	-14.2	16.5	1.45	6.5
72920-01-135	1.62E+05	112.8	1.87	860	4.38E+05	1.01	-0.55	8.8	0.38	1.83
72920-01-136	1.49E+05	99	1.34	2150	4.22E+05	1.22	-0.67	8.06	1.09	8.21
72920-01-137	1.49E+05	101.3	3.56	835	4.19E+05	2.08	-0.68	8.58	0.346	1.34
72920-01-138	1.45E+05	141	3.38	775	4.22E+05	1.18	-1.3	8.08	0.49	2.56
72920-01-139	1.53E+05	117.8	5.3	894	4.14E+05	1.17	0	8.44	0.16	1.88
72920-01-140	1.61E+05	122	3.2	626	4.12E+05	1.76	-1	8.08	0.33	1.49
72920-01-141	1.57E+05	265	5.8	1362	4.26E+05	3.92	-3.7	20.6	0.46	2.7
72920-01-142	1.48E+05	120	3.5	662	4.21E+05	2.25	0	10.77	0.17	1.2
72920-01-143	1.56E+05	240	6.2	2940	4.17E+05	4.17	-1.3	23.5	1.26	8.26
72920-01-144	1.57E+05	361	1.58	2400	4.31E+05	9.77	-0.39	20.6	0.261	2.37
72920-01-145	1.52E+05	155	2.02	1210	4.22E+05	1.5	0.35	11.2	0.61	4.1
72920-01-146	1.60E+05	645	8.4	3180	4.10E+05	8.5	-1.9	16.6	0.398	2.89
72920-01-147	1.50E+05	84.2	3.9	679	4.01E+05	1.46	-0.15	7.58	0.167	1.26
72920-01-148	1.57E+05	196	2.57	1212	4.24E+05	2.75	-1.52	15.9	0.29	2.08
72920-01-149	1.51E+05	181	5.7	2020	4.22E+05	2.04	-1.46	12.55	1.14	6.92
72920-01-150	1.54E+05	127	3.74	639	4.24E+05	1.67	-3.9	10.06	0.27	1.46
72920-01-151	1.53E+05	115	4.3	744	4.20E+05	2.12	0	10.09	0.176	1.1
72920-01-152	1.55E+05	84	4.12	865	4.21E+05	0.64	-0.31	5.01	0.61	3.35
72920-01-153	1.53E+05	60.5	5.1	182.3	4.12E+05	0.54	0	3.93	0.074	0.37
72920-01-154	1.55E+05	118.8	7	970	4.26E+05	1.74	-1.3	10.7	0.45	4.2
72920-01-155	1.48E+05	80.1	4.5	360	4.17E+05	1.03	0.20393	5.14	0	0.54
72920-01-156	1.53E+05	600	1.69	976	4.11E+05	4.68	-125	20.5	3.1	6.3

Table 6i. Zircon trace element geochemical data for 266 detrital zircon from the sandstone of Mammoth Rock.

Sample	Sm (ppm)	Eu (ppm)	Gd (ppm)	Tb (ppm)	Dy (ppm)	Ho (ppm)	Er (ppm)	Tm (ppm)	Yb (ppm)	Lu (ppm)	Hf (ppm)
72920-01-105	1.55	0.41	8	3.34	43.2	17.7	85.3	22.9	243	52.6	8640
72920-01-106	4.9	0.6	25.5	9.05	90.2	32	132.6	29.8	236	44.5	8610
72920-01-107	26.2	5.76	62.8	21.3	233	75	311	75.6	681	121.6	10690
72920-01-108	4.8	0.96	16.7	6.16	77.7	32.6	155.7	40.4	363	75.4	9030
72920-01-109	1.52	0.515	6.63	2.67	37.1	16.1	87.4	22.6	244	56	9770
72920-01-110	1.63	0.57	8.1	2.99	41.8	17.3	92.5	24.7	249.1	55.2	8560
72920-01-111	1.96	0.733	9.06	3.61	45.9	18.3	89.6	23.6	235	49.6	9290
72920-01-112	3.68	1.1	25.2	9.36	118.7	49.4	227	60	566	120.6	7240
72920-01-113	1.12	0.523	5.9	2.09	24.4	10.71	53	14.08	155.5	33.8	8660
72920-01-114	2.02	0.77	10.8	4.46	63.6	27.3	150	41.6	398	94.8	5210
72920-01-115	1.67	0.84	8.7	2.86	39.3	16.67	82.8	21.6	251	50.9	7730
72920-01-116	2.25	0.68	11.9	4.04	54.1	21.2	104.8	29.8	280	62	7970
72920-01-117	1.08	0.44	7.2	2.58	35	13.9	75.2	21.1	223	49	6640
72920-01-118	1.51	0.44	13.3	4.61	69	27.9	138	37.7	440	83	8850
72920-01-119	2.04	0.88	8.7	2.85	37.3	13.8	64.9	17.9	186	36.8	7750
72920-01-120	1.86	0.61	16.8	7.5	114	52.2	271	79.8	769	169.3	10440
72920-01-121	1.46	0.77	9.39	3.31	46.3	19.7	106.7	28.1	273	61.8	9370
72920-01-122	5.41	2.13	33.4	12.41	168.3	67.4	321	79.7	755	160	8380
72920-01-123	2.71	0.88	17.9	6.15	81.5	33.3	172	45.9	464	99.1	9220
72920-01-124	1.19	0.46	8.48	2.91	40.7	16.74	89.3	25.59	239	53	9160
72920-01-125	1.9	0.83	11.9	3.27	48.8	17.1	85.8	23.3	232	49.7	9650
72920-01-126	10.18	4.54	77.4	22.7	290	100.3	452	112.3	995	194.7	9500
72920-01-127	2.63	0.96	19.1	6.19	99	36	179.7	47.5	450	94.3	8760
72920-01-128	2.48	1.37	13.8	4.13	54.1	18.99	92.3	23.7	243	53.9	7490
72920-01-129	1.44	0.46	9.4	3.45	53.2	20.7	103.8	29	281	61.8	8860
72920-01-130	2.02	0.84	13.9	4.19	62.9	23.2	124.1	32.7	327	73.1	9530
72920-01-131	1.04	0.53	6.7	2.23	32.1	12.6	66.7	18.2	186	42.4	9350
72920-01-132	0.81	0.278	4.62	1.22	19.4	7.9	41	11.02	112.7	25.3	9040
72920-01-133	3.55	0.66	27.9	9.62	150.3	59.3	311	81.3	772	163	10700
72920-01-134	6.63	1.97	31.8	10.45	137.9	47.2	233.7	53.9	517	105.7	8310
72920-01-135	2.38	0.77	16.9	5.08	71.1	27.3	140.1	37.9	373	76.7	9900
72920-01-136	10.1	3.35	60.4	17.01	221	74.7	327	82	645	126.9	7480
72920-01-137	1.94	0.97	16.4	4.86	67.7	26.4	135	33.2	337	72.6	9340
72920-01-138	3.19	1.331	15	4.64	64	22.9	119.2	29.9	303	64.2	8460
72920-01-139	2.59	0.98	14.7	5.11	71	26.8	133.6	35.9	367	77.9	9340
72920-01-140	1.41	0.71	11.3	3.39	51.8	19.7	104	29.4	315	64.4	9250
72920-01-141	3.62	1.24	24.5	7.5	110.4	43	215	59.8	553	119	9840
72920-01-142	1.43	0.76	10.5	3.83	51.5	20.7	106.8	27.4	286	64.4	9350
72920-01-143	10.01	3.64	64.5	19.5	264	97.4	460	114.4	1046	204	8270
72920-01-144	4.4	0.82	34.7	13.41	205.8	79.6	415	106.2	989	205	10900
72920-01-145	4	1.51	26.6	7.9	109	40.3	201	54.4	520	115	9380
72920-01-146	5.88	0.89	47.3	17.9	267	102.3	535	135.5	1311	252.5	11440
72920-01-147	1.85	0.59	11.7	3.72	49.2	21	112.5	30.9	327	69.2	9450
72920-01-148	3.01	1.12	21.8	7.14	100.1	37.1	195.3	51.7	490	101.8	8780
72920-01-149	8.06	3.2	48.6	15.09	184.1	67.4	328	80.2	773	150.7	7960
72920-01-150	1.6	0.54	10.7	3.27	49.7	20.3	110.8	30.5	289	67	9680
72920-01-151	1.29	0.82	10.3	3.99	58.5	23	123.2	32.6	330	71.8	9120
72920-01-152	3.5	1.22	19.8	6.08	77.4	28.1	135.6	35.4	344	71.3	8710
72920-01-153	0.48	0.25	2.56	0.9	13.7	5.57	30.2	8.91	95.2	22.2	8660
72920-01-154	3.61	1.98	20.2	6.91	87.4	33.7	162	40.4	390	81.2	8430
72920-01-155	0.86	0.443	5.27	1.95	28.3	11.37	62.6	16.3	178	40.6	8990
72920-01-156	2.39	0.53	13.4	5.09	75.7	32.7	159.5	42.2	430	94.2	10700

Table 6j. Zircon trace element geochemical data for 266 detrital zircon from the sandstone of Mammoth Rock.

APPENDIX D

Sample	Age (Ma) $^{207}Pb/^{235}U$	$^{207}Pb/^{235}U$ age 2σ error	Age (Ma) $^{206}Pb/^{238}U$	$^{206}Pb/^{238}U$ age 2σ error	Age (Ma) $^{206}Pb/^{207}Pb$	$^{206}Pb/^{207}Pb$ age 2σ error	Concordance filter	U (ppm)	Th (ppm)
72720-2E-1A-6	219	2	219	1	223	19	1.00	1022	556
72720-2E-1B-8	219	2	219	2	215	15	1.00	681	301
72720-2E-1B-10	222	3	220	3	234	25	0.99	418	216
72720-2E-1A-1	224	2	220	2	252	12	0.99	1060	408
72720-2E-1A-7	224	2	222	2	246	21	0.99	685	234
72720-2E-1A-8	221	2	222	1	220	21	1.00	690	257
72720-2E-1A-4	223	2	223	2	235	18	1.00	621	187
72720-2E-1B-3	224	2	223	2	232	18	0.99	662	347
72720-2E-1A-5	226	2	223	1	259	19	0.99	837	309
72720-2E-1B-5	226	3	224	2	246	14	0.99	1226	379
72720-2E-1B-2	225	3	224	2	228	24	1.00	449	234
72720-2E-1A-2	225	2	224	1	234	13	0.99	666	205
72720-2E-1A-9	226	2	224	2	231	20	0.99	1239	468
72720-2E-1B-11	226	3	226	2	222	25	1.00	536	246
72720-2E-1B-12	227	2	226	2	246	15	1.00	786	537
72720-2E-1B-4	228	3	226	2	264	20	0.99	574	283
72720-2E-1B-1	228	2	226	1	243	25	0.99	444	196
72720-2E-1B-6	231	3	227	1	271	23	0.98	607	339
72720-2E-1A-3	227	3	227	1	212	23	1.00	347	116
72720-2E-1B-9	231	2	229	2	247	16	0.99	986	563
72720-2E-1B-13	231	2	230	1	234	25	0.99	327	131
72720-2E-1B-7	256	3	220	3	609	14	0.86	1139	423
73020-1A-1B-1	214	4	209	1	281	40	0.98	2039	807
73020-1A-1A-3	218	2	213	2	261	29	0.98	599	244
73020-1A-1A-4	216	2	213	2	233	27	0.99	525	168
73020-1A-1A-2	212	3	214	2	200	19	1.01	728	245
73020-1A-1B-3	219	3	218	3	238	19	1.00	514	180
73020-1A-1A-1	233	5	221	2	349	45	0.95	514	265
73020-1A-1B-2	332	67	225	6	990	380	0.66	1236	610
73020-1B-3-1	217	2	214	2	248	10	0.99	1406	644
73020-1B-3-3	215	3	214	2	222	14	1.00	1191	590
73020-1B-3-2	218	3	219	2	221	18	1.00	1048	480
73020-1B-3-4	223	2	223	2	210	17	1.00	883	360
73020-1B-3-7	417	5	395	4	553	31	0.95	186	165
73020-1B-3-5	597	6	591	4	632	29	0.99	233	163
73020-1B-3-12	924	19	878	27	1039	11	0.95	423	383
73020-1B-3-6	978	21	918	30	1120	6	0.94	628	138
73020-1B-3-11	1538	4	1532	7	1549	7	1.00	213	116
73020-1B-3-8	1647	10	1628	16	1675	5	0.99	357	202
73020-1B-3-10	1695	14	1649	10	1741	28	0.97	274	242
73020-1B-3-9	442	11	331	16	1065	49	0.75	345	69
73020-1B-3-13	-	-	-	-	-	-	-	14	12
73020-1C-1B-1	166	3	167	2	146	37	1.01	206	237
73020-1C-1B-2	138	4	135	3	212	42	0.97	322	282
8230-1D-2A-5	217	3	216	3	235	13	0.99	814	330
8230-1D-2A-4	218	2	216	3	228	11	0.99	912	351
8230-1D-2A-2	225	2	224	3	242	13	1.00	1281	420
8230-1D-2A-1	227	3	226	3	246	12	0.99	1496	552

Table 7a. U-Pb age data for 48 zircon grains from 5 clast samples of the breccia of Mammoth Rock (BMR).

Sample	$^{207}Pb/^{235}U$	$^{207}Pb/^{235}U$ 2σ error	$^{206}Pb/^{238}U$	$^{206}Pb/^{238}U$ 2σ error	Error correlation 6/38 - 7/35	$^{206}Pb/^{207}Pb$	$^{206}Pb/^{207}Pb$ 2σ error	Error correlation 38/6 - 7/6	$^{206}Pb/^{204}Pb$	$^{206}Pb/^{204}Pb$ 2σ error
72720-2E-1A-6	0.241	0.005	0.03	0.00	0.5730	0.051	0.001	0.1364	4884	1416
72720-2E-1B-8	0.241	0.005	0.03	0.00	0.7607	0.050	0.001	0.2016	6733	5242
72720-2E-1B-10	0.244	0.006	0.03	0.00	0.7262	0.051	0.001	0.0174	1981	475
72720-2E-1A-1	0.246	0.005	0.03	0.00	0.8439	0.051	0.001	0.0146	3357	642
72720-2E-1A-7	0.247	0.005	0.04	0.00	0.5601	0.051	0.001	0.0962	2494	540
72720-2E-1A-8	0.243	0.005	0.04	0.00	0.4241	0.051	0.001	0.2769	2203	457
72720-2E-1A-4	0.246	0.006	0.04	0.00	0.6506	0.051	0.001	-0.0631	2549	527
72720-2E-1B-3	0.247	0.006	0.04	0.00	0.5739	0.051	0.001	0.1314	5739	2477
72720-2E-1A-5	0.250	0.006	0.04	0.00	0.7584	0.051	0.001	-0.2355	2917	661
72720-2E-1B-5	0.250	0.006	0.04	0.00	0.9256	0.051	0.001	-0.4365	7016	1745
72720-2E-1B-2	0.248	0.006	0.04	0.00	0.7696	0.051	0.001	-0.0985	2120	495
72720-2E-1A-2	0.249	0.005	0.04	0.00	0.5755	0.051	0.001	0.0877	2974	781
72720-2E-1A-9	0.250	0.005	0.04	0.00	0.4107	0.051	0.001	0.5136	5017	1034
72720-2E-1B-11	0.249	0.006	0.04	0.00	0.6799	0.051	0.001	-0.1010	4095	1377
72720-2E-1B-12	0.251	0.006	0.04	0.00	0.7563	0.051	0.001	0.2102	6048	2893
72720-2E-1B-4	0.252	0.006	0.04	0.00	0.7476	0.052	0.001	0.0073	3297	1141
72720-2E-1B-1	0.251	0.006	0.04	0.00	0.3373	0.051	0.001	0.3149	1980	472
72720-2E-1B-6	0.255	0.006	0.04	0.00	0.5472	0.052	0.001	0.0108	4951	1431
72720-2E-1A-3	0.250	0.006	0.04	0.00	0.5300	0.050	0.001	-0.0924	1492	288
72720-2E-1B-9	0.256	0.006	0.04	0.00	0.7773	0.051	0.001	-0.1042	6567	2361
72720-2E-1B-13	0.256	0.006	0.04	0.00	0.2386	0.051	0.001	0.3059	2156	691
72720-2E-1B-7	0.286	0.007	0.03	0.00	0.8916	0.060	0.001	-0.0366	1138	79
73020-1A-1B-1	0.235	0.007	0.03	0.00	0.3194	0.052	0.001	0.0197	4704	1842
73020-1A-1A-3	0.239	0.005	0.03	0.00	0.7048	0.051	0.001	-0.0603	1927	551
73020-1A-1A-4	0.237	0.006	0.03	0.00	0.4261	0.051	0.001	0.2743	1723	360
73020-1A-1A-2	0.232	0.006	0.03	0.00	0.8921	0.050	0.001	-0.6017	1915	266
73020-1A-1B-3	0.241	0.006	0.03	0.00	0.8254	0.051	0.001	-0.0247	2281	490
73020-1A-1A-1	0.259	0.008	0.03	0.00	0.5071	0.054	0.002	-0.1603	926	122
73020-1A-1B-2	0.400	0.100	0.04	0.00	0.9408	0.080	0.017	-0.9107	333	188
73020-1B-3-1	0.239	0.005	0.03	0.00	0.8440	0.051	0.001	-0.0043	5354	989
73020-1B-3-3	0.236	0.006	0.03	0.00	0.8170	0.051	0.001	-0.1189	4373	643
73020-1B-3-2	0.239	0.006	0.03	0.00	0.8172	0.051	0.001	-0.0970	6700	2951
73020-1B-3-4	0.245	0.006	0.04	0.00	0.8394	0.050	0.001	-0.0633	5150	1840
73020-1B-3-7	0.508	0.013	0.06	0.00	0.5197	0.059	0.001	0.0081	1115	189
73020-1B-3-5	0.800	0.019	0.10	0.00	0.5873	0.061	0.001	0.0375	4270	1436
73020-1B-3-12	1.488	0.056	0.15	0.01	0.9898	0.074	0.002	0.5402	5052	679
73020-1B-3-6	1.624	0.064	0.15	0.01	0.9921	0.077	0.002	0.3691	6223	881
73020-1B-3-11	3.550	0.073	0.27	0.01	0.8564	0.096	0.002	0.0967	11819	4281
73020-1B-3-8	4.065	0.095	0.29	0.01	0.9745	0.103	0.002	-0.0388	14844	4056
73020-1B-3-10	4.311	0.113	0.29	0.01	0.1052	0.107	0.003	0.4053	2793	1163
73020-1B-3-9	0.547	0.020	0.05	0.00	0.8885	0.075	0.002	0.8102	576	90
73020-1B-3-13	-	-	-	-	-	-	-	-	255	60
73020-1C-1B-1	0.177	0.005	0.03	0.00	0.6443	0.049	0.001	0.0435	489	85
73020-1C-1B-2	0.146	0.005	0.02	0.00	0.6914	0.050	0.001	-0.1382	547	110
8230-1D-2A-5	0.238	0.006	0.03	0.00	0.9279	0.051	0.001	-0.1990	2729	492
8230-1D-2A-4	0.239	0.006	0.03	0.00	0.9139	0.051	0.001	-0.0198	2879	515
8230-1D-2A-2	0.248	0.006	0.04	0.00	0.8712	0.051	0.001	0.0441	5463	1400
8230-1D-2A-1	0.251	0.006	0.04	0.00	0.9416	0.051	0.001	-0.1186	5256	853

Table 7b. U-Pb analytical data for 48 zircon grains from 5 clast samples of the breccia of Mammoth Rock (BMR).

Sample	Age (Ma) $^{207}Pb/^{235}U$	$^{207}Pb/^{235}U$ age 2σ error	Age (Ma) $^{206}Pb/^{238}U$	$^{206}Pb/^{238}U$ age 2σ error	Age (Ma) $^{206}Pb/^{207}Pb$	$^{206}Pb/^{207}Pb$ age 2σ error	Concordance filter	U (ppm)	Th (ppm)
72820-5	185	7	183	3	221	77	0.99	626	103
72820-17	199	7	199	7	214	27	1.00	836	208
72820-98	207	3	204	3	255	18	0.98	1750	707
72820-71	208	10	204	10	223	18	0.98	840	275
72820-55	207	8	206	6	164	59	1.00	273	92
72820-87	212	7	208	5	242	36	0.98	238	77
72820-10	221	14	209	8	370	120	0.94	740	520
72820-97	227	12	210	7	344	60	0.93	385	146
72820-40	212	4	210	3	252	27	0.99	1345	567
72820-92	212	4	210	3	267	19	0.99	1970	601
72820-68	211	6	211	6	173	21	1.00	1061	291
72820-85	214	4	212	5	210	19	0.99	982	266
72820-2	217	2	212	2	293	23	0.98	1220	470
72820-75	209	4	212	5	153	17	1.01	560	222
72820-25	211	5	212	6	211	24	1.01	809	265
72820-103	213	4	212	3	226	16	1.00	1496	427
72820-110	214	5	213	5	225	18	0.99	1646	662
72820-9	212	5	213	4	223	37	1.00	639	181
72820-65	216	4	213	3	218	36	0.99	543	389
72820-67	214	7	213	5	185	42	0.99	690	173
72820-63	213	4	213	5	183	16	1.00	2071	795
72820-32	213	5	214	6	220	21	1.00	1091	301
72820-77	213	4	214	4	185	27	1.00	1167	515
72820-66	215	4	214	4	199	23	0.99	865	269
72820-4	216	4	215	4	232	13	0.99	1246	615
72820-35	212	4	215	4	210	32	1.01	513	231
72820-14	217	3	216	3	213	20	0.99	892	246
72820-44	219	6	216	6	272	26	0.98	974	314
72820-3	216	4	216	3	223	25	1.00	916	299
72820-33	219	5	216	4	268	27	0.99	1452	560
72820-7	214	4	216	5	206	36	1.01	530	174
72820-93	222	3	217	3	280	11	0.98	1620	484
72820-1	215	6	216	5	214	34	1.01	525	226
72820-74	217	3	217	3	187	27	1.00	1137	278
72820-81	217	20	217	21	206	23	1.00	739	216
72820-49	217	5	217	5	227	19	1.00	1031	487
72820-23	220	5	218	7	280	40	0.99	712	243
72820-104	219	4	217	4	232	26	0.99	780	211
72820-11	215	4	217	4	205	18	1.01	811	284
72820-83	217	5	217	5	203	16	1.00	926	283
72820-13	220	7	218	6	276	31	0.99	795	213
72820-101	256	33	221	8	560	240	0.86	330	137
72820-79	219	3	218	3	206	25	0.99	898	474
72820-28	216	4	218	4	207	17	1.01	1278	394
72820-30	218	8	218	9	250	22	1.00	1010	267
72820-106	219	3	218	4	234	23	1.00	942	283
72820-60	217	5	218	5	179	23	1.00	827	227

Table 8a. U-Pb age data for detrital zircon grains from 2 bulk-rock samples of the sandstone of Mammoth Rock.

Sample	Age (Ma) $^{207}Pb/^{235}U$	$^{207}Pb/^{235}U$ age 2σ error	Age (Ma) $^{206}Pb/^{238}U$	$^{206}Pb/^{238}U$ age 2σ error	Age (Ma) $^{206}Pb/^{207}Pb$	$^{206}Pb/^{207}Pb$ age 2σ error	Concordance filter	U (ppm)	Th (ppm)
72820-56	216	4	218	5	191	26	1.01	1066	302
72820-46	227	9	219	8	303	36	0.97	1032	572
72820-70	218	8	219	8	171	23	1.00	908	238
72820-39	219	6	219	6	237	23	1.00	954	340
72820-38	257	7	222	4	592	60	0.86	1208	382
72820-41	219	3	220	3	219	27	1.00	952	302
72820-99	224	8	220	7	269	29	0.98	1063	394
72820-76	232	11	220	5	322	91	0.95	773	227
72820-94	220	6	220	5	209	23	1.00	1029	377
72820-78	221	10	220	10	206	35	0.99	378	103
72820-73	218	7	220	8	162	36	1.01	938	289
72820-6	230	3	222	3	311	19	0.96	1360	675
72820-45	220	4	221	5	210	17	1.00	756	218
72820-26	230	6	222	5	316	30	0.96	1089	368
72820-43	222	5	222	5	244	25	1.00	836	219
72820-61	227	6	222	7	255	21	0.98	1214	446
72820-105	250	7	224	5	498	26	0.90	1301	507
72820-82	224	6	222	9	202	45	0.99	412	149
72820-42	231	4	223	4	345	24	0.96	1446	1070
72820-84	213	7	222	6	116	39	1.04	273	66
72820-50	222	9	223	9	221	30	1.00	886	276
72820-86	222	11	223	11	211	45	1.00	439	235
72820-12	224	5	223	4	238	29	1.00	544	163
72820-52	222	5	223	5	207	24	1.00	1191	776
72820-22	232	9	224	8	310	29	0.97	2540	1243
72820-19	223	5	224	5	228	30	1.00	492	127
72820-108	224	6	225	5	234	46	1.00	165	45
72820-53	224	4	225	4	212	29	1.00	527	213
72820-59	226	4	225	4	223	33	0.99	322	89
72820-47	223	6	226	4	190	34	1.01	488	139
72820-80	231	8	226	8	239	36	0.98	435	136
72820-36	226	5	226	5	220	31	1.00	904	273
72820-21	228	8	228	9	232	28	1.00	930	297
72820-27	224	9	228	9	199	26	1.02	960	536
72820-37	230	4	231	5	233	24	1.00	1770	870
72820-29	229	7	231	6	210	48	1.01	172	65
72820-89	247	9	232	9	390	48	0.94	687	227
72820-107	231	5	232	4	208	34	1.00	455	162
72820-91	234	10	234	13	258	34	1.00	537	153
72820-51	240	18	235	18	291	38	0.98	520	137
72820-48	235	9	237	9	224	30	1.01	515	207
72820-102	240	5	240	4	244	48	1.00	398	132
72820-16	235	9	240	9	196	27	1.02	548	176
72820-64	244	19	247	22	193	29	1.01	650	166
72820-15	247	21	255	22	195	36	1.03	670	290
72820-58	255	15	256	17	214	28	1.00	720	310
72820-96	257	22	261	25	253	20	1.03	345	149

Table 8b. U-Pb age data for detrital zircon grains from 2 bulk-rock samples of the sandstone of Mammoth Rock.

Sample	Age (Ma) $^{207}Pb/^{235}U$	$^{207}Pb/^{235}U$ age 2σ error	Age (Ma) $^{206}Pb/^{238}U$	$^{206}Pb/^{238}U$ age 2σ error	Age (Ma) $^{206}Pb/^{207}Pb$	$^{206}Pb/^{207}Pb$ age 2σ error	Concordance filter	U (ppm)	Th (ppm)
72820-100	1133	12	1131	20	1143	12	1.00	165	92
72820-34	1218	13	1211	17	1246	24	0.99	137	174
72820-88	1468	12	1446	25	1507	25	0.99	46	32
72820-54	1619	17	1594	34	1644	12	0.98	241	119
72820-109	192	22	189	21	234	60	0.98	257	72
72820-95	238	22	241	25	243	38	1.01	574	135
72820-24	716	39	142	3	3625	83	0.20	49	98
72820-8	990	300	326	68	2810	460	0.31	921	424
72820-31	490	250	252	36	1350	820	0.42	704	206
72820-20	337	31	217	9	1230	110	0.66	785	196
72820-62	304	65	229	17	830	360	0.80	720	200
72820-90	252	32	213	5	570	240	0.84	563	137
72820-69	280	32	238	8	570	220	0.84	209	72
72820-72	21	2	22	1	-30	120	1.03	550	282
72820-18	156	13	153	14	197	39	0.97	207	108
72820-57	-	-	-	-	-	-	-	29	37
72920-01-141	200	4	198	4	213	20	0.99	1170	615
72920-01-10	214	4	209	4	253	34	0.98	554	230
72920-01-98	215	3	213	2	249	22	0.99	1436	693
72920-01-16	213	6	213	3	196	57	1.00	378	133
72920-01-28	217	3	215	2	242	25	0.99	762	276
72920-01-140	223	19	215	17	262	59	0.96	453	143
72920-01-120	215	2	215	2	209	18	1.00	1392	374
72920-01-34	218	2	216	2	236	28	0.99	643	284
72920-01-14	217	3	216	2	221	24	1.00	1359	1376
72920-01-44	212	5	216	2	172	56	1.02	276	144
72920-01-13	220	2	217	2	229	27	0.98	968	279
72920-01-12	218	2	217	2	208	19	1.00	1030	603
72920-01-35	217	3	217	1	218	27	1.00	1007	302
72920-01-38	217	3	218	2	201	22	1.01	1168	706
72920-01-146	219	4	218	4	215	12	1.00	3180	1011
72920-01-29	223	3	219	3	264	17	0.98	1555	810
72920-01-82	224	2	219	2	265	17	0.98	1449	973
72920-01-136	220	5	219	2	210	45	0.99	448	245
72920-01-50	217	2	219	2	222	19	1.01	1165	497
72920-01-17	232	2	220	1	340	23	0.95	1300	754
72920-01-153	220	5	220	3	218	53	1.00	148	53
72920-01-54	220	3	220	3	241	28	1.00	1190	424
72920-01-23	221	9	220	9	236	24	1.00	720	410
72920-01-96	223	5	220	2	232	38	0.99	440	148
72920-01-19	224	2	221	2	252	26	0.99	445	193
72920-01-24	224	4	221	2	247	33	0.99	652	283
72920-01-36	222	2	221	1	225	16	0.99	1277	691
72920-01-144	220	4	221	4	203	13	1.00	2598	1023
72920-01-75	227	2	221	3	291	14	0.98	1291	837
72920-01-103	227	6	221	3	292	54	0.97	419	218

Table 8c. U-Pb age data for detrital zircon grains from 2 bulk-rock samples of the sandstone of Mammoth Rock.

Sample	Age (Ma) $^{207}Pb/^{235}U$	$^{207}Pb/^{235}U$ age 2σ error	Age (Ma) $^{206}Pb/^{238}U$	$^{206}Pb/^{238}U$ age 2σ error	Age (Ma) $^{206}Pb/^{207}Pb$	$^{206}Pb/^{207}Pb$ age 2σ error	Concordance filter	U (ppm)	Th (ppm)
72920-01-4	223	2	221	3	243	20	0.99	1280	746
72920-01-11	224	3	222	2	241	33	0.99	407	140
72920-01-83	228	4	222	3	310	33	0.98	342	136
72920-01-5	224	3	222	2	234	24	0.99	755	341
72920-01-123	222	3	222	2	245	33	1.00	715	290
72920-01-88	226	2	222	1	253	14	0.99	1070	498
72920-01-27	227	5	222	2	235	38	0.98	425	155
72920-01-85	226	4	223	2	249	35	0.99	480	184
72920-01-142	227	5	223	5	231	37	0.99	533	269
72920-01-2	223	3	223	2	234	22	1.00	875	493
72920-01-40	221	1	223	1	221	13	1.01	1111	516
72920-01-7	225	3	223	2	235	24	0.99	1097	702
72920-01-72	225	6	223	4	233	57	0.99	263	87
72920-01-126	224	5	223	4	238	15	1.00	1729	1280
72920-01-21	228	5	224	5	275	35	0.98	438	214
72920-01-122	224	3	223	2	233	19	1.00	1003	568
72920-01-95	228	3	224	2	268	25	0.98	484	166
72920-01-143	225	4	223	5	201	21	0.99	1270	931
72920-01-86	227	5	224	2	276	48	0.98	340	122
72920-01-33	223	2	224	1	218	23	1.00	918	798
72920-01-90	229	3	225	3	280	26	0.98	1073	380
72920-01-156	226	6	225	6	253	21	0.99	1069	374
72920-01-77	230	3	225	3	267	9	0.98	1506	419
72920-01-94	229	5	225	3	275	41	0.98	430	144
72920-01-41	234	4	226	2	311	50	0.96	241	64
72920-01-64	225	4	225	3	239	38	1.00	544	245
72920-01-134	223	4	225	4	184	32	1.01	541	386
72920-01-73	228	3	225	3	246	16	0.99	737	400
72920-01-6	229	5	225	2	240	43	0.98	438	257
72920-01-102	230	5	226	3	294	53	0.98	379	104
72920-01-109	228	4	226	3	265	26	0.99	525	146
72920-01-110	233	4	226	2	308	34	0.97	382	130
72920-01-76	229	3	226	1	254	15	0.99	1005	250
72920-01-111	229	5	226	3	252	27	0.99	654	321
72920-01-56	226	3	226	3	252	21	1.00	558	295
72920-01-25	227	5	226	3	222	44	1.00	435	173
72920-01-104	232	4	226	3	268	44	0.98	338	90
72920-01-154	227	5	226	3	227	48	1.00	340	188
72920-01-68	231	3	227	2	264	25	0.98	770	407
72920-01-8	229	3	227	1	252	36	0.99	446	261
72920-01-133	226	3	227	3	225	17	1.00	1509	527
72920-01-9	230	5	227	2	260	44	0.99	287	107
72920-01-3	227	2	227	2	233	25	1.00	723	254
72920-01-74	231	5	227	3	252	41	0.98	331	125
72920-01-125	227	6	227	5	227	44	1.00	286	125
72920-01-30	227	4	227	4	246	34	1.00	451	171
72920-01-131	223	5	227	6	192	35	1.02	292	107

Table 8d. U-Pb age data for detrital zircon grains from 2 bulk-rock samples of the sandstone of Mammoth Rock.

Sample	Age (Ma) $^{207}Pb/^{235}U$	$^{207}Pb/^{235}U$ age 2σ error	Age (Ma) $^{206}Pb/^{238}U$	$^{206}Pb/^{238}U$ age 2σ error	Age (Ma) $^{206}Pb/^{207}Pb$	$^{206}Pb/^{207}Pb$ age 2σ error	Concordance filter	U (ppm)	Th (ppm)
72920-01-15	230	3	227	3	237	26	0.99	737	389
72920-01-91	231	3	228	2	275	28	0.99	634	456
72920-01-78	230	3	228	1	266	18	0.99	500	209
72920-01-128	230	5	228	3	240	49	0.99	217	107
72920-01-87	231	2	228	2	257	18	0.99	1284	782
72920-01-80	236	4	228	2	323	46	0.97	220	76
72920-01-138	228	3	228	3	191	41	1.00	345	172
72920-01-22	231	5	228	3	230	54	0.99	409	152
72920-01-84	232	4	228	3	256	32	0.98	608	258
72920-01-52	247	20	230	3	400	160	0.93	671	444
72920-01-81	233	4	229	2	268	41	0.98	430	169
72920-01-53	232	3	229	2	284	30	0.99	839	470
72920-01-57	233	4	229	3	269	38	0.98	499	223
72920-01-148	227	5	229	5	210	25	1.01	718	462
72920-01-127	228	2	229	3	225	38	1.01	319	124
72920-01-137	225	7	229	7	180	39	1.01	378	166
72920-01-39	227	4	229	2	227	22	1.01	657	329
72920-01-67	232	3	229	2	245	15	0.99	523	208
72920-01-20	228	3	229	3	210	16	1.00	973	504
72920-01-61	227	4	229	4	231	24	1.01	537	169
72920-01-66	233	3	230	2	281	23	0.98	816	403
72920-01-32	230	3	230	2	235	23	1.00	410	164
72920-01-121	230	3	230	3	232	32	1.00	446	165
72920-01-149	231	3	230	3	238	23	0.99	760	482
72920-01-124	232	3	230	3	253	28	0.99	593	241
72920-01-150	229	4	230	3	227	22	1.00	497	184
72920-01-99	235	5	230	5	273	41	0.98	267	65
72920-01-45	233	3	231	3	264	26	0.99	853	249
72920-01-112	232	4	231	3	248	29	0.99	597	190
72920-01-60	229	3	231	3	240	22	1.01	659	295
72920-01-92	237	5	231	3	304	51	0.97	225	75
72920-01-46	231	3	231	3	254	32	1.00	365	102
72920-01-101	232	4	231	2	257	43	1.00	399	159
72920-01-70	232	6	231	4	237	64	1.00	277	86
72920-01-62	233	3	232	2	254	24	0.99	1055	613
72920-01-139	231	5	232	5	224	36	1.00	375	185
72920-01-48	234	6	232	6	263	46	0.99	184	67
72920-01-79	238	4	233	3	292	26	0.98	700	240
72920-01-51	228	3	232	1	222	39	1.02	447	182
72920-01-117	236	4	233	4	267	34	0.98	263	64
72920-01-71	232	6	232	4	234	54	1.00	214	68
72920-01-31	232	3	232	3	214	27	1.00	650	279
72920-01-100	237	4	233	2	267	26	0.98	830	320
72920-01-116	243	7	233	6	357	34	0.96	376	125
72920-01-58	233	4	233	3	253	38	1.00	389	116
72920-01-43	236	9	233	12	243	31	1.00	590	273
72920-01-97	237	8	234	2	274	74	0.98	266	93

Table 8e. U-Pb age data for detrital zircon grains from 2 bulk-rock samples of the sandstone of Mammoth Rock.

Sample	Age (Ma) $^{207}Pb/^{235}U$	$^{207}Pb/^{235}U$ age 2σ error	Age (Ma) $^{206}Pb/^{238}U$	$^{206}Pb/^{238}U$ age 2σ error	Age (Ma) $^{206}Pb/^{207}Pb$	$^{206}Pb/^{207}Pb$ age 2σ error	Concordance filter	U (ppm)	Th (ppm)
72920-01-42	230	3	233	3	213	28	1.01	637	277
72920-01-152	239	10	234	14	246	30	0.98	349	162
72920-01-69	240	5	234	3	299	40	0.98	348	128
72920-01-118	233	5	234	4	245	28	1.00	660	129
72920-01-105	237	5	234	3	246	47	0.99	350	94
72920-01-135	232	10	234	10	203	35	1.01	456	197
72920-01-93	238	7	234	4	245	31	0.98	311	193
72920-01-130	231	4	234	4	205	31	1.02	414	180
72920-01-155	237	8	235	9	269	52	0.99	229	64
72920-01-1	234	3	235	2	246	19	1.00	736	370
72920-01-18	251	7	236	3	386	55	0.94	862	223
72920-01-147	233	5	236	5	208	28	1.01	387	146
72920-01-89	234	4	236	4	252	44	1.01	352	165
72920-01-132	230	6	235	4	153	48	1.02	230	92
72920-01-119	236	6	236	6	288	42	1.00	196	82
72920-01-151	231	5	236	3	200	29	1.02	427	196
72920-01-145	231	6	236	6	159	18	1.02	644	324
72920-01-55	229	5	236	3	171	48	1.03	227	63
72920-01-59	234	6	239	3	196	45	1.02	216	62
72920-01-37	248	13	241	4	410	200	0.97	146	40
72920-01-113	243	7	241	5	270	60	0.99	165	47
72920-01-49	235	5	242	3	183	55	1.03	190	74
72920-01-47	252	3	251	4	295	30	0.99	467	138
72920-01-114	269	15	252	8	420	71	0.94	459	235
72920-01-115	269	8	263	5	312	70	0.98	185	87
72920-01-65	270	5	271	2	249	34	1.00	257	109
72920-01-108	638	5	634	9	670	29	0.99	300	64
72920-01-26	932	22	876	20	1043	19	0.94	617	218
72920-01-106	1023	8	1019	16	1040	26	1.00	129	50
72920-01-107	1216	42	719	34	2264	18	0.59	609	196
72920-01-129	316	18	248	5	870	130	0.79	379	172
72920-01-63	277	20	235	2	670	180	0.84	350	109

Table 8f. U-Pb age data for detrital zircon grains from 2 bulk-rock samples of the sandstone of Mammoth Rock.

Sample	$^{207}Pb/^{235}U$	$^{207}Pb/^{235}U$ 2σ error	$^{206}Pb/^{238}U$	$^{206}Pb/^{238}U$ 2σ error	Error correlation 6/38 - 7/35	$^{206}Pb/^{207}Pb$	$^{206}Pb/^{207}Pb$ 2σ error	Error correlation 6/38 - 6/7
72820-5	0.200	0.009	0.03	0.00	0.3701	0.051	0.002	0.0956
72820-17	0.217	0.009	0.03	0.00	0.9928	0.050	0.001	-0.5203
72820-98	0.226	0.006	0.03	0.00	0.9203	0.051	0.001	-0.3493
72820-71	0.227	0.013	0.03	0.00	0.9816	0.051	0.001	-0.1480
72820-55	0.226	0.011	0.03	0.00	0.8623	0.049	0.002	0.1396
72820-87	0.232	0.009	0.03	0.00	0.8978	0.051	0.001	-0.2289
72820-10	0.244	0.019	0.03	0.00	0.6821	0.054	0.003	-0.0781
72820-97	0.250	0.015	0.03	0.00	0.8034	0.054	0.002	-0.0108
72820-40	0.232	0.007	0.03	0.00	0.9534	0.051	0.001	-0.3293
72820-92	0.232	0.007	0.03	0.00	0.8451	0.052	0.001	0.1872
72820-68	0.231	0.009	0.03	0.00	0.9685	0.050	0.001	-0.1978
72820-85	0.235	0.007	0.03	0.00	0.9351	0.050	0.001	0.5156
72820-2	0.238	0.005	0.03	0.00	0.9448	0.052	0.001	-0.0766
72820-75	0.228	0.007	0.03	0.00	0.9348	0.049	0.001	0.0681
72820-25	0.231	0.008	0.03	0.00	0.9624	0.050	0.001	0.0182
72820-103	0.233	0.007	0.03	0.00	0.9888	0.051	0.001	-0.2421
72820-110	0.235	0.008	0.03	0.00	0.9647	0.051	0.001	0.0875
72820-9	0.233	0.007	0.03	0.00	0.9372	0.051	0.001	0.1553
72820-65	0.237	0.006	0.03	0.00	0.8400	0.051	0.001	-0.0174
72820-67	0.235	0.010	0.03	0.00	0.9170	0.050	0.001	0.0409
72820-63	0.234	0.007	0.03	0.00	0.9314	0.050	0.001	0.1882
72820-32	0.233	0.008	0.03	0.00	0.9910	0.051	0.001	0.3269
72820-77	0.234	0.007	0.03	0.00	0.9729	0.050	0.001	-0.2277
72820-66	0.236	0.007	0.03	0.00	0.8466	0.050	0.001	0.0924
72820-4	0.237	0.007	0.03	0.00	0.9545	0.051	0.001	-0.2679
72820-35	0.233	0.007	0.03	0.00	0.8982	0.050	0.001	-0.1497
72820-14	0.239	0.006	0.03	0.00	0.9769	0.050	0.001	0.0308
72820-44	0.241	0.008	0.03	0.00	0.8403	0.052	0.001	-0.0005
72820-3	0.237	0.007	0.03	0.00	0.9756	0.051	0.001	-0.1930
72820-33	0.241	0.008	0.03	0.00	0.8973	0.052	0.001	-0.5119
72820-7	0.234	0.007	0.03	0.00	0.9296	0.050	0.001	-0.0419
72820-93	0.244	0.006	0.03	0.00	0.9885	0.052	0.001	-0.0828
72820-1	0.235	0.008	0.03	0.00	0.7863	0.050	0.001	0.3046
72820-74	0.238	0.006	0.03	0.00	0.7874	0.050	0.001	-0.0320
72820-81	0.239	0.025	0.03	0.00	0.9954	0.050	0.001	-0.0988
72820-49	0.238	0.008	0.03	0.00	0.9700	0.051	0.001	-0.4500
72820-23	0.242	0.008	0.03	0.00	0.9153	0.052	0.001	0.3833
72820-104	0.241	0.007	0.03	0.00	0.9096	0.051	0.001	0.1783
72820-11	0.236	0.007	0.03	0.00	0.9877	0.050	0.001	-0.0663
72820-83	0.238	0.007	0.03	0.00	0.9727	0.050	0.001	0.0206
72820-13	0.242	0.010	0.03	0.00	0.9421	0.052	0.001	0.2181
72820-101	0.289	0.044	0.03	0.00	0.5130	0.061	0.008	-0.3488
72820-79	0.240	0.006	0.03	0.00	0.6994	0.050	0.001	0.1726
72820-28	0.237	0.007	0.03	0.00	0.9845	0.050	0.001	-0.1670
72820-30	0.240	0.011	0.03	0.00	0.9542	0.051	0.001	-0.2009
72820-106	0.241	0.006	0.03	0.00	0.9184	0.051	0.001	0.2884
72820-60	0.238	0.007	0.03	0.00	0.9748	0.050	0.001	-0.0670

Table 9a. U-Pb analytical data for detrital zircon grains from 2 bulk-rock samples of the sandstone of Mammoth Rock.

Sample	$^{207}Pb/^{235}U$	$^{207}Pb/^{235}U$ 2σ error	$^{206}Pb/^{238}U$	$^{206}Pb/^{238}U$ 2σ error	Error correlation 6/38 - 7/35	$^{206}Pb/^{207}Pb$	$^{206}Pb/^{207}Pb$ 2σ error	Error correlation 6/38 - 6/7
72820-56	0.237	0.007	0.03	0.00	0.8922	0.050	0.001	0.0584
72820-46	0.250	0.013	0.03	0.00	0.9325	0.052	0.001	-0.3618
72820-70	0.240	0.011	0.03	0.00	0.9690	0.050	0.001	-0.1077
72820-39	0.241	0.009	0.03	0.00	0.9745	0.051	0.001	-0.1507
72820-38	0.288	0.011	0.04	0.00	0.3909	0.060	0.002	0.1849
72820-41	0.241	0.006	0.03	0.00	0.6463	0.051	0.001	0.3303
72820-99	0.247	0.011	0.03	0.00	0.9313	0.052	0.001	-0.2298
72820-76	0.257	0.015	0.03	0.00	0.6759	0.052	0.002	-0.2588
72820-94	0.242	0.009	0.03	0.00	0.9823	0.050	0.001	-0.0483
72820-78	0.244	0.013	0.03	0.00	0.9603	0.050	0.001	-0.3077
72820-73	0.240	0.009	0.03	0.00	0.8627	0.049	0.001	0.1154
72820-6	0.254	0.006	0.03	0.00	0.9341	0.053	0.001	0.5970
72820-45	0.242	0.007	0.03	0.00	0.9554	0.050	0.001	-0.2317
72820-26	0.255	0.009	0.04	0.00	0.9148	0.053	0.001	-0.1708
72820-43	0.244	0.008	0.03	0.00	0.9016	0.051	0.001	-0.2308
72820-61	0.251	0.009	0.04	0.00	0.9227	0.051	0.001	0.1495
72820-105	0.279	0.011	0.04	0.00	0.8801	0.057	0.001	-0.2666
72820-82	0.247	0.009	0.04	0.00	0.8932	0.050	0.001	0.3453
72820-42	0.255	0.007	0.04	0.00	0.8266	0.053	0.001	-0.2012
72820-84	0.234	0.010	0.03	0.00	0.8330	0.048	0.001	-0.0378
72820-50	0.245	0.012	0.04	0.00	0.9703	0.051	0.001	0.1413
72820-86	0.244	0.014	0.04	0.00	0.9227	0.050	0.001	0.0792
72820-12	0.246	0.007	0.04	0.00	0.8920	0.051	0.001	-0.1039
72820-52	0.245	0.008	0.04	0.00	0.9265	0.050	0.001	-0.0378
72820-22	0.257	0.012	0.04	0.00	0.9675	0.053	0.001	-0.5869
72820-19	0.246	0.008	0.04	0.00	0.7914	0.051	0.001	0.2724
72820-108	0.247	0.008	0.04	0.00	0.7688	0.051	0.001	-0.0799
72820-53	0.247	0.007	0.04	0.00	0.8458	0.050	0.001	0.0359
72820-59	0.249	0.007	0.04	0.00	0.6540	0.050	0.001	0.5650
72820-47	0.246	0.009	0.04	0.00	0.9284	0.050	0.001	-0.3923
72820-80	0.256	0.011	0.04	0.00	0.7762	0.051	0.001	0.2056
72820-36	0.249	0.008	0.04	0.00	0.9772	0.051	0.001	-0.2158
72820-21	0.251	0.011	0.04	0.00	0.9831	0.051	0.001	-0.3522
72820-27	0.247	0.012	0.04	0.00	0.9898	0.050	0.001	-0.0305
72820-37	0.255	0.007	0.04	0.00	0.9543	0.051	0.001	0.1764
72820-29	0.253	0.010	0.04	0.00	0.7117	0.050	0.001	0.0453
72820-89	0.276	0.012	0.04	0.00	0.9301	0.055	0.002	0.4346
72820-107	0.256	0.008	0.04	0.00	0.8293	0.050	0.001	-0.0952
72820-91	0.260	0.014	0.04	0.00	0.9715	0.051	0.001	0.6167
72820-51	0.268	0.023	0.04	0.00	0.9883	0.052	0.001	-0.4318
72820-48	0.261	0.012	0.04	0.00	0.9482	0.051	0.001	0.3320
72820-102	0.267	0.008	0.04	0.00	0.7055	0.051	0.002	0.1513
72820-16	0.261	0.012	0.04	0.00	0.9216	0.050	0.001	-0.0213
72820-64	0.272	0.025	0.04	0.00	0.9865	0.050	0.001	0.0346
72820-15	0.277	0.027	0.04	0.00	0.6454	0.050	0.001	-0.1124
72820-58	0.286	0.021	0.04	0.00	0.9599	0.050	0.001	-0.0021
72820-96	0.282	0.027	0.04	0.00	0.9936	0.051	0.001	-0.0353

Table 9b. U-Pb analytical data for detrital zircon grains from 2 bulk-rock samples of the sandstone of Mammoth Rock.

Sample	$^{207}Pb/^{235}U$	$^{207}Pb/^{235}U$ 2σ error	$^{206}Pb/^{238}U$	$^{206}Pb/^{238}U$ 2σ error	Error correlation 6/38 - 7/35	$^{206}Pb/^{207}Pb$	$^{206}Pb/^{207}Pb$ 2σ error	Error correlation 6/38 - 6/7
72820-100	2.054	0.055	0.19	0.01	0.9492	0.078	0.002	0.0329
72820-34	2.321	0.063	0.21	0.01	0.7529	0.082	0.002	0.1813
72820-88	3.245	0.082	0.25	0.01	0.8702	0.094	0.002	0.1977
72820-54	3.927	0.114	0.28	0.01	0.9812	0.101	0.002	0.2439
72820-109	0.209	0.026	0.03	0.00	0.9823	0.051	0.002	-0.4567
72820-95	0.266	0.029	0.04	0.00	0.9829	0.051	0.001	0.2533
72820-24	1.007	0.075	0.02	0.00	0.8439	0.334	0.019	-0.6563
72820-8	1.820	0.871	0.05	0.01	0.9953	0.230	0.061	-0.9651
72820-31	0.810	0.540	0.04	0.01	0.9867	0.119	0.062	-0.9475
72820-20	0.383	0.047	0.03	0.00	0.9157	0.082	0.005	-0.3322
72820-62	0.326	0.071	0.04	0.00	0.7859	0.068	0.012	-0.5986
72820-90	0.284	0.044	0.03	0.00	0.3031	0.061	0.009	-0.1986
72820-69	0.320	0.043	0.04	0.00	0.7139	0.061	0.007	-0.5817
72820-72	0.021	0.002	0.00	0.00	0.5837	0.045	0.003	-0.1527
72820-18	0.167	0.015	0.02	0.00	0.9690	0.050	0.001	0.3169
72820-57	-	-	-	-	-	-	-	-
72920-01-141	0.217	0.006	0.03	0.00	0.9767	0.050	0.001	-0.4107
72920-01-10	0.234	0.007	0.03	0.00	0.7628	0.051	0.001	0.1339
72920-01-98	0.235	0.006	0.03	0.00	0.8643	0.051	0.001	-0.3405
72920-01-16	0.233	0.008	0.03	0.00	0.6269	0.050	0.002	-0.2771
72920-01-28	0.239	0.006	0.03	0.00	0.7245	0.051	0.001	-0.1562
72920-01-140	0.246	0.024	0.03	0.00	0.8970	0.052	0.002	-0.1622
72920-01-120	0.236	0.005	0.03	0.00	0.6529	0.050	0.001	0.0310
72920-01-34	0.240	0.005	0.03	0.00	0.7313	0.051	0.001	0.4962
72920-01-14	0.238	0.006	0.03	0.00	0.9252	0.051	0.001	-0.1781
72920-01-44	0.232	0.008	0.03	0.00	0.6938	0.050	0.002	-0.2699
72920-01-13	0.243	0.006	0.03	0.00	0.6095	0.051	0.001	0.3692
72920-01-12	0.239	0.006	0.03	0.00	0.7966	0.050	0.001	-0.1973
72920-01-35	0.239	0.006	0.03	0.00	0.5395	0.051	0.001	-0.1582
72920-01-38	0.238	0.006	0.03	0.00	0.9279	0.050	0.001	-0.0765
72920-01-146	0.241	0.007	0.03	0.00	0.9699	0.050	0.001	-0.1848
72920-01-29	0.246	0.006	0.03	0.00	0.9248	0.052	0.001	0.0262
72920-01-82	0.247	0.005	0.03	0.00	0.8749	0.052	0.001	-0.2789
72920-01-136	0.243	0.008	0.03	0.00	0.6347	0.050	0.001	0.0555
72920-01-50	0.239	0.005	0.03	0.00	0.7405	0.051	0.001	-0.1533
72920-01-17	0.257	0.006	0.03	0.00	0.3083	0.053	0.001	0.3550
72920-01-153	0.242	0.008	0.03	0.00	0.7354	0.051	0.001	-0.0332
72920-01-54	0.242	0.006	0.03	0.00	0.6866	0.051	0.001	0.1084
72920-01-23	0.243	0.012	0.03	0.00	0.9739	0.051	0.001	-0.1676
72920-01-96	0.246	0.007	0.03	0.00	0.7499	0.051	0.001	-0.0574
72920-01-19	0.246	0.006	0.03	0.00	0.5797	0.051	0.001	0.2909
72920-01-24	0.247	0.007	0.03	0.00	0.5825	0.051	0.001	-0.0578
72920-01-36	0.244	0.005	0.03	0.00	0.8461	0.051	0.001	0.4800
72920-01-144	0.242	0.007	0.03	0.00	0.9763	0.050	0.001	-0.0188
72920-01-75	0.250	0.006	0.03	0.00	0.8798	0.052	0.001	0.1095
72920-01-103	0.251	0.009	0.03	0.00	0.6829	0.052	0.002	-0.1819

Table 9c. U-Pb analytical data for detrital zircon grains from 2 bulk-rock samples of the sandstone of Mammoth Rock.

Sample	$^{207}Pb/^{235}U$	$^{207}Pb/^{235}U$ 2σ error	$^{206}Pb/^{238}U$	$^{206}Pb/^{238}U$ 2σ error	Error correlation 6/38 - 7/35	$^{206}Pb/^{207}Pb$	$^{206}Pb/^{207}Pb$ 2σ error	Error correlation 6/38 - 6/7
72920-01-4	0.246	0.005	0.03	0.00	0.9033	0.051	0.001	0.2537
72920-01-11	0.246	0.006	0.03	0.00	0.8809	0.051	0.001	-0.1324
72920-01-83	0.251	0.007	0.04	0.00	0.6441	0.053	0.001	0.2914
72920-01-5	0.247	0.006	0.04	0.00	0.5073	0.051	0.001	0.3218
72920-01-123	0.245	0.006	0.04	0.00	0.7607	0.051	0.001	-0.2247
72920-01-88	0.249	0.006	0.04	0.00	0.9794	0.051	0.001	-0.5490
72920-01-27	0.250	0.008	0.04	0.00	0.5654	0.051	0.001	-0.0503
72920-01-85	0.249	0.007	0.04	0.00	0.4759	0.051	0.001	0.1137
72920-01-142	0.248	0.009	0.04	0.00	0.8985	0.051	0.001	-0.3358
72920-01-2	0.246	0.006	0.04	0.00	0.9348	0.051	0.001	-0.3590
72920-01-40	0.244	0.005	0.04	0.00	0.8631	0.051	0.001	-0.0087
72920-01-7	0.248	0.006	0.04	0.00	0.6389	0.051	0.001	-0.0406
72920-01-72	0.248	0.009	0.04	0.00	0.6212	0.051	0.002	-0.0031
72920-01-126	0.247	0.008	0.04	0.00	0.9730	0.051	0.001	-0.3984
72920-01-21	0.252	0.008	0.04	0.00	0.7483	0.052	0.001	0.0748
72920-01-122	0.246	0.006	0.04	0.00	0.8374	0.051	0.001	0.0106
72920-01-95	0.252	0.007	0.04	0.00	0.6194	0.052	0.001	0.4080
72920-01-143	0.248	0.007	0.04	0.00	0.9329	0.050	0.001	0.0870
72920-01-86	0.251	0.007	0.04	0.00	0.5860	0.052	0.002	-0.1414
72920-01-33	0.245	0.006	0.04	0.00	0.3280	0.051	0.001	0.4009
72920-01-90	0.253	0.006	0.04	0.00	0.7087	0.052	0.001	0.0839
72920-01-156	0.250	0.009	0.04	0.00	0.9632	0.051	0.001	-0.2875
72920-01-77	0.254	0.007	0.04	0.00	0.9929	0.052	0.001	0.0429
72920-01-94	0.253	0.008	0.04	0.00	0.6149	0.052	0.001	-0.0481
72920-01-41	0.259	0.007	0.04	0.00	0.4326	0.053	0.002	-0.0360
72920-01-64	0.249	0.007	0.04	0.00	0.6400	0.051	0.001	0.1491
72920-01-134	0.245	0.007	0.04	0.00	0.7524	0.050	0.001	0.3733
72920-01-73	0.252	0.006	0.04	0.00	0.8630	0.051	0.001	-0.0476
72920-01-6	0.253	0.008	0.04	0.00	0.4778	0.051	0.001	-0.0455
72920-01-102	0.255	0.008	0.04	0.00	0.6798	0.052	0.002	0.3584
72920-01-109	0.252	0.007	0.04	0.00	0.7931	0.052	0.001	-0.2204
72920-01-110	0.258	0.007	0.04	0.00	0.6564	0.053	0.001	0.0433
72920-01-76	0.253	0.006	0.04	0.00	0.9546	0.051	0.001	-0.4680
72920-01-111	0.253	0.008	0.04	0.00	0.8938	0.051	0.001	-0.1626
72920-01-56	0.249	0.006	0.04	0.00	0.8260	0.051	0.001	0.1447
72920-01-25	0.250	0.008	0.04	0.00	0.5978	0.051	0.001	0.0267
72920-01-104	0.257	0.007	0.04	0.00	0.6758	0.052	0.001	0.2176
72920-01-154	0.250	0.008	0.04	0.00	0.7330	0.051	0.001	-0.0122
72920-01-68	0.255	0.006	0.04	0.00	0.6811	0.052	0.001	0.2262
72920-01-8	0.253	0.007	0.04	0.00	0.4580	0.051	0.001	0.1278
72920-01-133	0.249	0.006	0.04	0.00	0.9495	0.051	0.001	0.2618
72920-01-9	0.254	0.008	0.04	0.00	0.5416	0.051	0.002	-0.2266
72920-01-3	0.251	0.006	0.04	0.00	0.3700	0.051	0.001	0.2443
72920-01-74	0.255	0.008	0.04	0.00	0.6205	0.051	0.001	0.0381
72920-01-125	0.250	0.009	0.04	0.00	0.7509	0.051	0.001	-0.1733
72920-01-30	0.250	0.007	0.04	0.00	0.7307	0.051	0.001	-0.1272
72920-01-131	0.246	0.008	0.04	0.00	0.6440	0.050	0.001	0.3083

Table 9d. U-Pb analytical data for detrital zircon grains from 2 bulk-rock samples of the sandstone of Mammoth Rock.

Sample	$^{207}Pb/^{235}U$	$^{207}Pb/^{235}U$ 2σ error	$^{206}Pb/^{238}U$	$^{206}Pb/^{238}U$ 2σ error	Error correlation 6/38 - 7/35	$^{206}Pb/^{207}Pb$	$^{206}Pb/^{207}Pb$ 2σ error	Error correlation 6/38 - 6/7
72920-01-15	0.254	0.006	0.04	0.00	0.9080	0.051	0.001	0.1819
72920-01-91	0.255	0.007	0.04	0.00	0.7624	0.052	0.001	-0.1946
72920-01-78	0.255	0.006	0.04	0.00	0.6807	0.052	0.001	0.0715
72920-01-128	0.255	0.008	0.04	0.00	0.6032	0.051	0.002	0.2170
72920-01-87	0.255	0.006	0.04	0.00	0.7032	0.051	0.001	0.3228
72920-01-80	0.262	0.007	0.04	0.00	0.5982	0.053	0.001	-0.0085
72920-01-138	0.251	0.007	0.04	0.00	0.9299	0.050	0.001	0.1168
72920-01-22	0.254	0.008	0.04	0.00	0.4683	0.051	0.002	0.2256
72920-01-84	0.257	0.007	0.04	0.00	0.7131	0.051	0.001	0.1940
72920-01-52	0.276	0.027	0.04	0.00	0.7066	0.055	0.005	-0.6384
72920-01-81	0.258	0.007	0.04	0.00	0.2527	0.052	0.001	0.2791
72920-01-53	0.256	0.006	0.04	0.00	0.6416	0.052	0.001	-0.1735
72920-01-57	0.258	0.007	0.04	0.00	0.8313	0.052	0.001	0.0684
72920-01-148	0.250	0.008	0.04	0.00	0.8675	0.050	0.001	0.3412
72920-01-127	0.251	0.006	0.04	0.00	0.4349	0.051	0.001	0.5866
72920-01-137	0.248	0.010	0.04	0.00	0.8905	0.050	0.001	0.0108
72920-01-39	0.251	0.007	0.04	0.00	0.7894	0.051	0.001	-0.4160
72920-01-67	0.256	0.006	0.04	0.00	0.7252	0.051	0.001	-0.1890
72920-01-20	0.252	0.006	0.04	0.00	0.9019	0.050	0.001	0.0783
72920-01-61	0.251	0.007	0.04	0.00	0.8424	0.051	0.001	-0.3369
72920-01-66	0.258	0.006	0.04	0.00	0.7734	0.052	0.001	-0.0785
72920-01-32	0.254	0.007	0.04	0.00	0.4575	0.051	0.001	0.2114
72920-01-121	0.254	0.007	0.04	0.00	0.7410	0.051	0.001	0.0664
72920-01-149	0.255	0.006	0.04	0.00	0.9877	0.051	0.001	-0.2928
72920-01-124	0.257	0.007	0.04	0.00	0.7701	0.051	0.001	-0.2669
72920-01-150	0.253	0.007	0.04	0.00	0.8800	0.051	0.001	0.2091
72920-01-99	0.260	0.008	0.04	0.00	0.7955	0.052	0.001	-0.2559
72920-01-45	0.258	0.006	0.04	0.00	0.8815	0.052	0.001	-0.1150
72920-01-112	0.257	0.007	0.04	0.00	0.6860	0.051	0.001	0.1138
72920-01-60	0.253	0.006	0.04	0.00	0.6747	0.051	0.001	0.3281
72920-01-92	0.264	0.008	0.04	0.00	0.6199	0.053	0.002	0.1791
72920-01-46	0.255	0.006	0.04	0.00	0.3713	0.051	0.001	0.5484
72920-01-101	0.257	0.007	0.04	0.00	0.6057	0.051	0.001	-0.1464
72920-01-70	0.257	0.009	0.04	0.00	0.3266	0.051	0.002	0.2395
72920-01-62	0.258	0.006	0.04	0.00	0.6754	0.051	0.001	-0.0082
72920-01-139	0.256	0.008	0.04	0.00	0.6996	0.051	0.001	0.2496
72920-01-48	0.259	0.009	0.04	0.00	0.7380	0.052	0.001	0.1403
72920-01-79	0.264	0.007	0.04	0.00	0.8555	0.052	0.001	0.0160
72920-01-51	0.252	0.006	0.04	0.00	0.4574	0.051	0.001	-0.1495
72920-01-117	0.262	0.007	0.04	0.00	0.7066	0.052	0.001	0.4400
72920-01-71	0.257	0.009	0.04	0.00	0.6950	0.051	0.002	-0.0050
72920-01-31	0.257	0.006	0.04	0.00	0.7954	0.050	0.001	-0.1541
72920-01-100	0.263	0.008	0.04	0.00	0.9706	0.052	0.001	-0.3567
72920-01-116	0.270	0.011	0.04	0.00	0.8118	0.054	0.001	0.1245
72920-01-58	0.258	0.007	0.04	0.00	0.8260	0.051	0.001	-0.0231
72920-01-43	0.258	0.014	0.04	0.00	0.9305	0.051	0.001	0.1015
72920-01-97	0.263	0.011	0.04	0.00	0.4198	0.052	0.002	0.0897

Table 9e. U-Pb analytical data for detrital zircon grains from 2 bulk-rock samples of the sandstone of Mammoth Rock.

Sample	$^{207}Pb/^{235}U$	$^{207}Pb/^{235}U$ 2σ error	$^{206}Pb/^{238}U$	$^{206}Pb/^{238}U$ 2σ error	Error correlation 6/38 - 7/35	$^{206}Pb/^{207}Pb$	$^{206}Pb/^{207}Pb$ 2σ error	Error correlation 6/38 - 6/7
72920-01-42	0.255	0.006	0.04	0.00	0.4688	0.050	0.001	0.3561
72920-01-152	0.266	0.013	0.04	0.00	0.9831	0.051	0.001	-0.0375
72920-01-69	0.266	0.008	0.04	0.00	0.4091	0.052	0.001	0.2904
72920-01-118	0.258	0.008	0.04	0.00	0.8236	0.051	0.001	-0.1628
72920-01-105	0.263	0.008	0.04	0.00	0.3125	0.051	0.001	0.3398
72920-01-135	0.257	0.013	0.04	0.00	0.9504	0.050	0.001	-0.2571
72920-01-93	0.264	0.010	0.04	0.00	0.7403	0.051	0.001	-0.0971
72920-01-130	0.255	0.007	0.04	0.00	0.8811	0.050	0.001	0.0553
72920-01-155	0.264	0.011	0.04	0.00	0.8322	0.052	0.002	0.1551
72920-01-1	0.259	0.006	0.04	0.00	0.9343	0.051	0.001	-0.1966
72920-01-18	0.280	0.011	0.04	0.00	0.6670	0.054	0.002	-0.2186
72920-01-147	0.258	0.008	0.04	0.00	0.8437	0.050	0.001	0.0127
72920-01-89	0.260	0.008	0.04	0.00	0.6173	0.051	0.001	0.2479
72920-01-132	0.254	0.008	0.04	0.00	0.4434	0.049	0.001	0.3430
72920-01-119	0.262	0.009	0.04	0.00	0.6328	0.052	0.001	0.2164
72920-01-151	0.255	0.008	0.04	0.00	0.8576	0.050	0.001	0.1033
72920-01-145	0.255	0.009	0.04	0.00	0.9687	0.049	0.001	-0.2401
72920-01-55	0.253	0.008	0.04	0.00	0.5251	0.050	0.001	-0.1273
72920-01-59	0.259	0.009	0.04	0.00	0.7412	0.050	0.001	-0.3298
72920-01-37	0.277	0.017	0.04	0.00	0.7882	0.056	0.006	-0.7069
72920-01-113	0.271	0.010	0.04	0.00	0.5535	0.052	0.002	0.1264
72920-01-49	0.261	0.008	0.04	0.00	0.4350	0.050	0.002	0.0718
72920-01-47	0.282	0.007	0.04	0.00	0.7854	0.052	0.001	0.2317
72920-01-114	0.303	0.020	0.04	0.00	0.9721	0.055	0.002	-0.8966
72920-01-115	0.304	0.013	0.04	0.00	0.5665	0.053	0.002	0.0696
72920-01-65	0.305	0.008	0.04	0.00	0.4234	0.051	0.001	0.1125
72920-01-108	0.874	0.020	0.10	0.00	0.6634	0.062	0.002	0.3220
72920-01-26	1.505	0.062	0.15	0.00	0.9830	0.074	0.002	-0.5109
72920-01-106	1.740	0.042	0.17	0.00	0.5665	0.074	0.002	0.5889
72920-01-107	2.320	0.138	0.12	0.01	0.9924	0.143	0.003	-0.6646
72920-01-129	0.365	0.025	0.04	0.00	0.4898	0.069	0.005	-0.2497
72920-01-63	0.315	0.028	0.04	0.00	0.7435	0.063	0.005	-0.6621

Table 9f. U-Pb analytical data for detrital zircon grains from 2 bulk-rock samples of the sandstone of Mammoth Rock.